AD-A008 992

MODELS FOR DUCTILE AND BRITTLE FRACTURE FOR TWO-DIMENSIONAL WAVE PROPAGATION CALCULATIONS

L. Seaman, et al

Stanford Research Institute

Prepared for:

Army Materials and Mechanics Research Center

February 1975

UNCLASSIFIED

SECURITY CLASSIFICATION OF THIS PAGE (When Data Entered)

REPORT DOCUMENTATION PAGE

READ INSTRUCTIONS BEFORE COMPLETING FORM

1. REPORT NUMBER: AMMRC CTR 75-2	2. GOVT ACCESSION NO.
3. RECIPIENT'S CATALOG NUMBER: AD-A008 992	
4. TITLE (and Subtitle): MODELS FOR DUCTILE AND BRITTLE FRACTURE FOR TWO-DIMENSIONAL WAVE PROPAGATION CALCULATIONS	5. TYPE OF REPORT & PERIOD COVERED: FINAL REPORT June 20, 1972 to Feb.19,1974
	6. PERFORMING ORG. REPORT NUMBER: SRI Project PYU-2024
7. AUTHOR(s): L. Seaman, D. A. Shockey	8. CONTRACT OR GRANT NUMBER(s): DAAG46-72-C-0182
9. PERFORMING ORGANIZATION NAME AND ADDRESS: Stanford Research Institute, 333 Ravenswood Avenue, Menlo Park, California 94025	10. PROGRAM ELEMENT, PROJECT, TASK AREA & WORK UNIT NUMBERS: D/A Project: IT062105AH84; AMCMS Code: 61205.11.H8400; Agency Accession: DA)E4702
11. CONTROLLING OFFICE NAME AND ADDRESS: Army Materials and Mechanics Research Center, Watertown, Massachusetts 02172	12. REPORT DATE: February, 1975
	13. NUMBER OF PAGES
14. MONITORING AGENCY NAME & ADDRESS (if different from Controlling Office)	15. SECURITY CLASS. (of this report): Unclassified
	15a. DECLASSIFICATION/DOWNGRADING SCHEDULE

16. DISTRIBUTION STATEMENT (of this Report)

Approved for public release; distribution unlimited.

17. DISTRIBUTION STATEMENT (of the abstract entered in Block 20, if different from Report)

18. SUPPLEMENTARY NOTES

19. KEY WORDS (Continue on reverse side if necessary and identify by block number)

Spalling
Armor
Fracture Strength
Shock waves
Adiabatic shear
Hugoniot data

20. ABSTRACT (Continue on reverse side if necessary and identify by block number)

Two-dimensional computational subroutines were constructed to simulate ductile and brittle fracture in Lagrangian wave propagation computer programs applied to armor penetration problems. Included in these subroutines are models of void or crack nucleation and growth, and the stress and strength reduction associated with developing damage. These models extended the earlier one-dimensional models to multidimensional problems, higher shear strain cases, and higher damage levels (including full separation in the

DD FORM 1 JAN 73 1473 EDITION OF 1 NOV 65 IS OBSOLETE

UNCLASSIFIED

SECURITY CLASSIFICATION OF THIS PAGE (When Data Entered) ductile model).

Rolled homogeneous steel XAR30 was characterized statically and dynamically. Tapered-flyer, flat-plate impacts were used to determine the fracture parameters for this material. Long rod penetration tests showed the occurrence of brittle fracture, the alpha-to-epsilon phase transition near the impact plane, and adiabatic shear bands near the zone of penetration.

Two-dimensional wave propagation test calculations were made with the ductile and brittle fracture models to simulate impacts in targets of 1145 aluminum, Armco iron, and XAR30 armor steel. The fracture models were found to function satisfactorily. It is concluded that the fracture models for both ductile and brittle fracture modes are operable and are suitable for insertion as subroutines into Lagrangian wave propagation codes such as HEMP.

ACKNOWLEDGEMENTS

The authors acknowledge the help of many of the staff of Poulter Laboratory in conducting the experiments and performing the analysis. P. S. De Carli conducted both the long rod and plate impact experiments. J. Wilhelm helped with the experiments and the experimental data. D. Petro cut, polished, and photographed the specimens. B. Lew measured the crack sizes and orientations. M. Austin determined the N.A.G. parameters from the crack data, incorporated the fracture models into FIBROUS, and conducted the wave propagation calculations.

CONTENTS

ILLUSTRATIONS

TABLES

I INTRODUCTION AND SUMMARY

The Army Materials and Mechanics Research Center (AMMRC) is studying several types of armor penetration problems including penetration with rods and very high velocity pellets. A basic element in the study is a computer code (HEMP[1]), which simulates the two-dimensional axisymmetric wave propagation in a penetration experiment. Present day two-dimensional Lagrangian wave propagation computer codes such as HEMP represent the gross plasticity aspects very well, and yield satisfactory predictions for cases where fracturing of the armor plate is not a significant part of the penetration process. The predictions are less satisfactory however, for cases where microcracking and shear banding dominate. The latter mechanisms become more important with increasing armor plate hardness and increasing projectile hardness and velocity, and are enhanced by certain projectile geometries. Thus it appeared necessary to account for fracture in a more detailed way.

The overall objective of the program reported here was to improve the predictive capability of HEMP for penetration calculations by incorporating into it recently developed dynamic fracture models, the SRI NAG (Nucleation And Growth) models. These models for brittle and ductile fracture[2-7] provide for the nucleation of cracks or voids, growth of these flaws during the period of tensile loading, and the reduction of stress and strength associated with the developing damage. The models appeared to be appropriate for handling the penetration problem, but they were available only in a one-dimensional form. Therefore, two of the specific objectives of the study were: (1) to modify the brittle and ductile fracture models so that they could handle two-dimensional flow and (2) to incorporate these models into subroutines for use with the HEMP code.

To be able to use a fracture model one must know the fracture parameters appropriate to materials of interest. Fracture parameters for the SRI models were available only for OFHC copper, 1145 aluminum, Lexan polycarbonate (a transparent plastic), and several grades of beryliium. Therefore, a third objective of the study was (3) to conduct impact experiments in an armor steel and derive the fracture parameters. Included in this objective was the metallographic examination of the targets to guide in derivation of the fracture models.

During this program the above objectives were largely met. The fracture models were developed and incorporated into HEMP in several stages. First the one-dimensional models were simply altered to account for two-dimensional flow. For brittle fracture this required constructing a new description of the crack size and orientation distributions. An armor steel, XAR30, was selected for characterization. Tapered-flyer impacts were conducted to determine the compressive, tensile, and fracture behavior. Rod impact experiments were conducted to study the penetration behavior. Posttest metallographic examination was made of the sectioned targets to determine qualitatively the nature of the fracture damage. For the tapered-flyer impacts the cracks were also analyzed quantitatively to determine the size and orientation distribution of cracks. From these distributions the fracture parameters were obtained for the XAR30 armor steel, (Table V). The models were then implemented and tested in a SRI two-dimensional code similar to HEMP and used to simulate successfully some impact problems (Figure 24-27). Finally, the models were modified to account for higher levels of damage. The models were then delivered to Mr. John Mescall of AMMRC for insertion into the HEMP code. At the time of writing of this report, the models for ductile and brittle fracture have been incorporated into HEMP, and test calculations have been performed.

The remainder of this report is organized in the following way. In Section II the fracture model in two space dimensions is developed and described both for brittle and ductile fracture modes. In Section III the experimental work is described, and in Section IV we present computational simulation (with the developed fracture model) of three two-dimensional impact experiments. Finally, in Section V a summary is given of the results of the program. In addition, six appendices provide additional details concerning the computational model and the experiments performed.

II MODELS FOR BRITTLE AND DUCTILE FRACTURE IN TWO SPACE DIMENSIONS

A. Introduction

Computational models describing brittle and ductile fracture were modified to include two-dimensional (planar or axisymmetric) behavior and were applied to some two-dimensional wave propagation problems.

In these computational models for fracture, damage occurs as the nucleation and growth of small voids (ductile fracture) or microcracks (brittle fracture). Nucleation may occur physically by widening of inherent flaws in the material, cracking of hard inclusions, separating along grain boundaries, or by other mechanisms. In the model, however, nucleation means the appearance of the void or crack of an observable and easily identifiable size on photomicrographs at a scale of about 100X. This nucleation occurs in the model as a function of stress and stress duration. Following nucleation, the voids or cracks grow at a rate that is dependent on the stress level, duration of loading, and the size of the void or crack. The model also accounts for the stress reduction that accompanies the development of damage.

The models developed in this work were for incipient damage and not for full separation. The brittle fracture model has been extended to full separation on a concurrent project.[8] In this extended model the microcracks coalesce and form fragments. The ductile fracture model had been previously verified for damage resulting in 10% porosity but not for greater damage. During this effort the program was modified to extend the model to full separation, but that extension has not yet been verified by correlation with experiment.

The two computational models of fracture are implemented in subroutines that may readily be inserted into two-dimensional Lagrangian wave propagation computer codes. While the material is undergoing fracture, these subroutines are called instead of the usual equation-of-state subroutines.

The analytical basis for the two models is presented below. These analyses are somewhat different from those presented earlier[2-4] because of the extension to higher damage. Details of the computational procedures used are given in Appendix A. Implementation of the models into a computer program is described in Appendix B.

B. Ductile Fracture

The ductile fracture model was formulated on the basis of observations of ductile fracture in soft aluminum[2] and copper.[3] These observations, which were made on polished cross sections of targets after impact, showed that the fracture occurred by the nucleation and growth of nearly spherical voids. The observed voids were measured and counted and assembled into number-versus-radius size distributions. These surface distributions were then transformed statistically to volumetric distributions with the BABS1[2] computer program. A sample set of void size distributions is shown in Figure 1. Curves are given for four depths within the sample; the maximum damage is at the plane F01. All the volumetric distributions obtained with aluminum and copper had a form that could be approximated by the equation

$$N_g(R) = N_o \exp(-R/R_1) \tag{1}$$

where N_g is the cumulative number/cm^3 of voids with radii larger than R, N_o is the total number of voids per cubic centimeter, and R_1 is a parameter of the distribution.

The total void volume is obtained by integrating over the entire distribution.

$$\begin{aligned} V_v &= \frac{4\pi}{3}\int_o^\infty R^3 \frac{dN}{dR}\, dR \\ &= \frac{4\pi}{3}\int_o^\infty R^3\left(-\frac{N_o}{R_1}\right) \exp(-R/R_1)dR \qquad (2) \\ &= 8\pi N_o R_1^3 \end{aligned}$$

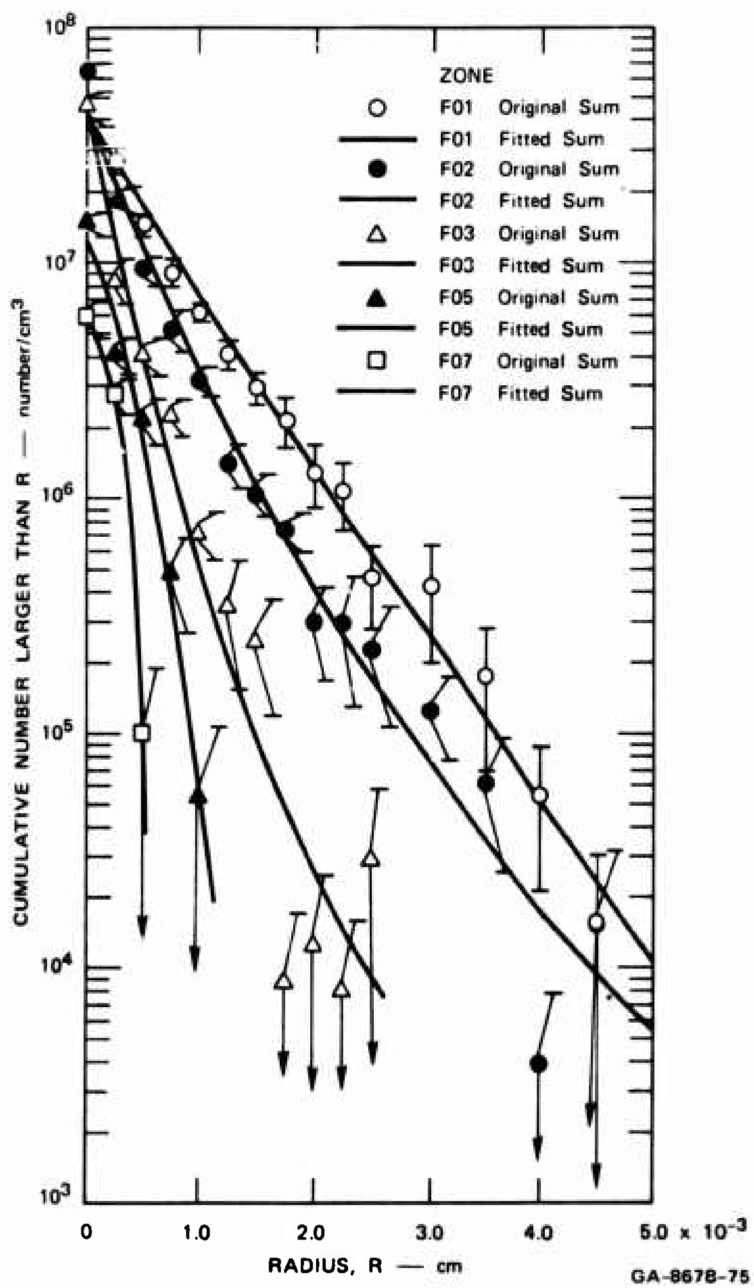

FIGURE 1 OBSERVED VOLUME DISTRIBUTION OF VOIDS ON THE FREE SURFACE SIDE OF THE SPALL PLANE IN AN OFHC COPPER TARGET AFTER A ONE-DIMENSIONAL IMPACT: EXPERIMENT S24

The void size distribution at any time and at any point can be represented by N_o and either R_1 or V_v. For computational purposes N_o and V_v are selected.

1. Nucleation: Nucleation in the model occurs as the addition of new voids to the existing set. These new voids are presumed to occur in a range of sizes with a size distribution given by Eq. (1). At nucleation, the parameter R_1 equals R_n, the nucleation size parameter (a material constant). The number of voids nucleated is governed by a nucleation rate function that was derived from our work in both ductile and brittle materials.

$$\dot{N} = \dot{N}_o \exp\left(\frac{P - P_{no}}{P_1}\right) \qquad P > P_{no} \tag{3}$$

$$= 0 \qquad P < P_{no}$$

where $\dot{N}_o$, P_{no}, and P_1 are material constants, and P is the tensile pressure. The constant P_{no} is the threshold for nucleation.

The void volume nucleated in a time interval Δt is found from Eqs. (2) and (3) to be

$$\Delta V_n = 8\pi \dot{N} \Delta t R_n^3 \tag{4}$$

2. Growth: In the model, damage increases by nucleation of new voids and by growth of the existing voids. In our studies of aluminum and copper it was found that growth was linearly dependent on the pressure level and current void size so that the growth rate $\dot{R}$ is

$$\dot{R} = \frac{P - P_{go}}{4\eta} R \tag{5}$$

where P is the tensile pressure; P_{go} is the threshold pressure for growth, and η is the material viscosity. This is the usual form for a growth law in a viscous material with no strength. In Reference 3 it is shown that Eq. (5) is accurate for small voids, but for larger radii, inertial effects reduce the velocity below that given by Eq. (5). The growth represented by Eq. (5) is spherically symmetric because the void expands equally in all directions. In Reference 3 it was shown that Eq. (5) is an appropriate description of void growth in material with strength undergoing one-dimensional planar flow as well as for spherical flow. The results of calculations described in Appendix C show that the same growth law also holds for conditions of high shear strain.

The growth of a void during a time interval Δt is obtained by integrating Eq. (5) to obtain the new radius R,

$$R = R_o \exp\left(\frac{P - P_{go}}{4\eta} \Delta t\right) \tag{6}$$

where R_o is the radius at the beginning of the time interval. Since every void in the distribution grows by the same exponential factor, the size parameter R_1 also grows according to Eq. (6).

$$R_1 = R_{10} \exp\left(\frac{P - P_{go}}{4\eta}\right)\Delta t \tag{7}$$

where R_{10} is the size parameter at the beginning of the time interval. Then the new void volume can also be found from Eqs. (2) and (7),

$$\begin{aligned} V_v &= 8\pi N_o R_1^3 \\ &= V_{vo} \exp\left(3\frac{P - P_{go}}{4\eta}\right)\Delta t \end{aligned} \tag{8}$$

where $V_{vo} = 8\pi N_o R_{10}^3$, the void volume at the beginning of the time interval.

The total change in void volume is the sum of the contributions associated with nucleation and growth. Thus the total volume at the end of the interval is

$$V_{v1} = V_{vo} \exp\left(3\frac{P - P_{go}}{4\eta} \Delta t\right) + \Delta V_n \tag{9}$$

For simplicity in the computer calculations, a new variable T_1 is introduced with the definition

$$T_1 = \frac{3}{4\eta} \tag{10}$$

3. <u>Pressure-Volume Relation</u>: The stress-strain relations for material undergoing fracture account for the presence of voids. As usual, the stress is separated into pressure and deviatoric components. The deviatoric stress-strain relations are described in the following subsection.

The pressure is related to the specific volume and internal energy through a combination of the Mie-Grüneisen equation of state for the solid and a relation between pressure in the solid and average pressure on the porous material. We assume that an average pressure in the solid material can be computed from the specific volume of the solid and the internal energy through use of the Mie-Grüneisen equation:

$$P_s = (C\mu + D\mu^2 + S\mu^3)\left(1 - \frac{\Gamma\mu}{2}\right) + \Gamma\rho_s E \tag{11}$$

where C, D, and S are constants, Γ is the Grüneisen ratio, E is internal energy, ρ_s is the solid density, and μ is the strain: $\mu = \rho_s/\rho_o - 1$, where ρ_o is the initial density of the solid. Here we neglect all nonlinear terms in μ because the solid strains and stresses are all small during fracture, and obtain

$$P_s = C\left(\frac{\rho_s}{\rho_o} - 1\right) + \Gamma\rho_s E \tag{12}$$

The pressure computed from Eq. (12) is necessarily an average because the actual stress states will vary greatly through partially fractured material.

The average pressure on the gross section of the fracturing material can now be related to the pressure in the solid components according to a relation derived by Carroll and Holt[9] for porous material:

$$P = \frac{P_s V_s}{V} \tag{13}$$

where P is the average pressure on a section, V_s is the specific volume of the solid, and V is the gross specific volume. The volume V is the sum of the solid volume V_s and the volume V_v associated with voids. A combination of Eqs.(12) and (13) serves to evaluate the pressure:

$$P = C\left(\frac{\rho}{\rho_o} - \frac{\rho}{\rho_s}\right) + \Gamma \rho E \tag{14}$$

These equations may also be inverted to obtain expressions for the specific volume of the solid in terms of P_s or P.

$$V_s = \frac{\dfrac{1}{\rho_o} + \dfrac{\Gamma E}{C}}{1 + \dfrac{P_s}{C}} \tag{15}$$

$$V_s = \frac{1}{\rho_o} - \frac{P}{C\rho} + \frac{\Gamma E}{C} \tag{16}$$

The change in solid volume ΔV_s is related approximately to the change in solid pressure ΔP_s by differentiation of Eq.(15)

$$\Delta V_s = V_{so} \frac{\Gamma \Delta E - V_{so} \Delta P_s}{C/\rho_o + \Gamma E} \tag{17}$$

where V_{so} is the specific volume of the solid at the previous time step and ΔE is the change in internal energy during the time step.

4. <u>Deviator Stress Computation in Two Dimensions</u>: The deviator stresses are first computed elastically.

$$\sigma'_{ij} = \sigma'_{ijo} + 2G\left(\Delta\epsilon_{ij} - \frac{\delta_{ij}}{3}\sum \Delta\epsilon_{ii}\right) \tag{18}$$

where G is shear modulus, $\Delta\epsilon_{ij}$ is the strain increment tensor, and

δ_{ij} is the Kronecker delta. In the fracture routines all stresses (and pressures) are positive in compression. It is noted here that in HEMP, BFRACT, and DFRACT,

$$TXY = \sigma'_{12}$$

and

$$EXY = \epsilon_{12} + \epsilon_{21} = 2\epsilon_{12}$$

If yielding occurs, then the deviator stresses are computed by the visco-plastic relation

$$\sigma'_{ij} = Y \frac{d\epsilon^p_{ij}}{d\gamma^p} + 2\eta \left(\frac{d\epsilon_{ij}}{dt} - \frac{\delta_{ij}}{3} \sum \frac{d\epsilon_{ii}}{dt} \right) \tag{19}$$

where $d\epsilon^p_{ij}$ is the ij component of the plastic strain increment and $d\gamma^p$ is the scalar "effective" plastic strain increment. Equation (19) is solved for the deviator stresses by using Wilkins' procedure[1] to handle the first term on the right side. Then

$$\sigma'_{ij} = \frac{Y}{\bar{\sigma}^E} \sigma'^E_{ij} + 2\eta \left(\frac{d\epsilon_{ij}}{dt} - \frac{\delta_{ij}}{3} \sum \frac{d\epsilon_{ii}}{dt} \right) \tag{20}$$

where σ'^E_{ij} = deviator stress from Eq. (18) and

$$\bar{\sigma}^E = \sqrt{\frac{3}{2}} \sqrt{\sum \sigma^2_{ii} + 2 \left(\sigma^2_{12} + \sigma^2_{23} + \sigma^2_{13} \right)}$$

The damage that occurs is presumed to affect both the yield strength and the effective shear modulus of the material. The modulus is reduced as a function of the developing porosity in accordance with the elastic relations of MacKenzie.[10] His formulation, in the present nomenclature, is

$$G = G_o \left[1 - V_v \rho F\right] \tag{21}$$

where G is the effective shear modulus, G_o and C are shear and bulk moduli of the solid, V_v is the specific volume of voids, ρ is the gross density, and

$$F = 5\left(\frac{3C + 4G_o}{9C + 8G_o}\right) = 15\,\frac{(1 - \nu)}{(7 - 5\nu)} \qquad (22)$$

where ν is Poisson's ratio.

The factor F varies only from 2.14 to 1.66 as ν ranges from 0 to 0.5. In the fracture subroutine F is called SMF and is inserted with a value of 1.88 corresponding to $\nu = 1/3$.

The yield strength reduces somewhat more rapidly than the modulus as the porosity increases. Dynamic calculations of void growth by Seaman et al.[3] indicated that the yield strength should reduce in the following way.

$$Y = Y_o[1 - 4V_v\rho] \qquad (23)$$

This expression is used in the fracture subroutine.

C. Brittle Fracture

The brittle* fracture model was formulated on the basis of observations of fracture in Armco iron,[3,4] beryllium,[4] novaculite[6] (a fine-grained quartz), and Lexan polycarbonate[5] (a transparent plastic). In impact experiments with these materials, fracture occurred by the nucleation and growth of microcracks. These cracks were measured for length and angular orientation with respect to the direction of loading. The observed cracks were then organized into groups according to size interval and angle interval. These surface distributions were then transformed statistically to volumetric distributions in size and angle with the BABS2[3] computer program. For this transformation it was assumed that the cracks were penny-shaped and that the distribution was axisymmetric around the direction of propagation. A sample set of crack distributions is shown

* Fracture was termed brittle whenever the primary damage mode appeared as cracks. In many cases, such as Armco iron, the cracks grew in what is often termed a "ductile" manner.

in Figure 2. Here the angular variation has been suppressed, so the ordinate is the total number of cracks larger than the indicated radius. The volumetric distributions obtained with Armco iron had the same exponential form found for voids. In addition to a size distribution, it was necessary to consider an orientation distribution. Furthermore, as the material rotates (as it does at the rear of a plate under projectile impact) the cracks rotate with the material.

Considering the requirements for size and orientation distributions and for permitting rotation, the fracture model was constructed with an array of crack orientations or "bins" associated with each computational cell. Each crack bin contains penny-shaped cracks with a specific orientation and with a specific size distribution.

The size distribution for each bin in the model is given the following analytical form

$$N_g^i = N_o^i \exp(-R/R_1^i) \tag{24}$$

where N_o^i is the total number of cracks per cubic centimeter in the i^{th} bin, N_g^i is the number of cracks with radii greater than R, and R_1^i is a constant giving the shape of the crack size distribution in the i^{th} bin.

Each bin contains cracks normal to a specific angle φ (in the x, y plane) and ψ (in planes normal to the x,y plane) as shown in Figure 3. At present only four values of φ (0°, 45°, 90°, 135°) and two of ψ (0°, 90°) are used. For example, bin 1 contains all cracks with φ between -22.5° and 22.5° and ψ between 45° and 135°. Note that cracks with φ between 157.5° and 202.5° are included in this bin. Bin 5 contains all cracks with ψ less than 45° or greater than 135°. In the model calculations the cracks are treated as though they all had orientations corresponding to the center of the bin ($\varphi = 0^\circ$, $\psi = 90^\circ$ for bin 1, $\psi = 0^\circ$ for bin 5, and so on.) Experience will show whether five is a large enough number of bins.

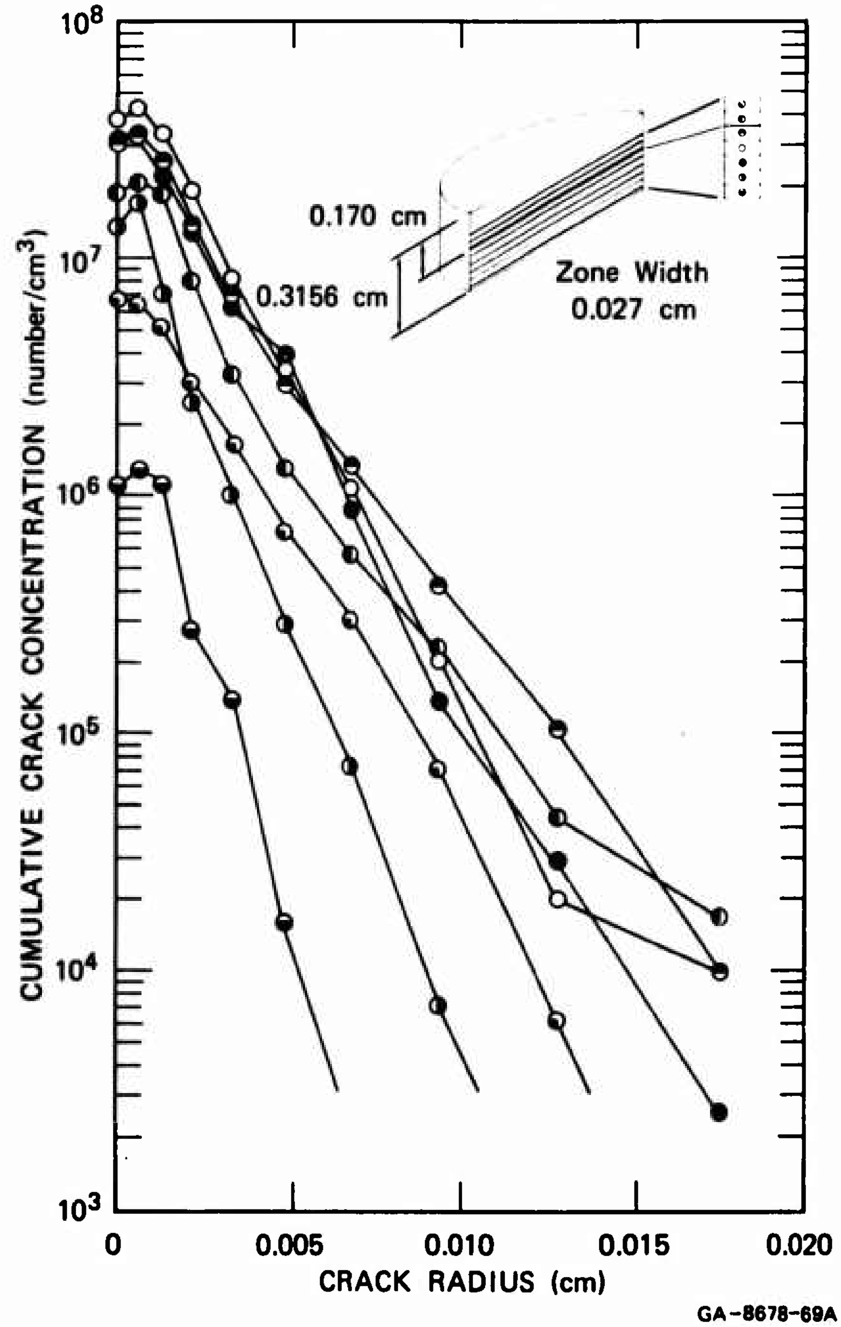

FIGURE 2 CRACK SIZE DISTRIBUTION IN ZONES NEAR THE SPALL PLANE IN AN ARMCO IRON TARGET AFTER A ONE-DIMENSIONAL IMPACT: EXPERIMENT S25

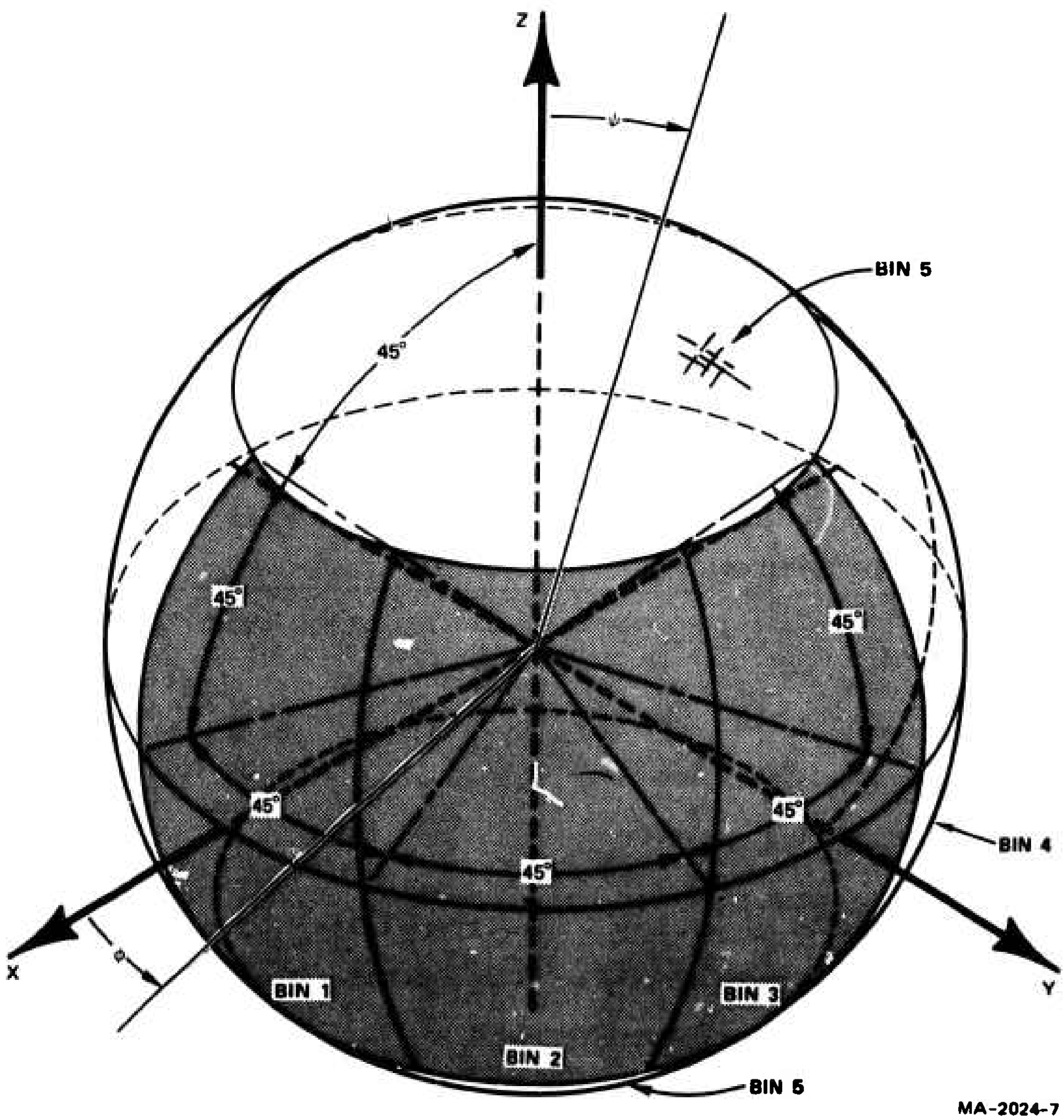

FIGURE 3 CRACK ORIENTATION BINS AND DEFINITIONS OF ϕ AND ψ

In two-dimensional axisymmetric or planar flow, the cells may rotate in the x-y plane. This rotation is accounted for by allowing the crack bins to rotate with the material. The angular rotation is given by the variable ρ_t. The position of the i^{th} bin in the x-y plane is then given by

$$\varphi_i = \varphi_{io} + \rho_t \tag{25}$$

where φ_i is the current angular position and φ_{io} its initial position. At the end of a computation ρ_t is listed so that the bin orientations can be related to the fixed x-y grid. The crack bin rotation is independent of the initial orientation of the computational cell and of rotations that the cell undergoes before fracture begins.

The stresses applied normal to the cracks in each bin are determined by the usual transformations for two-dimensional problems. The stress in the Z direction is always a principal stress. These normal stresses, which govern nucleation, growth, and expansion of the cracks are

$$\sigma_{\varphi\psi} = \frac{\sigma_x + \sigma_y}{2} + \frac{\sigma_x - \sigma_y}{2} \cos 2\varphi_i + \tau_{xy} \sin 2\varphi_i \quad (\text{for } \psi = 90^\circ) \tag{26}$$

$$\sigma_{\varphi\psi} = \sigma_Z \quad (\text{for } \psi = 0^\circ) \tag{27}$$

If the cell rotates by an angle ρ_t (positive counterclockwise), then the angle to the crack group becomes $\varphi_{io} + \rho_t$ for the set of groups at $\psi = 90^\circ$. Then Eq. (26) is used, with φ_i determined by Eq. (25).

The cracks are presumed to open elastically to the value given by Sneddon[11]

$$\delta = \frac{4(1 - \nu^2)}{\pi E} R \, \sigma_{\varphi\psi} \tag{28}$$

where δ is one-half the maximum separation of the crack faces and E is Young's modulus. The crack faces form an ellipsoid with three semi-axes δ, R, and R. Then the volume of a crack is

$$V_{1c} = \frac{16(1 - \nu^2)}{3E} R^3 \sigma_{\varphi\psi} \tag{29}$$

The volume of the entire crack distribution is obtained by combining Eqs. (24) and (29) into the following integral:

$$V = \sum_i V^i = \sum_i \int_o^\infty V_{1c} \frac{d[N_o^i \exp(-R/R_1^i)]dR}{dR}$$

$$= \frac{32(1 - \nu^2)}{E} \sum_i N_o^i (R_1^i)^3 \sigma_{\varphi\psi}^i \tag{30}$$

1. Crack Nucleation: Nucleation in the model occurs as the addition of new cracks to the existing set. These new cracks are presumed to occur in a range of sizes with a size distribution like Eq. (24). At nucleation, the parameter R_1^i equals R_n, the nucleation size parameter (a material constant). The number of cracks nucleated is governed by a nucleation rate function similar to that used for ductile fracture:

$$\dot{N} = \dot{N}_o \exp\left(\frac{\sigma_{\varphi\psi} - \sigma_{no}}{\sigma_1}\right) \tag{31}$$

where $\dot{N}_o$, σ_{no}, and σ_1 are fracture parameters and $\sigma_{\varphi\psi}$ is stress normal to the plane of the cracks. This form of nucleation function resembles the relation deduced by Zhurkov[12] for the rate of breakage of atomic bonds. We have found it applicable to ductile materials and also to such diverse brittle materials as Armco iron,[3] beryllium,* polycarbonate,[5] and a three-directionally reinforced quartz phenolic composite.[13] The new cracks are

* In beryllium[4] it was found that the deviator stress governs nucleation and not the stress $\sigma_{\varphi\psi}$.

nucleated with a range of sizes such that the number greater than R is

$$\Delta N_g^i = \dot{N}^i \Delta t \exp(-R/R_o) \tag{32}$$

where $\dot{N}^i \Delta t$ is the total number nucleated in the i^{th} bin, R_o is the nucleation distribution parameter, and Δt is the time step. The volume of the entire nucleated distribution is obtained by combining Eqs. (30) and (32).

$$V_n = \sum V_n^i = \sum_i \int_o^\infty V_{1c} \frac{d[\dot{N}^i \Delta t \exp(-R/R_o)]dr}{dr}$$

$$= \frac{32(1 - \nu^2)\, \Delta t\, R_n^3}{E} \sum_i \dot{N}^i \sigma_{\varphi\psi}^i \tag{33}$$

If the material is isotropic and under a uniform tensile stress, nucleation of cracks occurs with equal probability in any direction. In such a case the number of cracks assigned to each bin is proportional to the solid angle subtended by the bin. The fraction of the total solid angle for each bin is called FNUC in the fracture subroutine: it is now set for isotropic nucleation. If the material is not isotropic, FNUC can be altered to reflect the observed flaw orientations.

2. Crack Growth: The growth law derived from experimental data on both ductile and brittle fracture is:[4]

$$\frac{dR}{dt} = T_1 (\sigma - \sigma_{go})R \tag{34}$$

where T_1 is a growth coefficient and σ_{go} is the growth threshold stress, Here σ_{go} is treated as a constant material parameter, but in some cases it has been taken as the critical stress for crack growth according to fracture mechanics

$$\sigma^*_{go} = \frac{\pi}{4R} K_{Ic} \tag{35}$$

where K_{Ic} is the fracture toughness. Since σ^*_{go} is generally very small for impact problems, σ_{go} in Eq. (34) can usually be taken as a small constant.

When Eq. (34) is integrated over a time step Δt (holding σ_{go} constant), the final value of the radius is

$$R = R_1 \exp\left[T_1(\bar{\sigma}_{\varphi\psi} - \sigma_{go})\Delta t\right] \tag{36}$$

where R_1 is the radius at the beginning of the interval and $\bar{\sigma}_{\varphi\psi}$ is the average stress in the interval. When Eq. (30) is combined with Eq. (36) the crack volume associated with growth at the end of the time step is found to be

$$V^i_g = 32N^i_o \frac{(1 - \nu^2)}{E} (R^i_1)^3 \sigma^i_{\varphi\psi} \exp\left[3T_1(\bar{\sigma}^i_{\varphi\psi} - \sigma_{go})\Delta t\right] \tag{37}$$

The total number of cracks in the i^{th} bin at the end of the time step is

$$N^i_1 = N^i_o + \dot{N}^i \Delta t \tag{38}$$

The total volume V^i_t may be represented as the sum of V^i_n and V^i_g from Eqs. (33) and (37), or the combination of cracks may be described by a single analytical form with N^i_1 cracks and a new shape parameter R^i_2

$$V^i_t = V^i_n + V^i_g \tag{39}$$

or

$$V^i_t = 32\, N^i_1 \cdot \frac{(1 - \nu^2)}{E} (R^i_2)^3 \sigma^i_{\varphi\psi} \tag{40}$$

Equating the two expressions for V_t^i provides a means for evaluating R_2^i, the distribution parameter appropriate to the end of the time step.

$$(R_2^i)^3 = \frac{N_o^i (R_1^i)^3 \exp\left[3T_1 (\bar{\sigma}_{\varphi\psi}^i - \sigma_{go}) \Delta t\right] + \dot{N}^i \Delta t\, R_o^3}{N_1^i} \tag{41}$$

Now the damage at the end of the time step can be completely characterized by two parameters, N_1^i and R_2^i, obtained from Eqs. (38) to (41).

3. <u>Stress-Strain Relations</u>: The stress-strain relations for material undergoing brittle fracture are the same as those for ductile fracture. The void volume is replaced by the crack opening volume in the equations. Because the crack opening volume is small, the usual stress-strain relations are modified very little by the damage.

For the stress calculation, the damage is treated as if it were isotropic. Future modifications may be made to account for the anistropic nature of the damage.

4. <u>Implementation in the Computer Program</u>: The foregoing analyses set forth the basic equations describing nucleation and growth of voids and cracks, and the damage-caused modifications of the stress-strain relations. These equations are used directly in the computer subroutines. Further derivations required for the numerical procedures in the subroutine are described in Appendix A. The subroutine and test cases for it are given in Appendix B.

III EXPERIMENTAL INVESTIGATION

The purpose of the experimental program was to examine qualitatively and quantitatively the nature of fracture in one armor steel. The steel selected was a high-hardness armor steel designated XAR30. The dynamic experiments were tapered-flyer impacts and long rod penetration tests.

The tapered-flyer impacts were conducted to determine both the Hugoniot (stress-strain character under compression) and the fracture (NAG) parameters in tension. These impacts were instrumented with stress gages at the rear of the target to obtain the needed Hugoniot data. The targets were sectioned, and the crack size and orientation distributions were measured; from these distributions the NAG fracture parameters were obtained.

Long rod penetration tests were conducted to provide both qualitative guidance in developing the two-dimensional fracture model and a test case for future computer simulation. Besides tests on XAR30 targets, penetration tests were also made with 1145 aluminum and Armco iron, two materials whose fracture behavior was already well characterized. The aluminum and Armco iron tests are described in Appendix D.

For further insight into the basic mechanisms associated with penetration, posttest observations were made on targets of an improved homogeneous steel (IHS) following penetration experiments. These results are described in Appendix E. The micromechanics of the fracture behavior of the XAR30 and IHS steels and Armco iron are compared in Appendix F.

A. Materials

High-hardness armor steel made by Great Lakes Steel Company and United States Steel Company and designated as XAR30 was used in this work. The chemical compositions reported by Hickey[14] are given in Table I, and tensile properties are given in Table II. The microstructures

Table I

CHEMICAL COMPOSITION OF XAR30 ARMOR STEEL
(Weight percent)

Supplier	C	Mn	P	S	Si	Cr	Mo	Zr	B	Ni
Great Lakes Steel	0.28	0.94	0.010	0.025	0.66	0.59	0.21	0.14	0.0014	--
U.S. Steel	0.29	0.83	0.007	0.010	0.60	0.49	0.41	0.16	--	1.05

Table II

TENSILE PROPERTIES OF XAR30 ARMOR STEEL*

Supplier and Orientation	0.2% Yield Strength (ksi)	Tensile Strength (ksi)	Elongation (%)	Reduction in Area (%)
Great Lakes Steel				
Longitudinal	208	262	14.5	49.8
Long transverse	216	253	10.5	39.8
Short transverse*	211	261	10.0	12.5
U.S. Steel				
Longitudinal	201	231	11.5	47.8
Long transverse	204	241	11.0	44.0

* Short transverse properties are the average of three tests performed at SRI and described more fully in Appendix E. All other values are the average of two tests performed by Hickey.[14]

of both materials appear to be a mixture of martensite, bainite, and retained austenite. Fracture toughness testing by Hickey indicated that the United States Steel material was slightly tougher than the Great Lakes Steel material.

The Vickers hardness of the material was measured to be 545 (corresponding to R_c 52 and BHN 509) and differed by less than 3% on three mutually perpendicular faces. Small unconventional tensile specimens were prepared from the half-inch plates in the plate thickness direction, and the short transverse tensile properties were measured. The results are summarized in Table II and described in more detail in Appendix E. The strengths and elongations are essentially the same in all three directions in the steel, but the reduction in area at failure is much smaller in the short transverse tests.

B. Flat Plate, Tapered-Flyer Impact Experiments

Five flat plate impact experiments were performed with the gas gun to establish the dynamic fracture behavior of XAR30 armor steel. The experimental configurations are given in Table III. The objective of the first two experiments was to measure the load history; the objective of the remaining three experiments was to produce different degrees of fracture damage that could later be quantified. As discussed in Section IV, the measured load histories are correlated with the fracture damage to obtain parameters that describe the dynamic fracture behavior.

The experimental arrangement is shown in Figure 4. Specimen disks 1.5 inches in diameter were machined to various thicknesses (see Table III) and mounted in the target plate. The edges were beveled at an 8 degree angle to allow the specimen to release easily from the target plate upon impact and fly into the rags of the catcher tank.

Tapered flyer plates 2¼ inches in diameter and having an average thickness half that of the specimen were machined from the same material

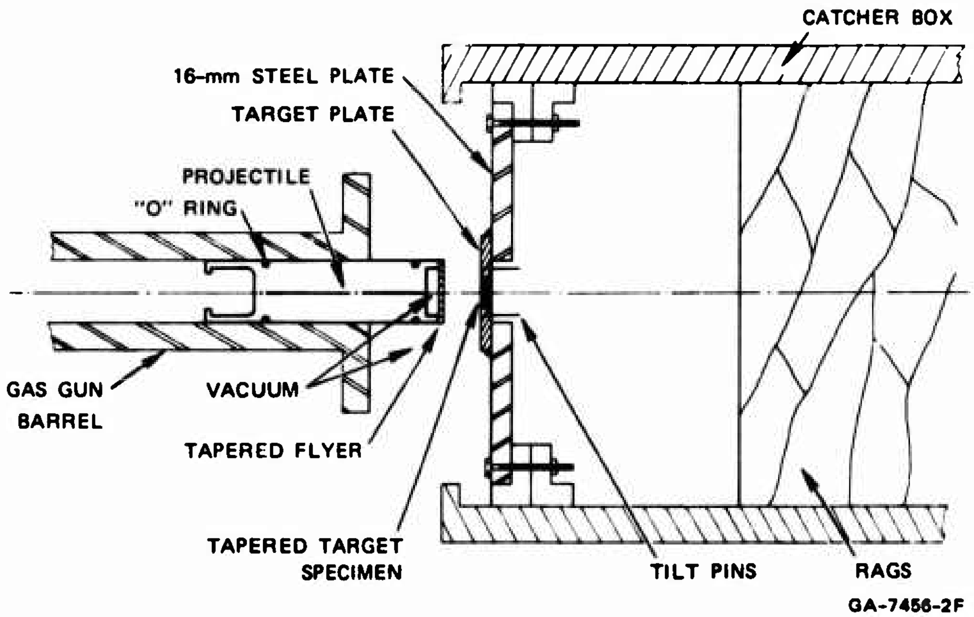

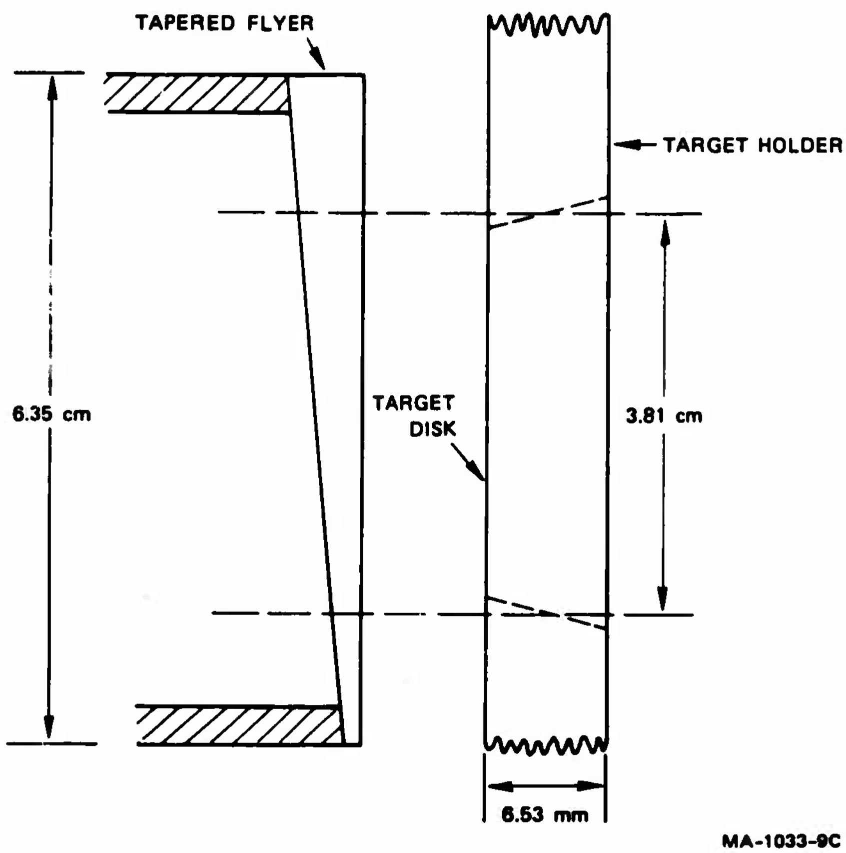

FIGURE 4 EXPERIMENTAL ARRANGEMENT FOR TAPERED-FLYER IMPACT EXPERIMENTS

Table III

DYNAMIC FRACTURE EXPERIMENTS ON XAR30 ARMOR STEEL

Experiment Number	Specimen Thickness (mm)	Flyer Thickness at Center (mm)	Angle of Taper (deg)	Flyer Velocity (mm/μsec)	Remarks
2024-1*	7.62	3.81	5.7°	0.451	Full spall; clear gage record
2024-2*	10.1	4.44	5.7	0.357	Large continuous fracture; clear gage record
2024-3	5.08	2.24	5.7°	0.226	Numerous microfractures
2024-4	12.1	5.58	6.84°	0.200	Numerous microfractures
2024-5	2.54	1.12	2.3°	0.259	Numerous microfractures

* Instrumented with back surface ytterbium piezoresistive stress transducers.

and mounted on the front of a 6-inch-long aluminum projectile. The angle of taper varied for different experiments from 2.3 to 6.8 degrees as shown in Table III. The impacting surfaces were ground flat and parallel to within 0.0005 inch.

The projectile was accelerated down the barrel of the gas gun upon sudden release of compressed helium, and careful alignment of the flyer plate and specimen resulted in flat plate impact. The impact velocity was measured by electrical contacts at the gun muzzle.

Since the stress duration in the specimen varies according to flyer thickness, tapered flyer experiments have the advantage over untapered flyer experiments in that a range of stress durations can be obtained in one experiment. Since the extent of dynamic fracture damage depends on stress duration as well as on the magnitude of the stress, a range of damage can be produced in a single experiment.

Analysis of the stress history for a tapered flyer experiment is more complicated than for the uniaxial strain conditions resulting from untapered flyer impact, because a shear wave arises when the dilatational wave reflects from the inclined rear surface of the flyer. A two-dimensional (planar) wave propagation code, however, was used successfully to compute the stress histories and damage. This analysis is described in Section IV.

Wave profiles were recorded close to the rear surface of two of the specimens. Ytterbium piezoresistive stress transducers, mounted in 3/8-inch thick blocks of C-7 epoxy that were glued to the specimens, produced the oscilloscope traces shown in Figure 5. Both records show the Hugoniot elastic limit (HEL), a flat-topped loading wave, and a clear fracture signal. The HEL measures the yield strength of the material under dynamic uniaxial strain conditions and is useful in specifying the constitutive equation of the armor. The flat-topped

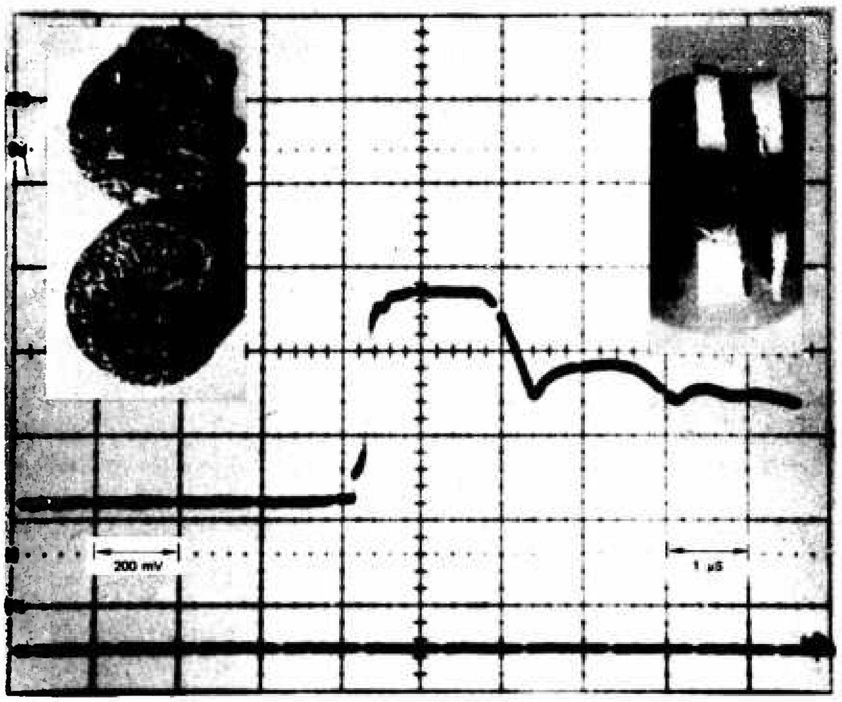

(a)

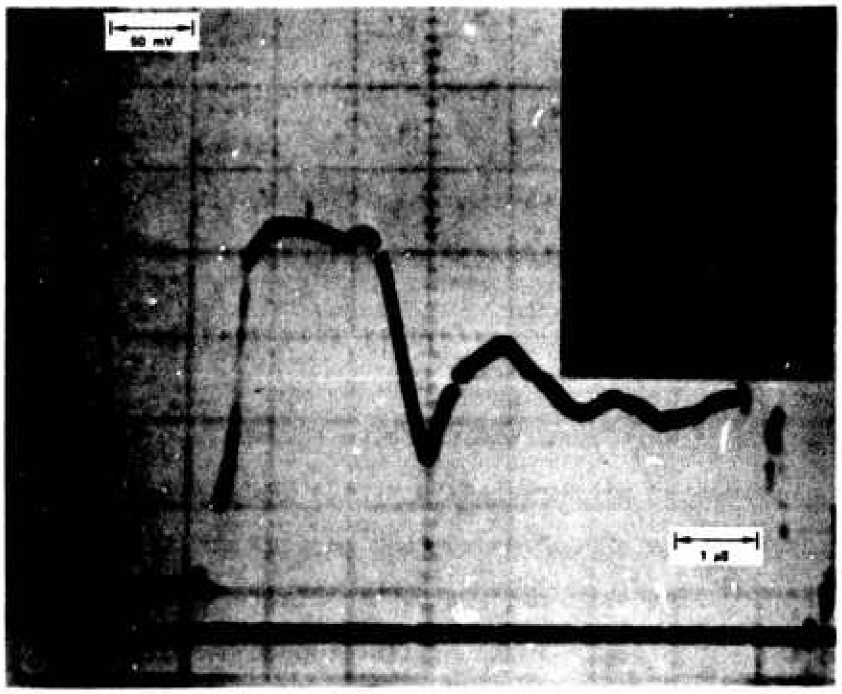

(b)

MP-2024-8

FIGURE 5 VOLTAGE-TIME RECORDS FROM YTTERBIUM STRESS GAGES IN PMMA ATTACHED TO THE BACK SURFACES OF FLAT PLATE IMPACT SPECIMENS loading wave indicates that impact planarity was good and that significant attenuation did not occur before fracture. The second peak in the records, known as the fracture signal, is caused by a reloading recompression of the transducers by waves emanating from the internal fracture surfaces as they form and grow.

Shock absorbing materials were located in the path of the impacted specimen to decelerate it gradually and prevent subsequent shock loads. The recovered specimens were then sectioned to reveal the internal fracture damage as shown in Figure 6. Specimens 2024-3 and 2024-4 were sectioned so as to produce a cross section in the direction of maximum taper (see insets in Figures 7 through 11; Specimen 2024-5 was sectioned parallel to the direction of taper at three locations (see inset in Figures 12 and 13).

The fracture damage in Specimens 2024-3, 2024-4, and 2024-5 was analyzed quantitatively by counting and measuring the traces of the microfractures on the polished section surfaces. Measurements were made by using a large area record reader (LARR) with which an operator positions a cross hair on one end of a crack trace, pushes a button to record the coordinates, and repeats the process for the other end. A simple computer program uses these data to compute the length, orientation, and position within the specimen of the trace. If desired, a similar procedure can be used to obtain crack widths. The size distributions on the sectioned surfaces are then converted to actual crack size distributions per unit volume by means of a statistical transformation implemented in the BABS2 computer code. This procedure is described in detail in Reference 3.

The results of this quantitative damage analysis are presented in Figure 7 through 13, which show crack size distribution curves for various positions on a cross section for several cross sections in Specimens 2024-3, 2024-4, and 2024-5. No fracture damage was observed for section C-C of Specimen 2024-5.

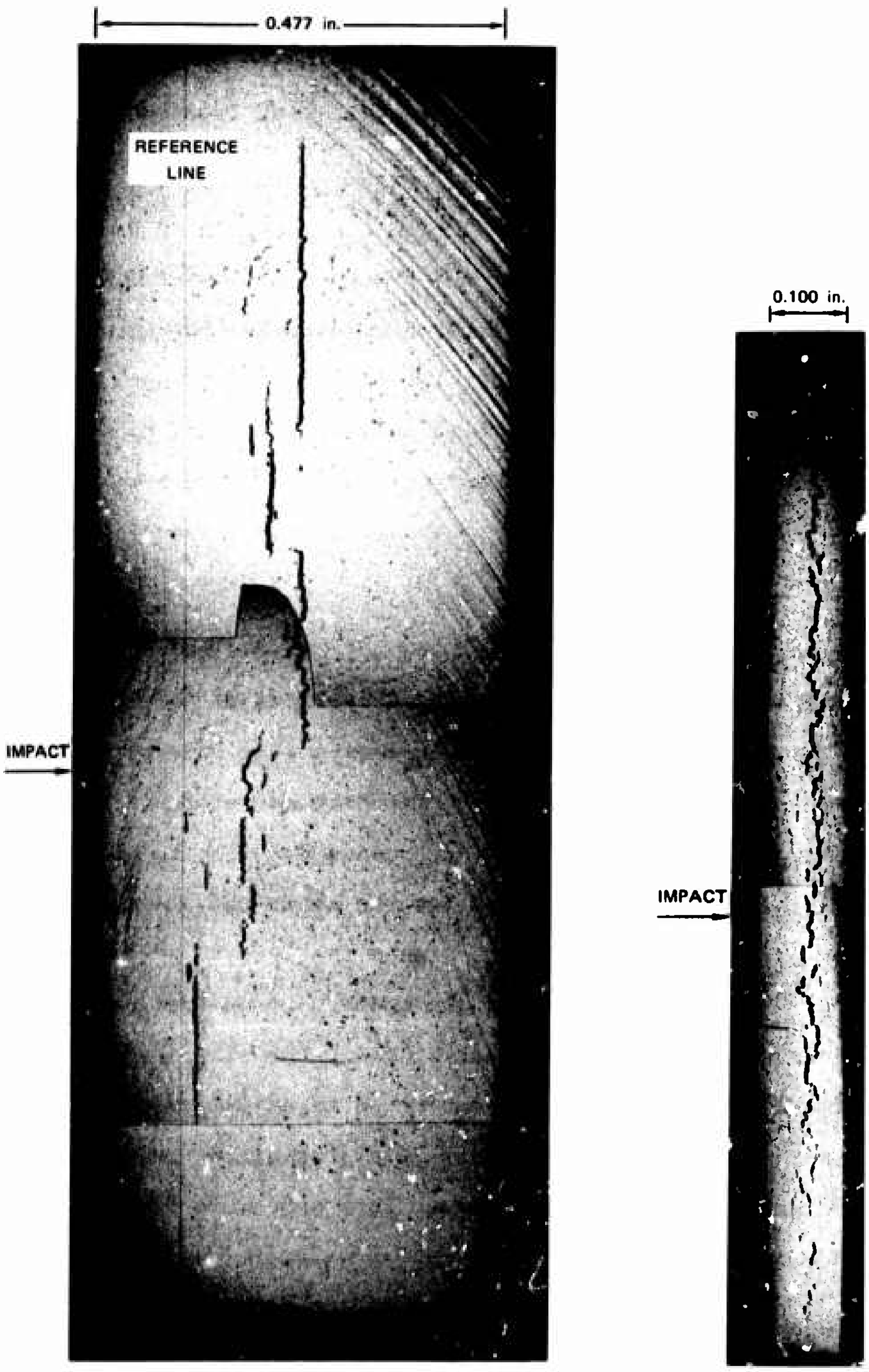

(a) SPECIMEN 2024-4, SECTION A-B
(Surface is parallel to taper of flyer)

(b) SPECIMEN 2024-5, SECTION A-A
(Surface is perpendicular to taper of flyer)

MP-2024-16

FIGURE 6 POLISHED CROSS SECTIONS SHOWING INTERNAL SHOCK-INDUCED FRACTURES

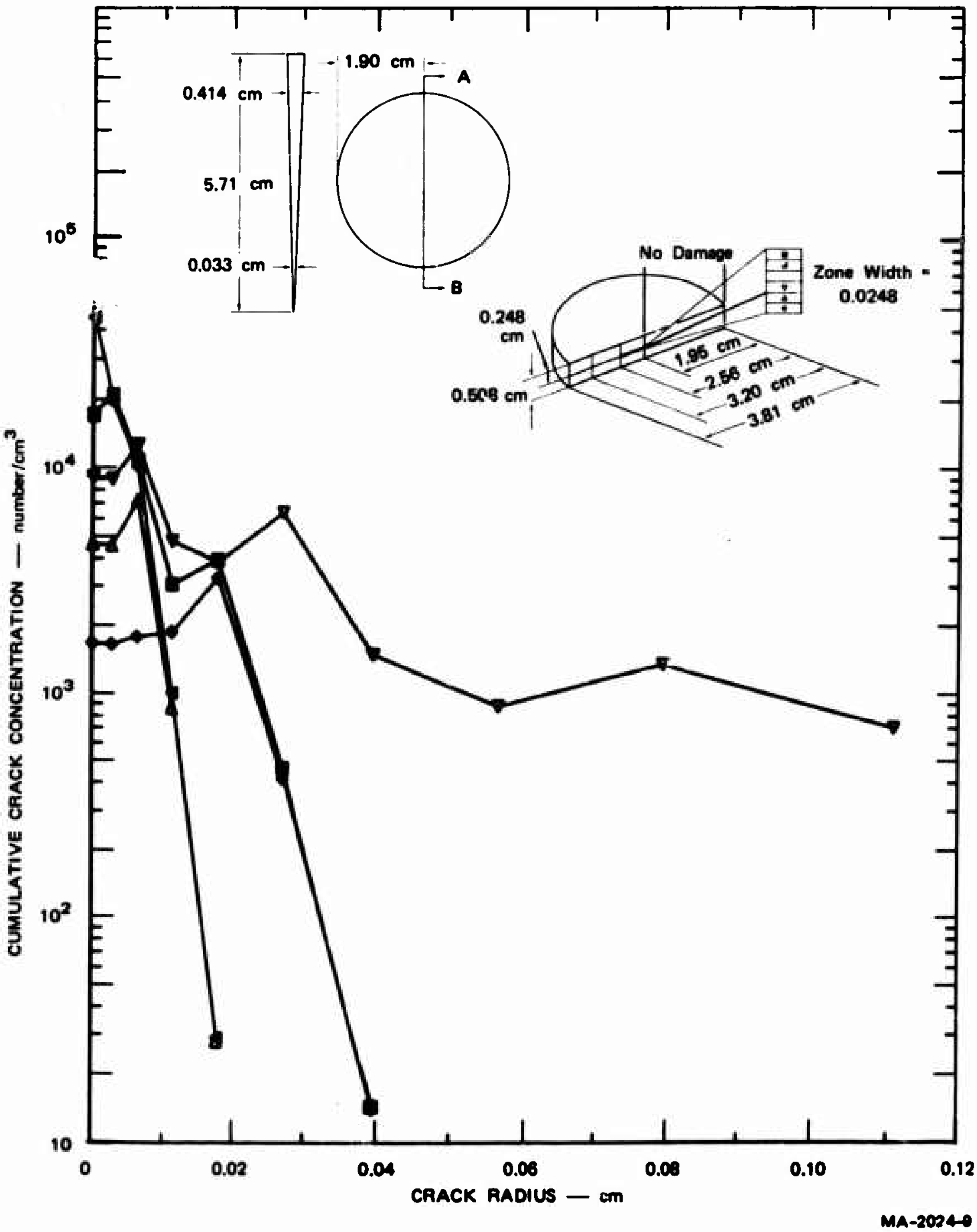

FIGURE 7 CRACK SIZE DISTRIBUTIONS ON SECTION A-B, FILE 1 OF SPECIMEN 2024-3

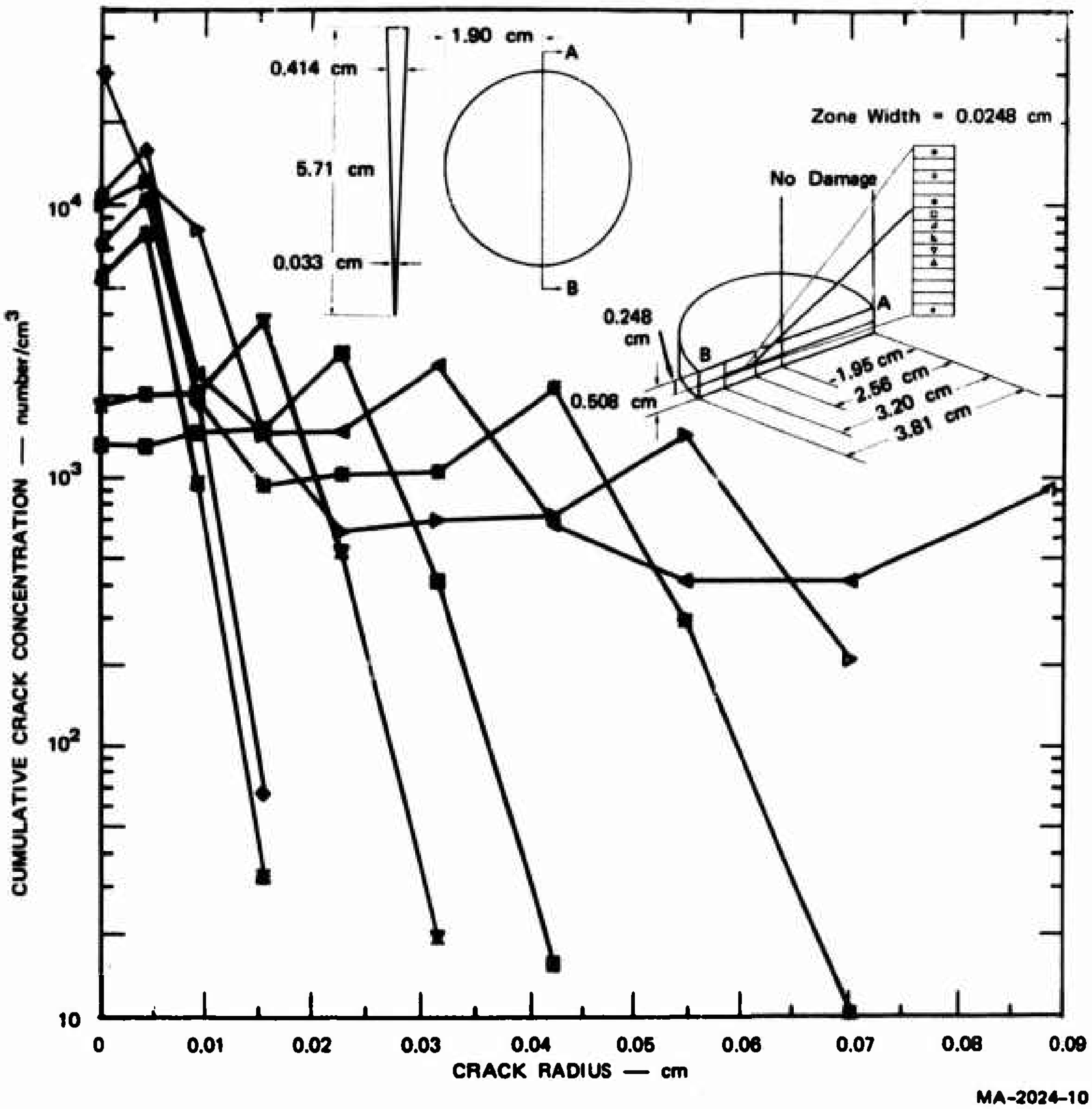

FIGURE 8 CRACK SIZE DISTRIBUTIONS ON SECTION A-B, FILE 2 OF SPECIMEN 2024-3

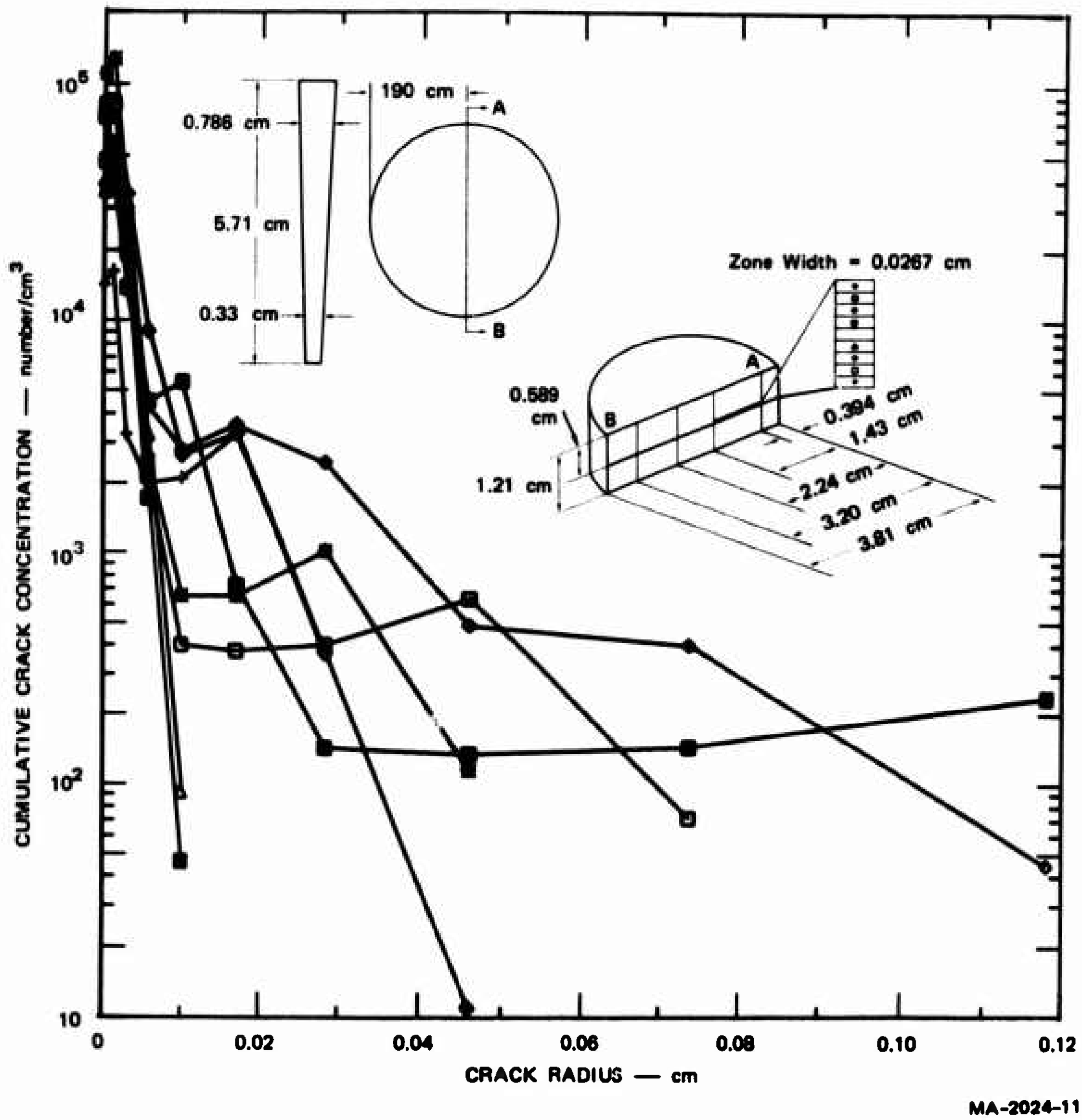

FIGURE 9 CRACK SIZE DISTRIBUTIONS ON SECTION A-B, FILE 1 OF SPECIMEN 2024-4

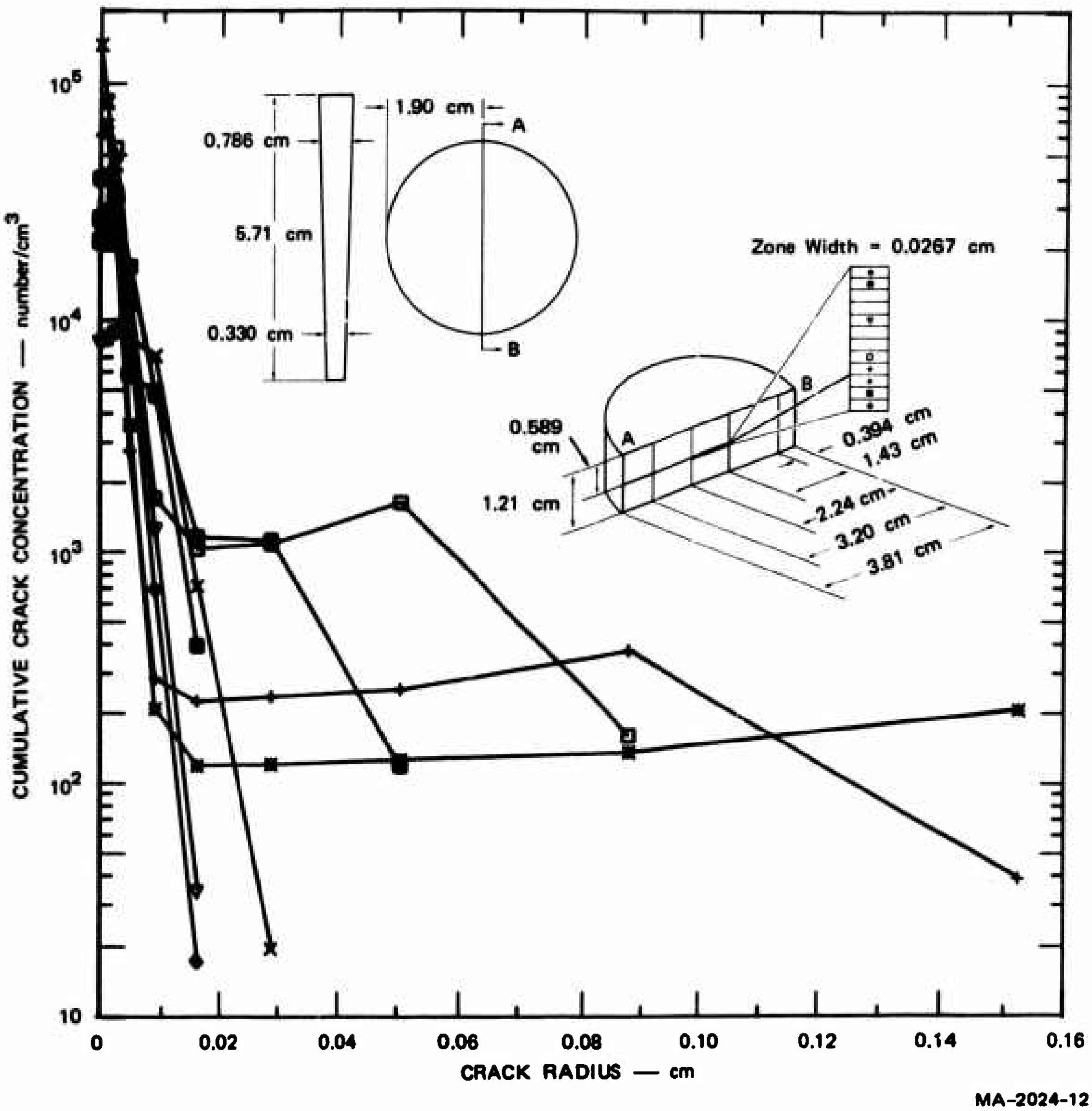

FIGURE 10 CRACK SIZE DISTRIBUTIONS ON SECTION A-B, FILE 2 OF SPECIMEN 2024-4

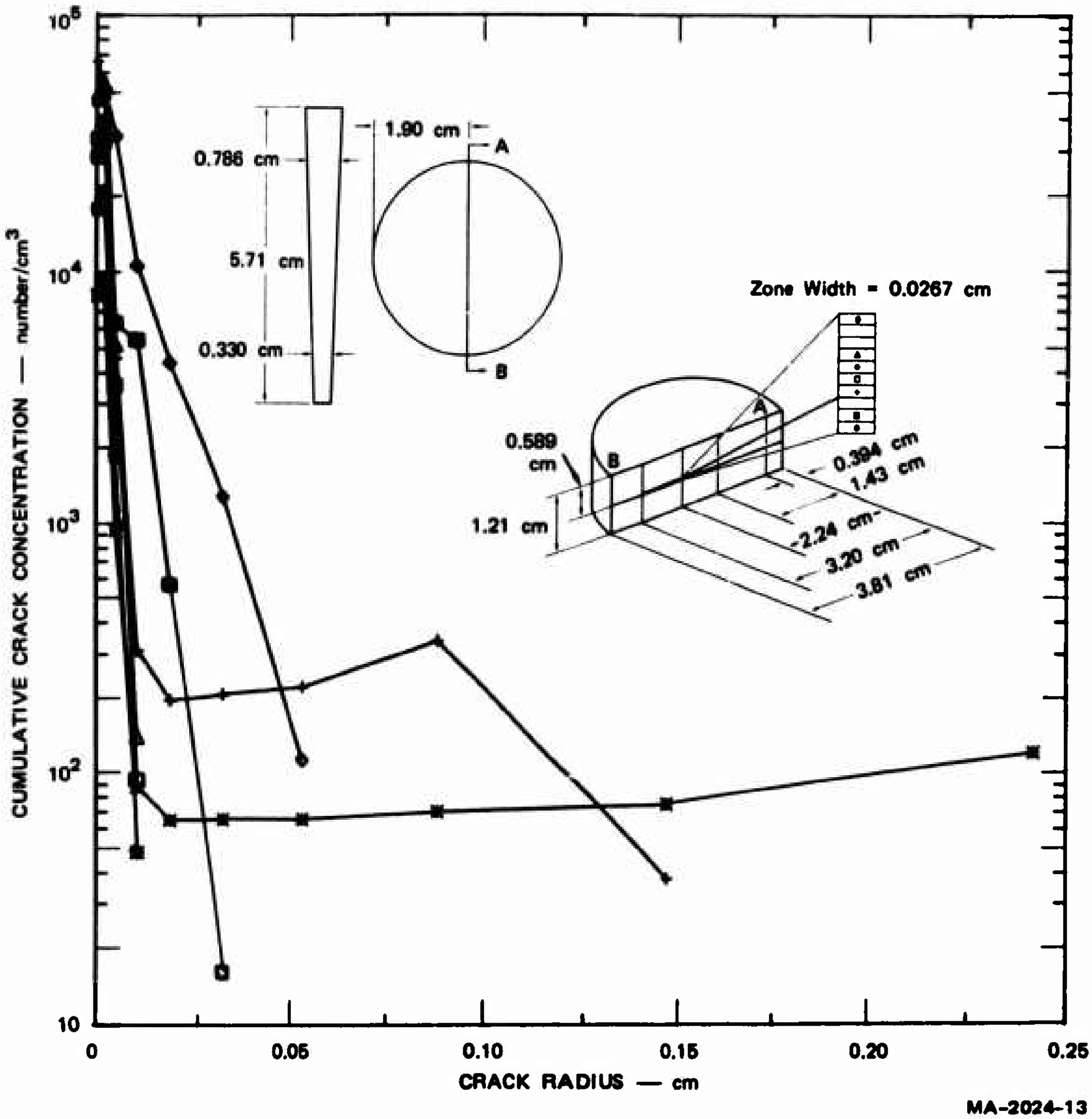

FIGURE 11 CRACK SIZE DISTRIBUTIONS ON SECTION A-B, FILE 3 OF SPECIMEN 2024-4

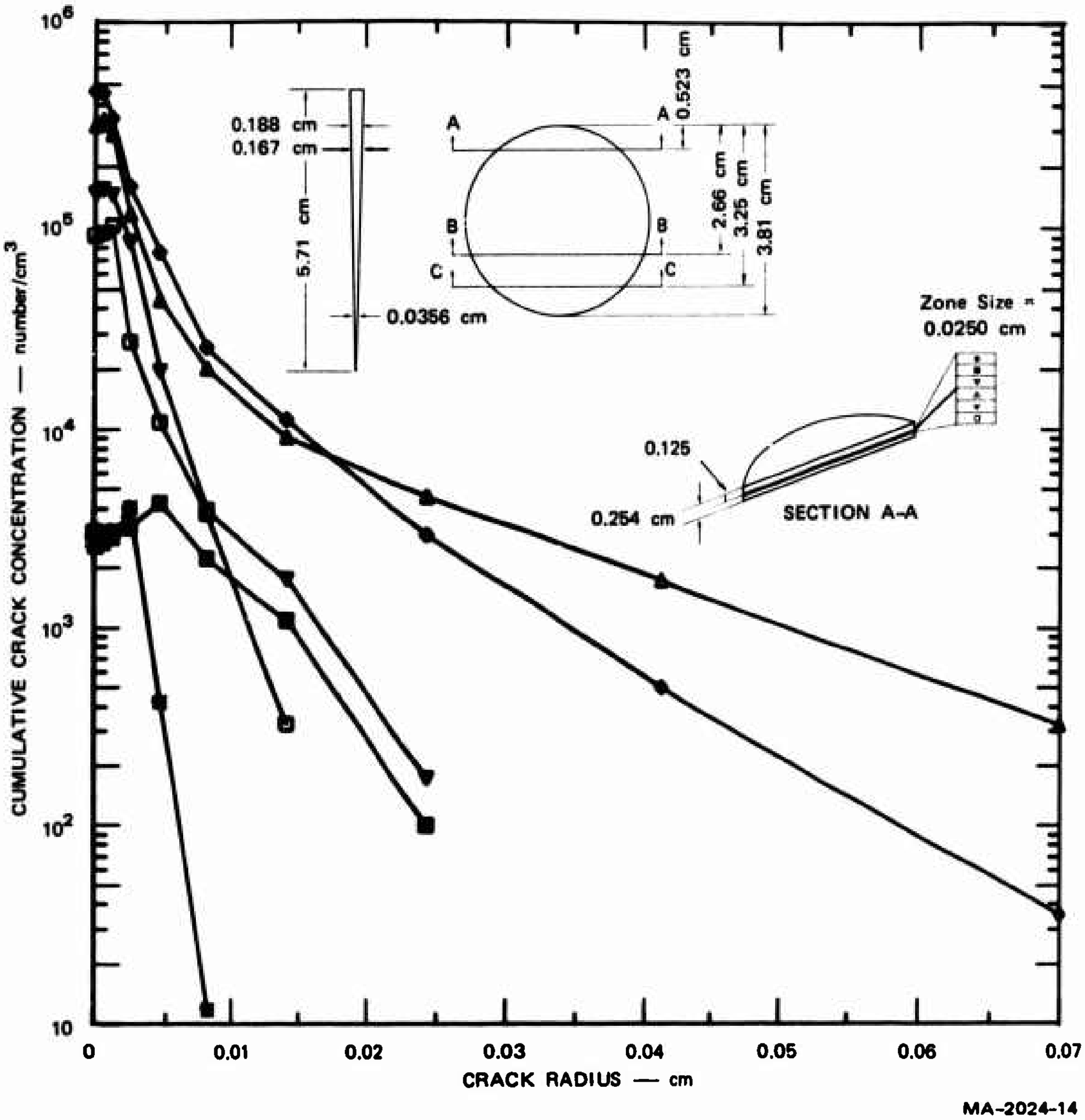

FIGURE 12 CRACK SIZE DISTRIBUTIONS ON SECTION A-A OF SPECIMEN 2024-5

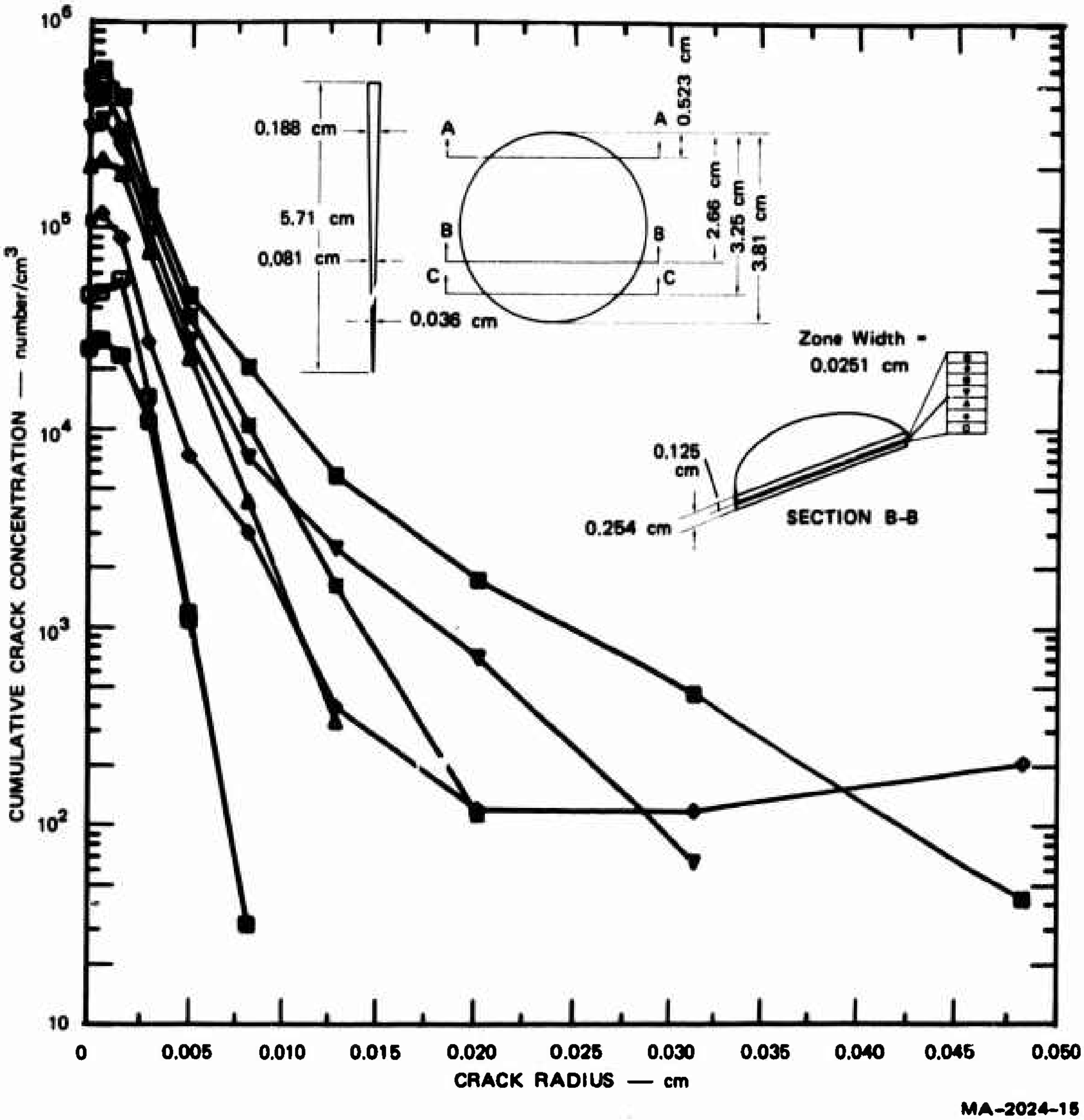

FIGURE 13 CRACK SIZE DISTRIBUTIONS ON SECTION B-B OF SPECIMEN 2024-5

C. Rod Impact Experiments

For the rod impact experiments, square specimens 10 or 15 cm on a side were cut from the half-inch armor steel. and the front and back surfaces were ground smooth and parallel. The projectiles were cylinders 1.03 cm in diameter by 2.03 cm long made of drill rod heat treated to various hardness levels and fitted into 1.16-cm-diameter Lexan polycarbonate sabots.

The experiments were conducted with a remotely fired, propellant-activated gun, Figure 14. The gun consists of a 1917 Enfield action fitted with a heavy barrel, which is chambered for the 1.16 Winchester magnum cartridge and smooth-bored to 1.16-cm diameter. Strain gages were mounted at three locations on the barrel--over the chamber, at 30 cm, and at 38 cm from the breech--and were routinely monitored during every experiment. The pressure-versus-time data were used in designing powder charges for desired projectile velocities and in ensuring that safe pressures were not exceeded in the gun.

Projectile velocity was determined either from a calibration curve relating velocity-at-impact to powder charge or by measuring the times between successive cutoffs of three light beams by the projectile as it emerged from the muzzle. Fiber optics, mounted in an aluminum muzzle extension, were used for transmission and pickup of the light beams. The muzzle extension also served as a projectile guide, ensuring normal impact of the projectile on the target. Since over half of the projectile length is still in the muzzle extension at the moment of impact, the muzzle extension is slotted to relieve the gas pressure.

Details of the five rod impact experiments are given in Table IV, and views of polished cross sections of the specimens through the point of impact are shown in Figure 15. No fracture damage and very little deformation occurred at 0.64 mm/μsec. At higher velocities a large

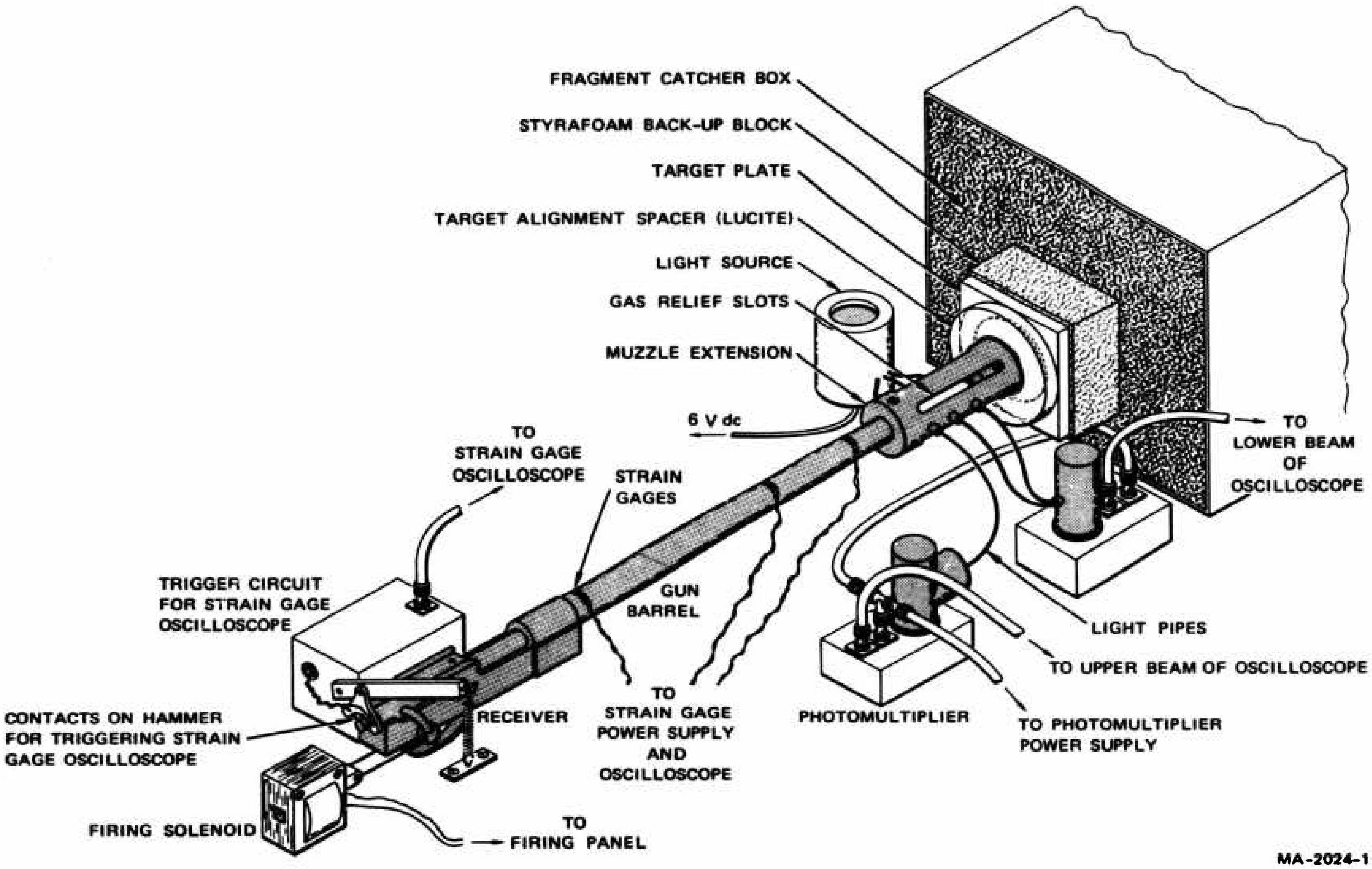

FIGURE 14 EXPERIMENTAL FACILITY FOR LONG-ROD-IMPACT TESTS

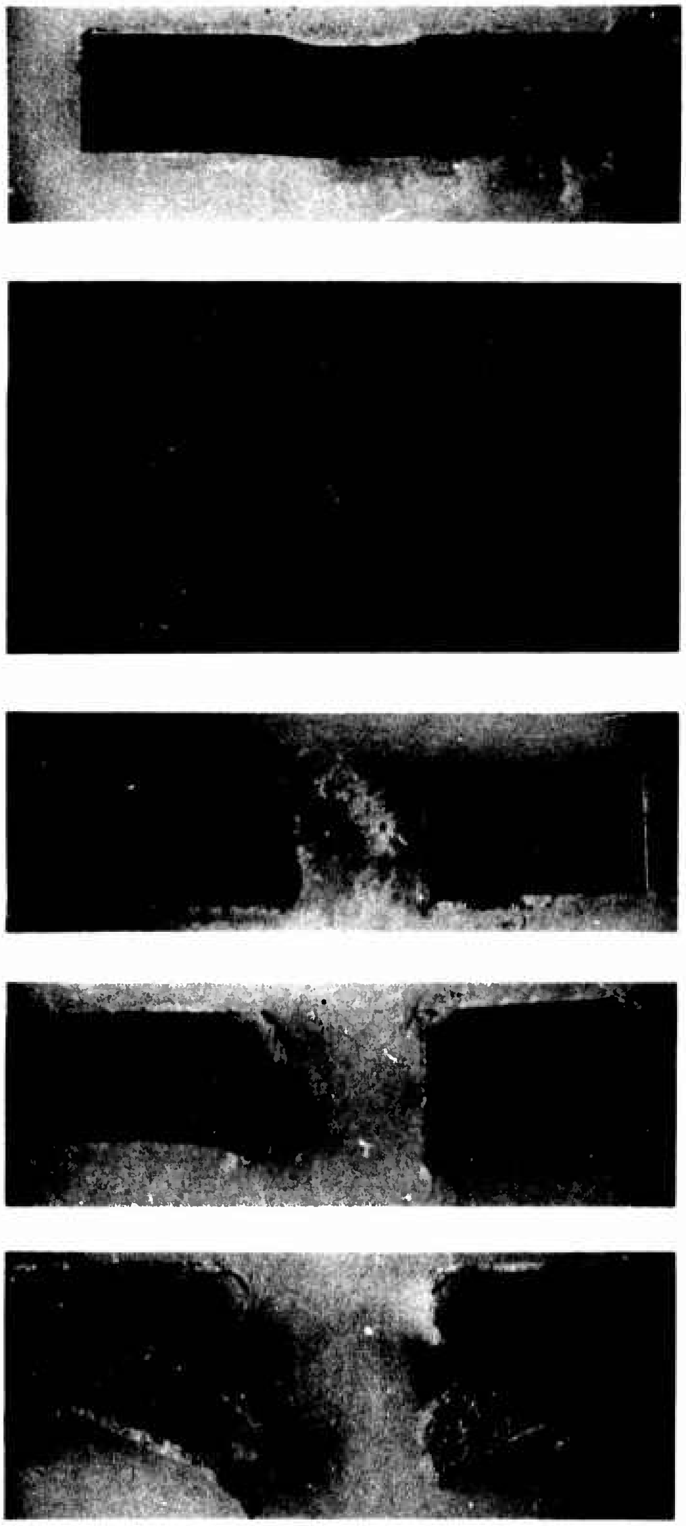

(a) SPECIMEN 34, 0.64 mm/μsec

(b) SPECIMEN 35, 0.67 mm/μsec

(c) SPECIMEN 33, 0.72 mm/μsec

(d) SPECIMEN 32, 0.85 mm/μsec

(e) SPECIMEN 31, 1.0 mm/μsec

MP-2024-25

FIGURE 15 POLISHED AND ETCHED SECTIONS THROUGH 8.66-mm-THICK XAR30 ROLLED HOMOGENEOUS STEEL PLATES SHOWING THE EFFECT OF THE VELOCITY OF THE IMPACTING ROD ON THE DAMAGE PATTERN

Table IV

ROD IMPACT EXPERIMENTS ON XAR30 ARMOR STEEL

Experiment Number	Specimen Thickness (mm)	Projectile Velocity (mm/μsec)	Remarks
31	8.66	1.0	Penetration; gross back surface scab.
32	8.66	0.85	Penetration; large mid-plane crack.
33	8.66	0.72	Penetration.
34	8.66	0.64*	No penetration.
35	8.66	0.67*	Penetration.

* Optically measured.

(a) FULLY SCABBED BACK SURFACE

(b) BACK SURFACE SCAB

(c) PLUG

MP-2024-26

FIGURE 16 APPEARANCE OF XAR30 TARGET IN LONG ROD EXPERIMENT 31 AFTER IMPACT AT 1.0 mm/μsec central crack formed, Figure 15(c) and (d), which at 1.0 mm/μsec caused a large scab of the armor steel to break free, Figure 15(e) and Figure 16. Figure 16 shows the appearance of the scabbed back surface, the scab, and the plug from Experiment 31.

Penetration in these experiments is classified as occurring in a plugging mode. Close examination of the surfaces shown in Figure 15 shows the existence of narrow bands that appear white when etched in nital or Vilella's reagent (Figure 17). These bands are known as adiabatic shear bands* and act as preferred cracking paths. Thus the penetration process in XAR30 armor steel includes the formation of highly localized regions of intense shear, which fail and result in the liberation of the plug-like segment of material from the armor plate.

The plugs from these experiments were also sectioned, polished, etched, and examined with a microscope. A small meniscus-shaped region of different etching response, Figure 18, was observed directly beneath the impact surfaces of Specimen 31, indicating that the $\alpha_{bcc} \rightleftarrows \epsilon_{hcp}$ polymorphic phase transformation had taken place. This zone was not observed in the other specimens. It was recently shown[15] that the lower boundary of this meniscus corresponds to an isobar of about 130 kbar.[15] It was also found that the occurrence of this phase change significantly alters the stress history and hence the fracture damage in the target material.[15]

Specimen 31 also exhibited several cracks parallel to the impact surface at about mid-thickness, Figure 18. Only one such crack was

---

* Adiabatic shear bands are narrow regions of highly localized large plastic shear strains. The heating accompanying the shear deformation may increase the temperature high enough to cause solid phase transformations or even melting. Very rapid quenching of this material follows because the large volume of adjacent material in intimate contact with the narrow band conducts the heat away at high rates. In the present instance a transformation to austenite followed by another rapid transformation to martensite probably occurred. The white etching response in 5% nital is consistent with the existence of martensite.

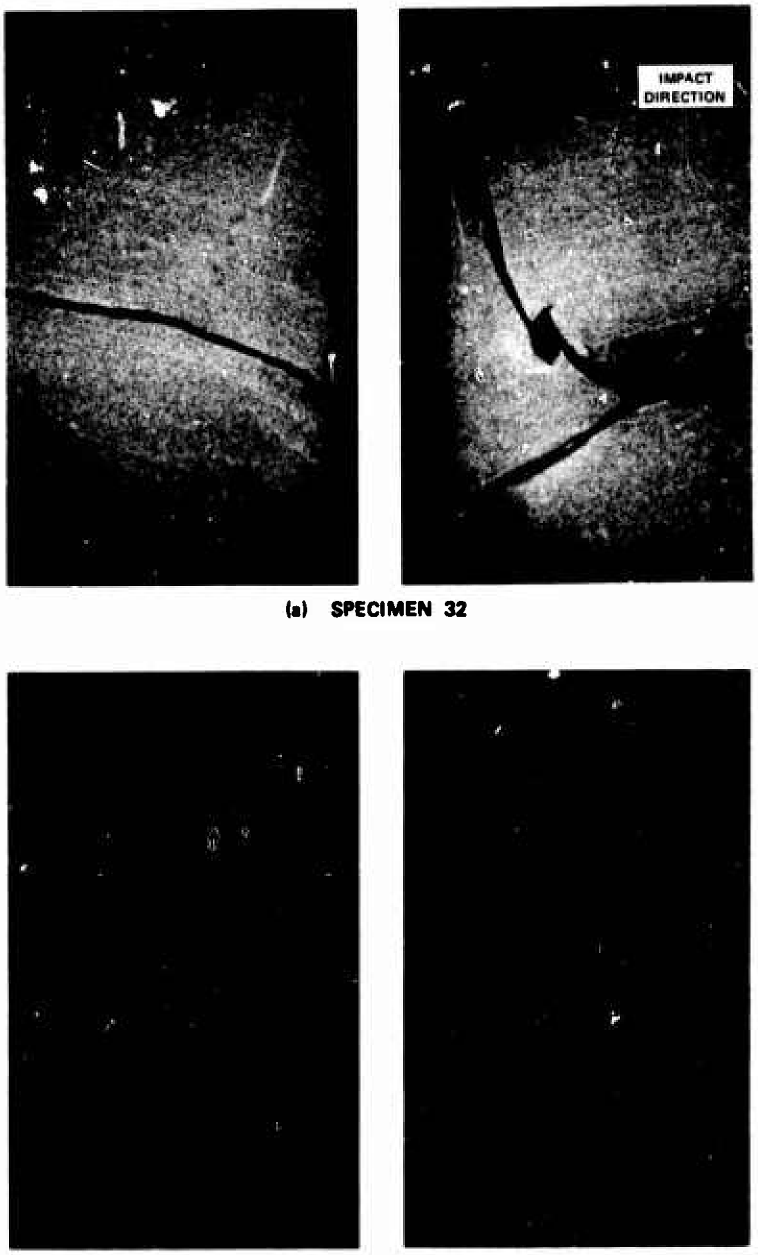

(a) SPECIMEN 32

(b) SPECIMEN 35

MP-2024-27

FIGURE 17 ENLARGED VIEWS OF SECTIONS THROUGH SPECIMENS 35 AND 32 NEAR THE ZONE OF PENETRATION SHOWING THE ADIABATIC SHEAR BANDS

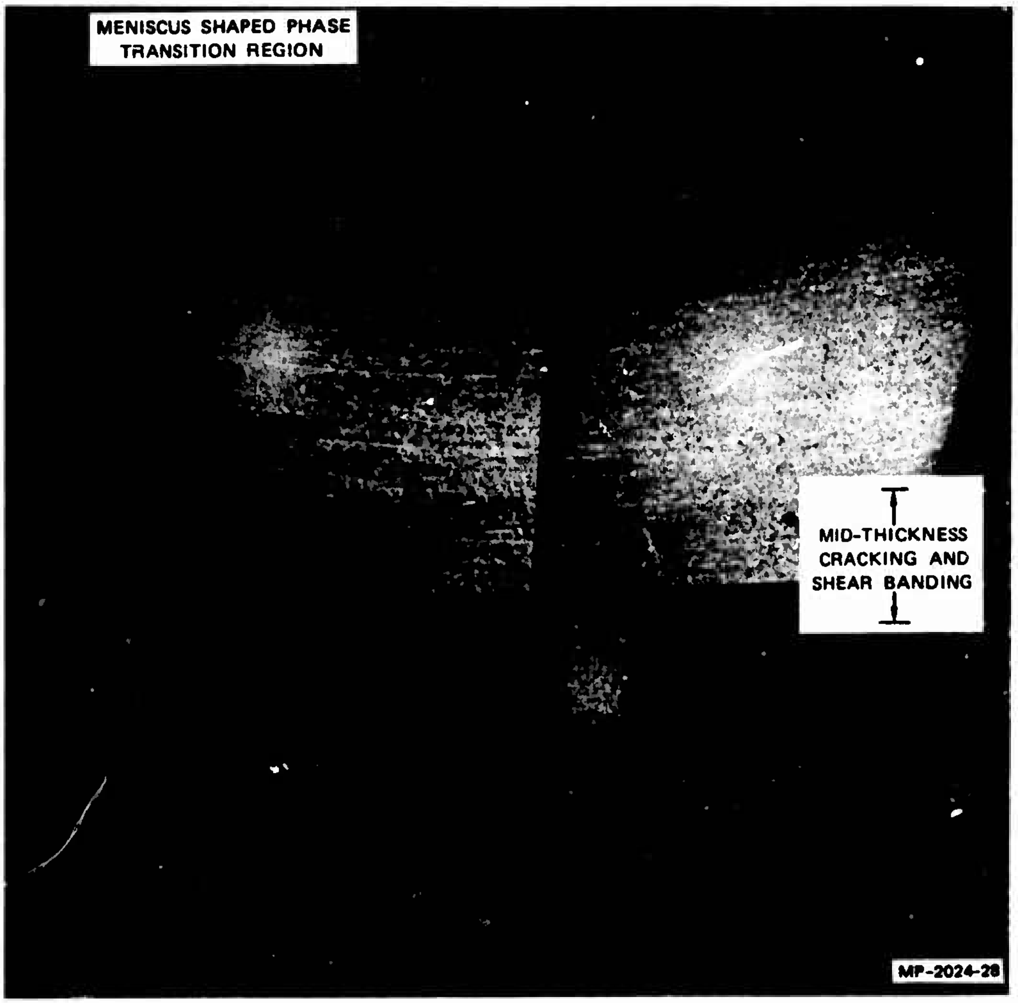

FIGURE 18 ENLARGED CROSS SECTION OF THE PLUG FROM THE XAR30 TARGET IMPACTED IN LONG ROD EXPERIMENT 33

observed in Specimen 32; none was observed in the other specimens. Adiabatic shear bands bordered the edges of all plugs. A single shear band running inward from the sides at mid-thickness was observed in Specimens 31 and 32.

IV APPLICATIONS OF THE DUCTILE AND BRITTLE FRACTURE MODELS

The two-dimensional ductile and brittle fracture models were applied to the simulation of damage in several metals. The brittle fracture parameters for XAR30, an armor steel, were derived from impact experiments, as described in the previous section. Then model calculations were performed to simulate two-dimensional damage in a target of the material. To further demonstrate the models, simulation calculations were made for tapered-flyer impacts in 1145 aluminum (ductile fracture) and in Armco iron (brittle fracture).

The first step in applying a fracture model to a material is to determine the fracture parameters governing nucleation and growth of damage. The fracture parameters for XAR30 armor steel were computed from the observed damage in three tapered-flyer experiments. The following procedure, which was used to calculate the parameters, was similar to that developed for beryllium.[4] The average crack nucleation rate (total number of cracks divided by nominal duration of the tensile stress) was plotted versus peak stress in tension to find the nucleation threshold stress (σ_{no}) and the other nucleation parameters (σ_1 and $\dot{N}_o$). The shape parameter R_1^c of the observed distribution was plotted versus tensile impulse (peak tension times duration of the tension) to determine the nucleation size (R_o^c) and the growth rate constant (T_1). After the initial estimates of all five parameters were determined from plots, trial one-dimensional calculations were performed to approximate the impact conditions at several points in the target. These calculations were repeated with different fracture parameters until the computed and measured damage compared satisfactorily. Then a two-dimensional calculation was performed to simulate the entire impact. It was not necessary to modify the parameters further and repeat the two-dimensional simulation. The fracture parameters found for XAR30 armor are listed in Table V. The parameters for Armco iron and aluminum, obtained on earlier projects,[2-4] are also included in the table.

Some of the results of the simulations for three tapered-flyer impacts are shown in Figures 19 through 21. These figures show the crack-size distributions on the planes of maximum damage at each section. The crack size distributions are exponential in the computations and therefore appear as straight lines in these figures. The computed distributions are high in some case and low in others but the agreement is considered satisfactory.

Two fracture calculations were performed with the ductile and brittle fracture models to examine their capabilities. Each was the simulation of a tapered-flyer experiment in a well-characterized material: 1145 aluminum (ductile) and Armco iron (brittle). These tapered-flyer experiments were selected instead of projectile impacts because no large distortions of the Lagrangian mesh occur during a calculation. Thus it was possible to test the fracture models without the difficulties involved in rezoning and construction of slide lines that would be required for more complex geometries.

The configuration for the tapered flyer experiments was shown schematically in Figure 4, and dimensions for the sample cases are shown in Figure 22. For the aluminum impact calculations, the width of the flyer and target were foreshortened to 5.328 mm to minimize the number of computational cells required. In the computations the lateral boundaries were allowed no horizontal motion, thus approximately simulating the conditions in the central region of a tapered-flyer target.

The first wave traveling through the target after the impact was a compressive wave. This wave was reflected from the free rear surface of the target as a zero-stress rarefaction (waves 4 in Figure 23). This

Table V

DYNAMIC FRACTURE PARAMETERS FOR XAR30 ARMOR STEEL, ARMCO IRON, AND 1145 ALUMINUM

Code Designation	Name in Derivations	Units	XAR30	Armco	1145 Al
TSR(M,1)	T_1, growth coefficient	$cm^2/dyn/sec_2$	-5.5×10^{-5}	-0.0006	-0.01
	η, material viscosity	$dyn\text{-}sec/cm^2$	4545	417	75
TSR(M,2)	σ_{go} or P_{go}, growth threshold	dyn/cm^2	-1.0×10^8	-2.0×10^8	-4.0×10^9
TSR(M,3)	R_o, nucleation size parameter	cm	4.0×10^{-3}	5.0×10^{-5}	1.0×10^{-4}
TSR(M,4)	$\dot{N}_o$, threshold nucleation rate	$no./cm^3/sec$	4.0×10^8	4.6×10^{12}	3.0×10^9
TSR(M,5)	σ_{no} or P_{no}, nucleation threshold	dyn/cm^2	-2.5×10^{10}	-3.0×10^9	-3.0×10^9
TSR(M,6)	σ_1 or P_1, nucleation sensitivity	dyn/cm^3	-1.786×10^9	-4.56×10^9	-4.0×10^8

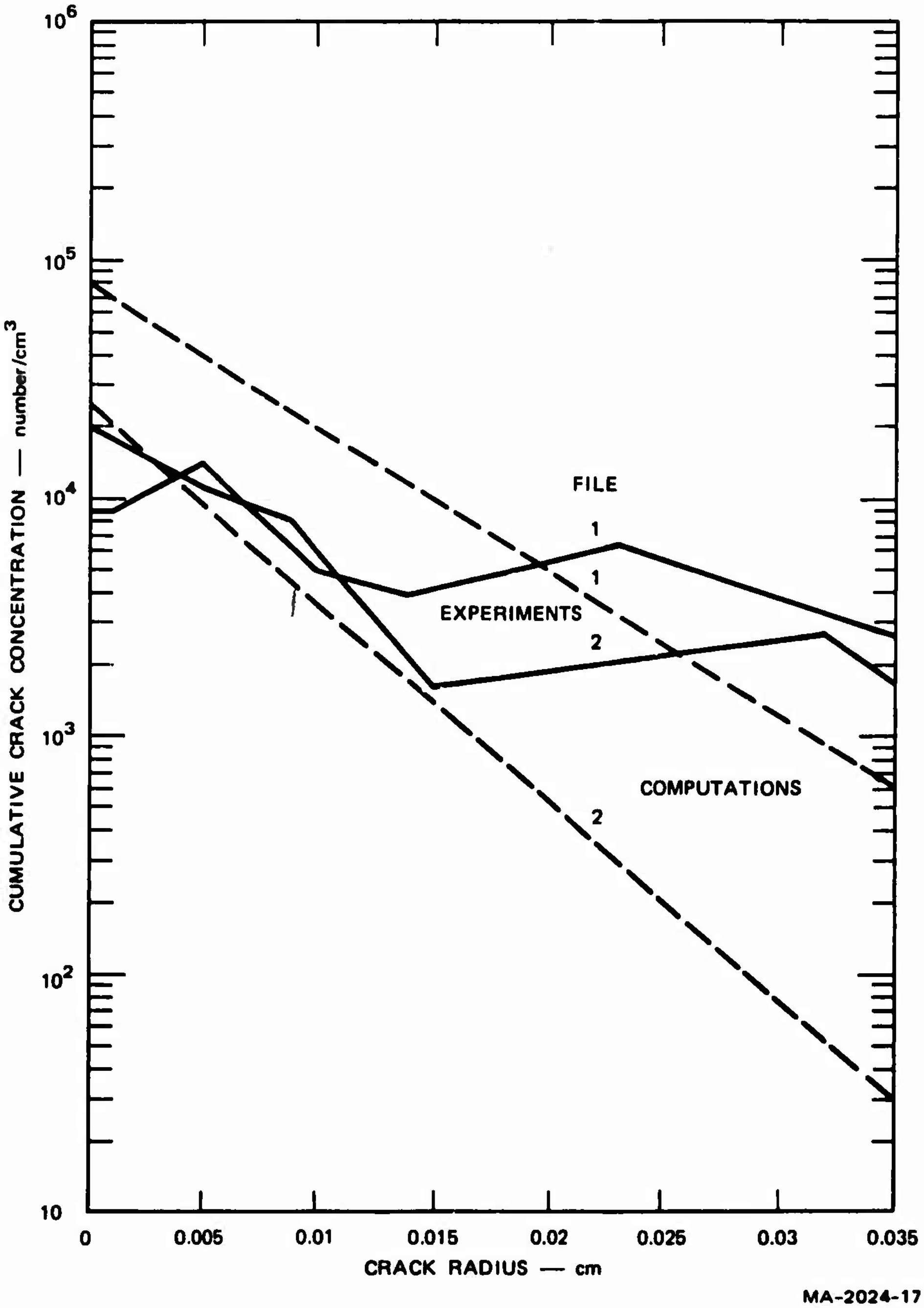

FIGURE 19 COMPARISON OF MEASURED AND COMPUTED DAMAGE ON THE PLANES OF MAXIMUM DAMAGE IN TAPERED-FLYER IMPACT EXPERIMENT 2024-3

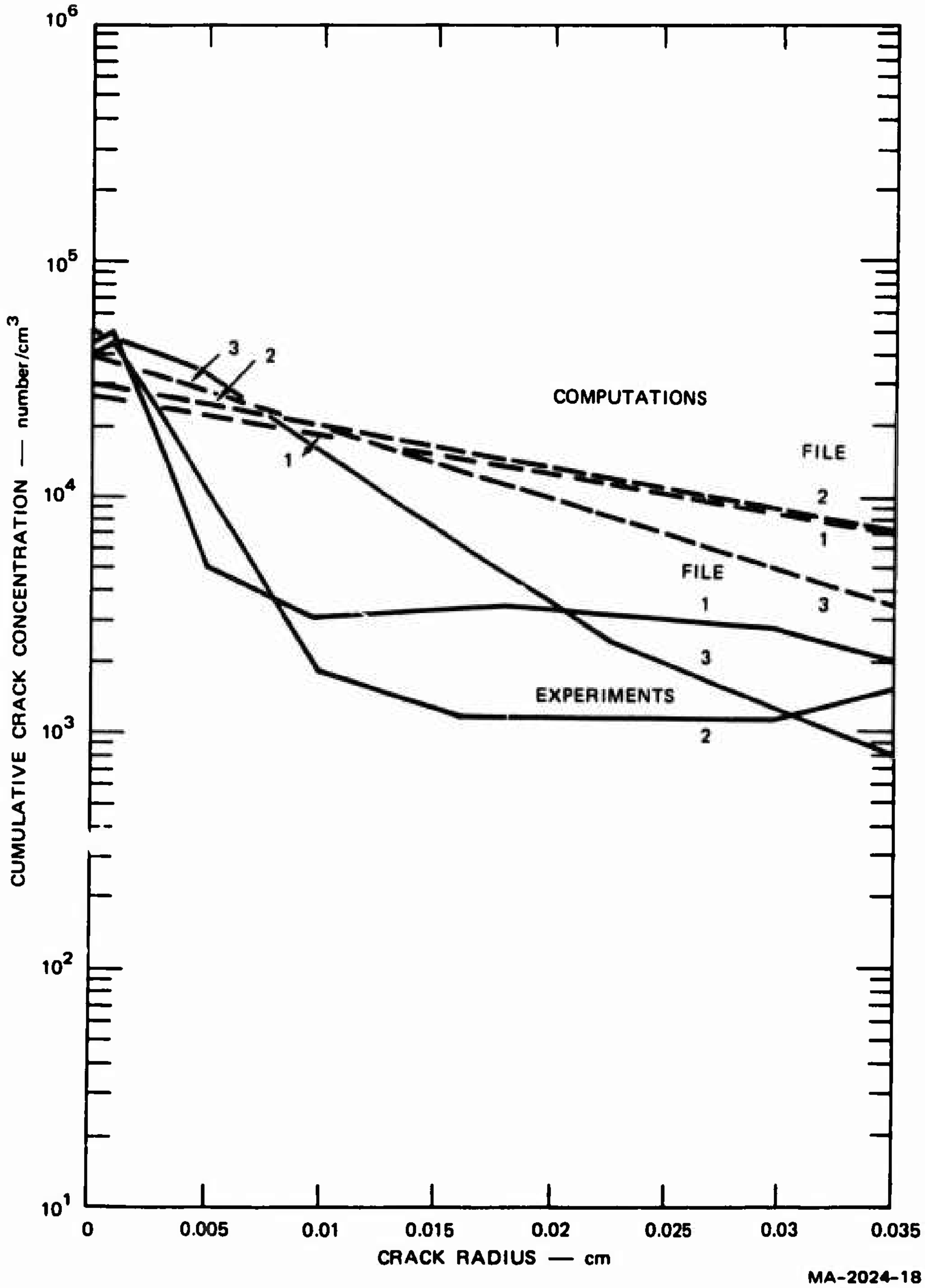

FIGURE 20 COMPARISON OF MEASURED AND COMPUTED DAMAGE ON THE PLANES OF MAXIMUM DAMAGE IN TAPERED-FLYER IMPACT EXPERIMENT 2024-4

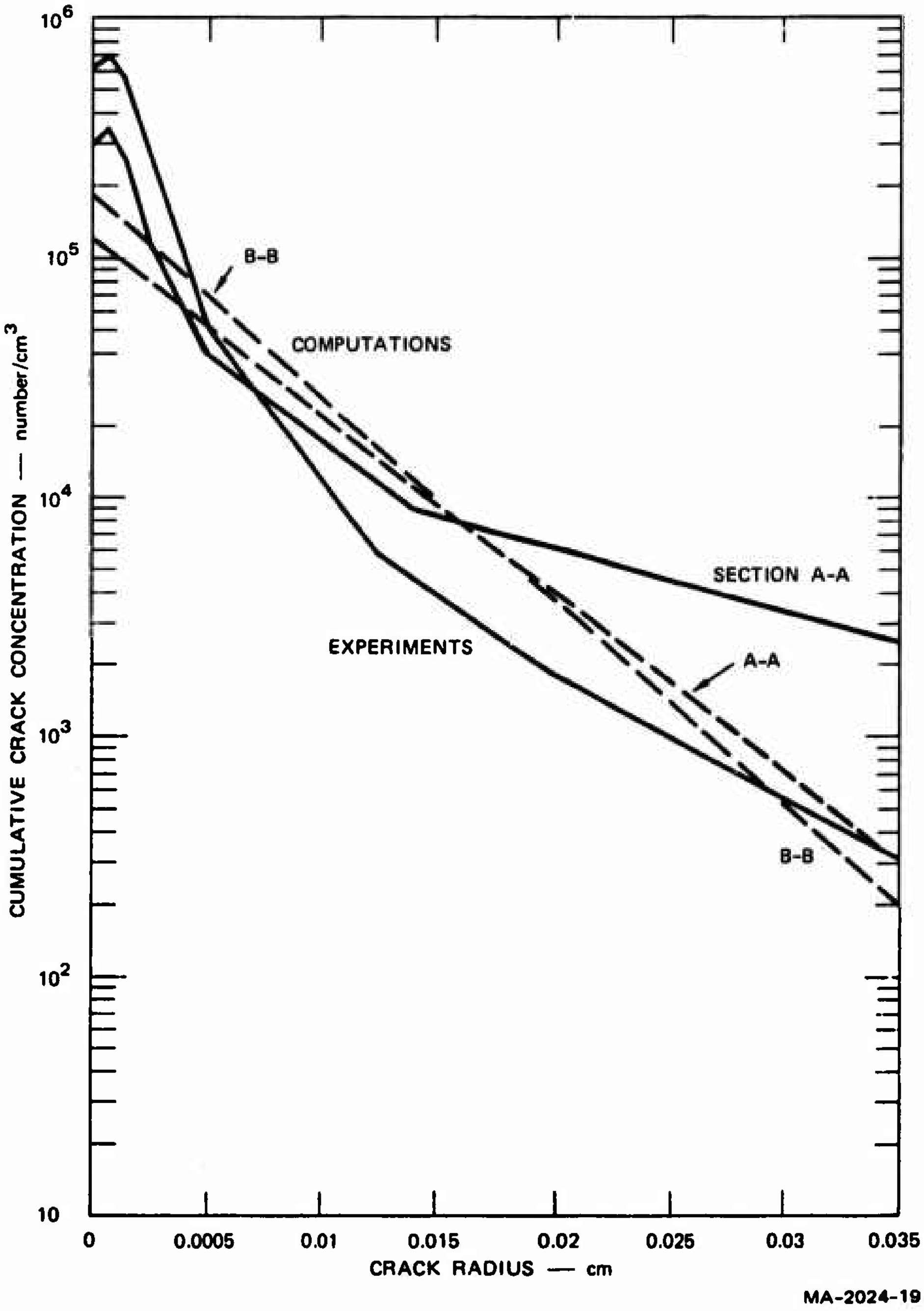

FIGURE 21 COMPARISON OF MEASURED AND COMPUTED DAMAGE ON THE PLANES OF MAXIMUM DAMAGE IN TAPERED-FLYER IMPACT EXPERIMENT 2024-5

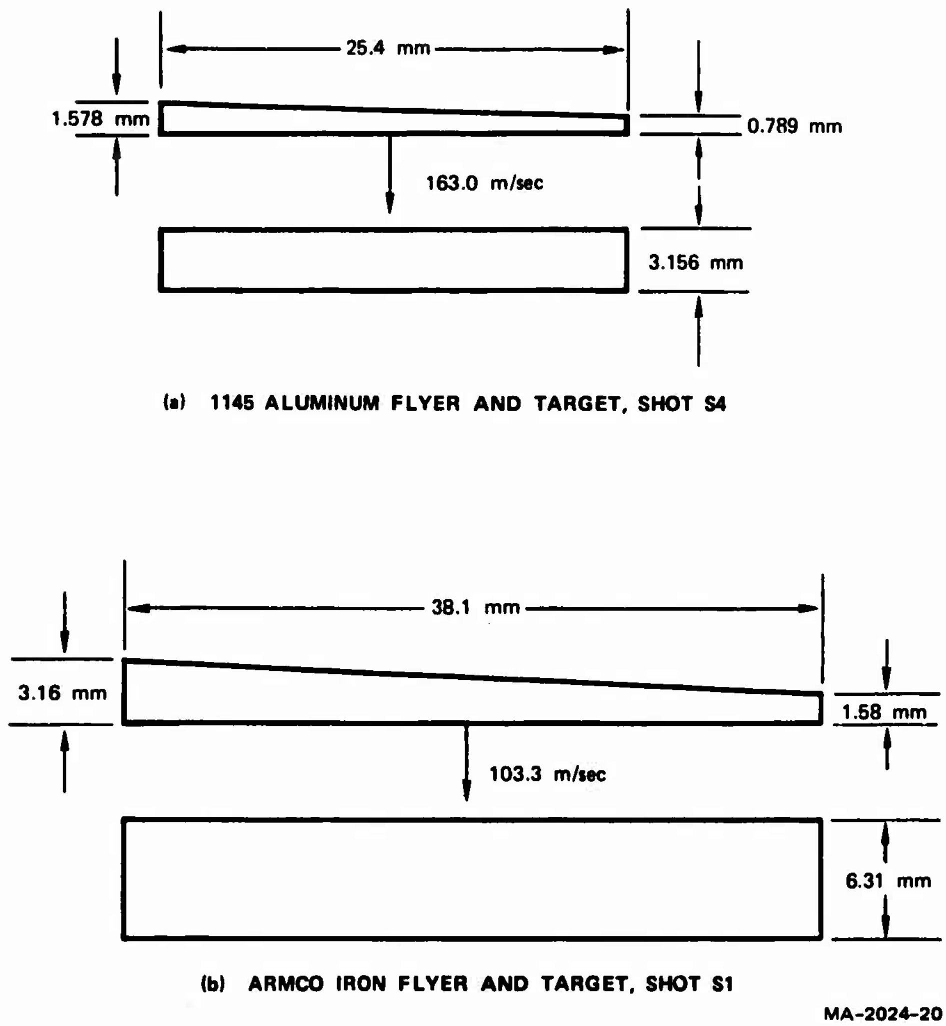

FIGURE 22 CONFIGURATIONS FOR TAPERED-FLYER IMPACT EXPERIMENTS

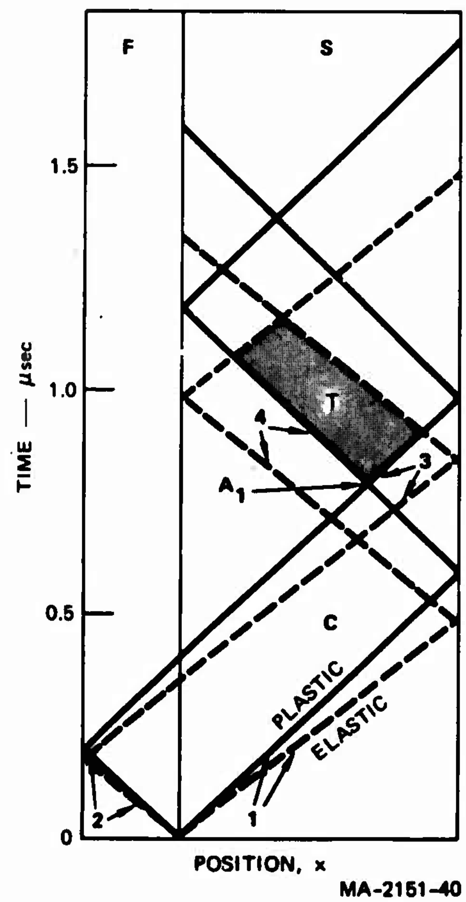

FIGURE 23 DISTANCE TIME PLOT SHOWING WAVE PATHS AND COMPRESSIVE (C) AND TENSILE (T) REGIONS IN A ONE-DIMENSIONAL IMPACT

rarefaction interacted with the rarefaction from the free surface of the flyer (waves 3) to produce tension in the target, as shown by the region labelled T in Figure 23. The vertical length of the tensile region is the duration of the tension at a point in the target. This duration is a linear function of the flyer thickness. Therefore in the tapered-flyer experiment, the peak tensile stress is constant, but the duration varies in the direction of the taper.

These simulations are given as sample problems in Appendix B. The computed results are depicted here as three-dimensional surfaces in which the damage functions are the amplitudes above the plane of the sections through the targets. The damage in the aluminum target is shown in Figures 24 and 25. Figure 24 shows that the line of maximum void volume is nearly at the middle of the target and that the amount of void volume increases toward the high damage end. The high damage end is the part of the target struck by the thicker portion of the flyer. Similar results are observed with the crack concentrations plotted in Figure 25. We note the damage functions present a fairly smooth surface, as is expected from a calculation if there are no stability problems.

The crack volume and crack concentrations computed for the Armco iron impact are shown in Figures 26 and 27. Note that both the amount of damage and the extent through the thickness increase towards the high damage end of the target.

Quantitative analyses of the experimental damage was not performed for these two tapered-flyer impact experiments. However, a qualitative comparison can be made between the damage observed and that computed. The aluminum impact calculation compares well with the observed amplitude of damage and the width of the damaged region. The Armco iron calculation indicates about the right level of damage, but the width of the damage region appears broader than that seen in the experiments.

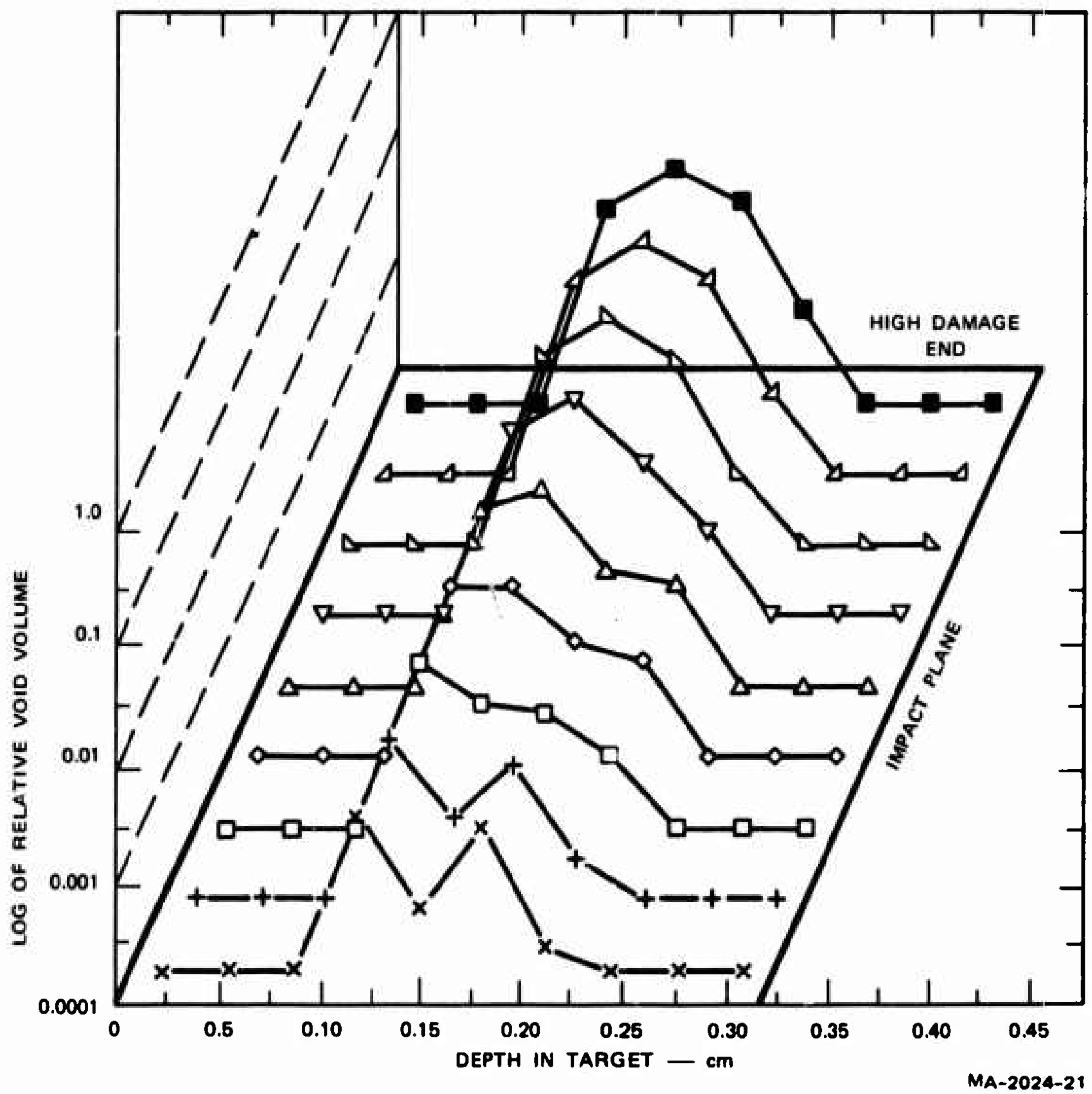

FIGURE 24 COMPUTED VOID VOLUME THROUGHOUT THE 1145 ALUMINUM TARGET AFTER TAPERED-FLYER IMPACT EXPERIMENT S4

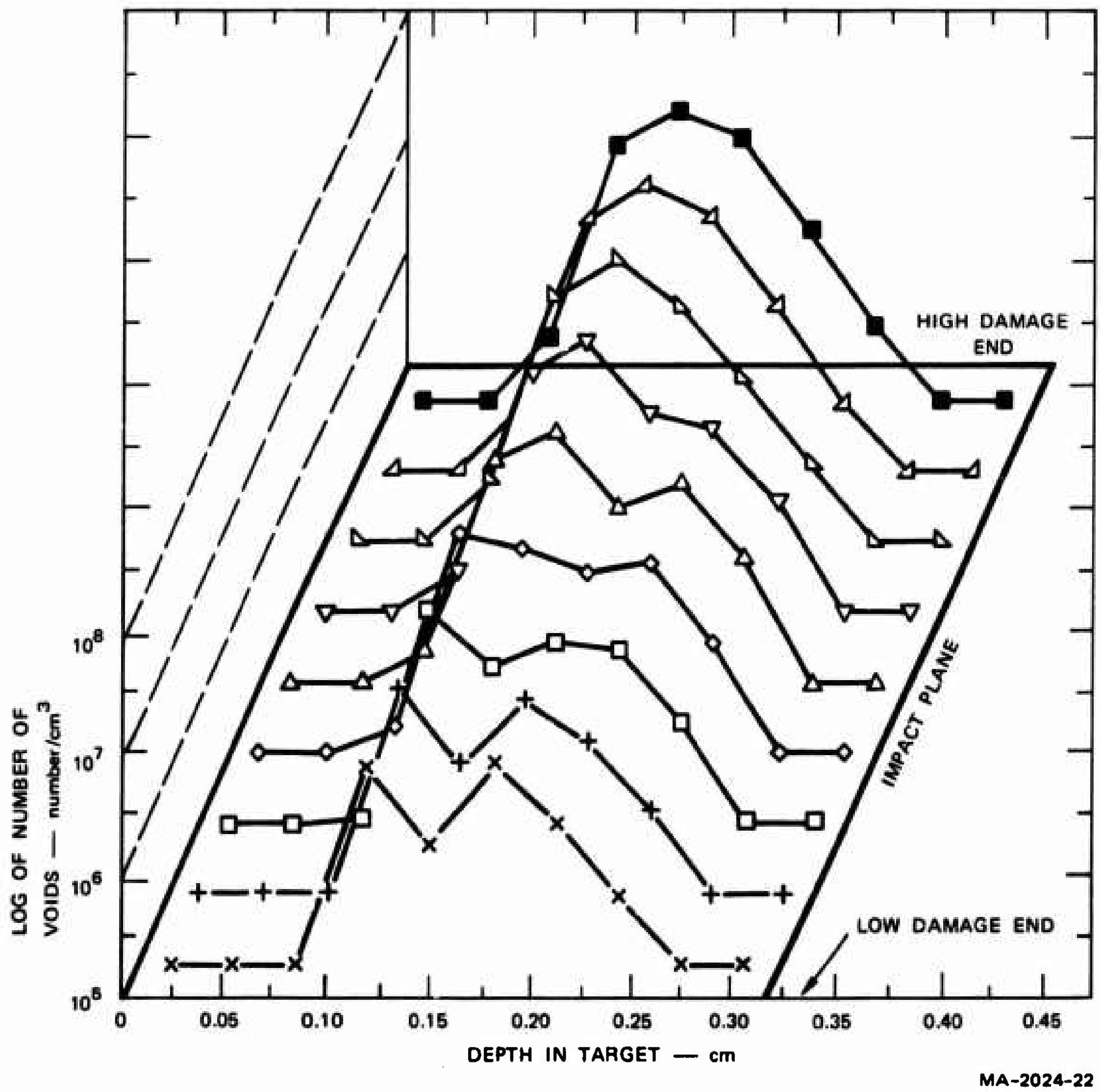

FIGURE 25 COMPUTED NUMBER OF VOIDS THROUGHOUT THE 1145 ALUMINUM TARGET AFTER TAPERED-FLYER IMPACT EXPERIMENT S4

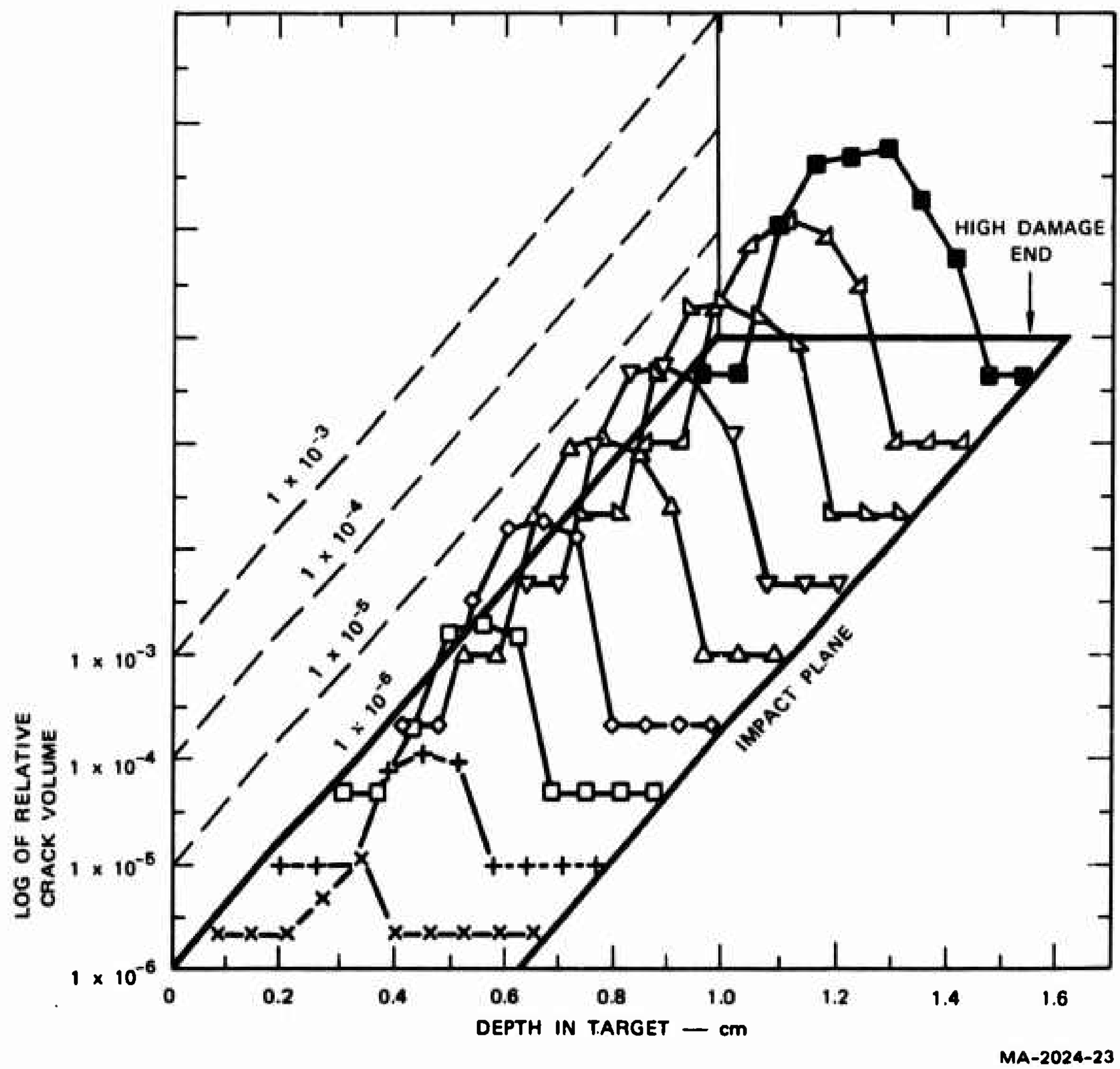

FIGURE 26 COMPUTED CRACK VOLUME THROUGHOUT THE ARMCO IRON TARGET IN TAPERED-FLYER EXPERIMENT S1 AT 2.069 μsec

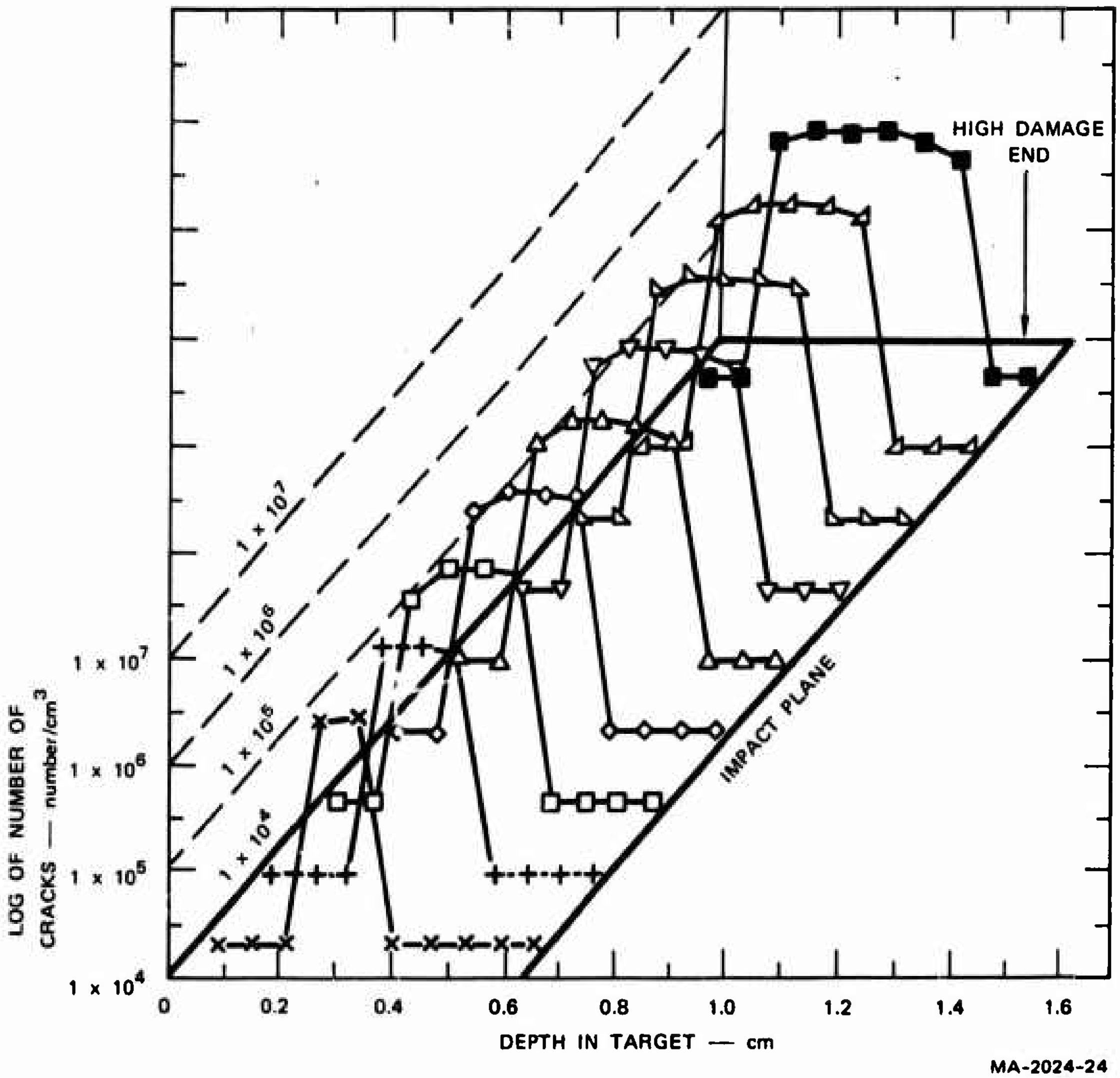

FIGURE 27 COMPUTED NUMBER OF CRACKS THROUGHOUT THE ARMCO IRON TARGET IN TAPERED-FLYER EXPERIMENT S1 AT 2.069 μsec

This lack of agreement suggests a need to allow nonelastic crack opening relations for the iron to permit damage to reduce the stress more rapidly. Such inelastic opening certainly occurs because the cracks remain open after the impact. However, appropriate opening relations have not yet been developed.

In summary, the brittle fracture parameters for XAR30 armor steel were derived from three tapered-flyer impact experiments. The ductile and brittle fracture models were then used to perform sample two-dimensional impact calculations to simulate damage in 1145 aluminum and Armco iron. The results of the computations in the three materials show that the models can simulate satisfactorily the ductile and brittle damage in two-dimensional problems.

Appendix A

DERIVATION OF EQUATIONS FOR FRACTURE SUBROUTINES

The detailed equations required to implement the ductile and brittle fracture models in wave propagation computer programs are derived in this appendix. These models are the bases of the subroutines DFRACT and BFRACT, which replace the usual equation-of-state subroutines when ductile or brittle fracture begins. Thus, during the early part of an impact calculation while the material is in compression, the usual equation-of-state subroutine is called to compute the stress for each cell at each time increment. Later, when the computed tensile stress exceeds the nucleation threshold, DFRACT or BFRACT is called. These routines compute the pressure and stress from given values of the strain increments, internal energy, and other parameters. In addition, these subroutines nucleate cracks or voids and permit existing cracks or voids to grow. Once a fracturing routine is called to compute stress for a computational cell, the usual equation-of-state subroutine is never called again for that cell. Thus the presence of damage is accounted for in subsequent recompressions or extensions by these fracture subroutines. In the model the recompression wave does not compact voids or reduce the number of voids or cracks; it simply compresses the solid material. Thus the model treats correctly only a low amplitude recompression wave. When a later tension occurs, the damage again begins to increase by nucleation and growth.

The stress and damage quantities are related by strongly nonlinear equations so that an iteration solution procedure is required. The development of this iteration procedure and of equations for the stress estimates used to start the iterations is described in this appendix.

Iteration Procedure

The subroutine is organized around an iteration procedure to determine simultaneously the damage quantities and the stresses. To minimize the number of iterations, a complex estimating procedure is derived for determining the starting value for each iteration. Methods for making the required estimates are outlined in the second subsequent section of this appendix.

The subroutines are provided with an internal energy E and strains $\Delta\epsilon$, as well as the values of E, ρ, pressure, and stresses at the previous time step, and are asked to provide pressure and deviator stresses at the current time. These new stress quantities are a function of the changes in energy and density, and also of the growing damage. Thus we require the simultaneous solution of the following system of equations:

$$\text{Damage} = f_1(P, \sigma'_{xx}, \sigma'_{yy}, \tau_{xy}, \sigma'_{\theta\theta})$$

$$\sigma = f_2(\text{Damage}, \Delta E, \Delta\rho) \qquad \text{(A1)}$$

where P = pressure

$\sigma'_{xx}, \sigma'_{yy}, \sigma'_{\theta\theta}$ = deviator stress

τ_{xy} = shear stress on the x-y plane

σ = any stress

The iteration process for solving the system of Eq. (A1) requires (1) an estimate, (2) a computation of all quantities including one with which the accuracy of the estimate can be tested, and (3) a test for convergence. The change in solid volume ΔV_s was chosen as the initial parameter for beginning an iteration because all the quantities can be computed from that one estimate. Convergence is based on ΔV, the overall volume change. The iteration process contains the following six steps, which provide the framework of the subroutine.

(1) Estimate ΔV_s.

(2) Compute the pressure and deviator stresses.

(3) Compute the crack or void volume, V_{va}, from the growth, nucleation, and expansion laws.

(4) Compute the total volume change ΔV_a from the change in crack or void volume ΔV_{va} and the change in solid volume ΔV_s.

(5) Compare ΔV and ΔV_a and terminate the iterations if the comparison is satisfactory.

(6) Reestimate ΔV_s and return to step (2).

The accuracy requirements for determining convergence were developed from trial computations with Armco iron and a program to test BFRACT. Several density step sizes and accuracy controls were used. It was found that the results can be made independent of step sizes to a precision on stress of 0.01 kbar:

(1) If step size in density is such that the maximum change in stress could be 0.33 σ_{no}, that is, one-third the nucleation threshold stress.

(2) If the ratio of $(\Delta V - \Delta V_a)/V_s$ is less than 2×10^{5}.

If the iterations do not converge in ten tries, an abort procedure is provided. Normally the convergence improves as the density step size decreases. Therefore, in the abort procedure, the step size is decreased and the calculations are repeated. If convergence is still not achieved, a message is printed and the calculations continue.

For compressive stresses there is no crack volume and void volume is held constant: then the initial estimate of ΔV_s is exact and no iteration is required. For small amounts of damage, the first estimate is usually accurate enough to provide convergence on the first iteration cycle. However, as the increase in crack or void volume becomes comparable to the imposed total volume changes, the number of iterations increases. Even at large damage, convergence usually occurs in three to five iterations.

Pressure Estimation

For beginning each iteration it is necessary either to estimate the specific volume directly or to estimate the pressure and derive the specific volume from the pressure. The initial estimate of pressure is made as accurately as possible to minimize the number of iterations required. Estimates are made on the assumption that the pressure is determined entirely by strain and changes in internal energy, by nucleation of new cracks or voids, or by a combination of strain, expansion, and growth of cracks or voids.

For strain and changes in internal energy only, Eq. 12 (See Section II of this report) is used, with ρ_s computed by assuming that all strain is taken in changing the solid specific volume, i.e., $\Delta V_s = \Delta V$. The estimate of pressure in the solid is

$$P_{se} = C\left(\frac{1}{\rho_o(V_{so} + \Delta V)} - 1\right) + \frac{\Gamma E}{V_{so} + \Delta V} \qquad \text{(A2)}$$

where V_{so} is the specific volume of the solid at the beginning of the time step.

If there are few cracks or voids in the cell, the initial pressure step beyond the nucleation threshold may be governed by nucleation. For cracks the pressure estimate based on nucleation is obtained by setting the imposed volume change ΔV equal to the nucleated volumes from Eq. (33) for all crack orientation bins. For the estimate, the stresses in each direction in Eq. (33) must be approximated in some way. Stress appears in the expression in two ways: directly, to describe the opening of the cracks (Eq. 29), and in the nucleation rate function $\dot{N}^i$ (Eq. 31). The stress appearing in the nucleation rate function is assumed to be of maximum importance, so it is treated more exactly than the stress controlling crack opening. The latter stress, which appears directly in Eq. (33), is taken as P_{so}, the solid pressure at the previous step. The pressure is used here instead of the stress in any particular direction to get an average of the nucleation behavior in all directions. In the expression for $\dot{N}^i$ (Eq. 31), $\sigma_{\omega\psi}$ is treated as the average pressure over the time interval, that is, $(P_{sn} + P_{so})/2$, where P_{sn} is the nucleation-based estimate. The pressure estimate from Eq. (33) is then

$$P_{sn} = - P_{so} + 2\sigma_{no} + 2\sigma_1 \ln \frac{\Delta V}{V_c \dot{N}_o R^3 \Delta t P_{so}} \quad \text{(crack nucleation)} \tag{A3}$$

where $V_c = \dfrac{32(1 - \nu^2)}{E} = 8 \left(\dfrac{1}{G} + \dfrac{1}{C+G/3}\right)$

C = bulk modulus

G = shear modulus

σ_{no} = nucleation threshold

$\dot{N}_o$ = nucleation rate parameter

E = Young's modulus

ν = Poisson's ratio

R_o = nucleation size parameter

Δt = time step

For void nucleation, the pressure estimate is derived from Eqs. (3) and (4), of Section II, with P taken as the average pressure, $(P_{sn} + P_{so})/2$. Then

$$P_{sn} = - P_{so} + 2P_{no} + 2P_1 \ell n \frac{\Delta V}{8\pi N_o R_o^3 \Delta t} \quad \text{(void nucleation)} \tag{A4}$$

Usually P_{sn} is an overestimate of the correct pressure.

A third estimate of solid pressure is made by considering that the imposed change in volume is taken by a combination of expansion and growth of existing cracks plus a strain in the solid material for the brittle case. Equation (37) is used to determine the volume change associated with expansion and growth of cracks. In this expression $\sigma_{\varphi\psi}$ in the expansion portion was replaced by $P_{sg} + \sigma'/2$, and $\sigma_{\varphi\psi}$ in the exponential was replaced by $(P_{sg} + P_{so})/2 + \sigma'$ where σ' is the most tensile deviator stress. These replacements for $\sigma_{\varphi\psi}$ were chosen on the basis of trial calculations in Armco iron. The total volume change from expansion and growth is then

$$V_v = - T_7[\sum_i N_o^i (R_1^i)^3] \; (P_{sg} + \frac{\sigma'}{2}) \exp [3T_1(\frac{P_{sg}}{2} + \frac{P_{so}}{2} + \sigma' - \sigma_{go}) \Delta t] \tag{A5}$$

or approximately

$$V_v = V_o \exp [3T_1(P_{so} + \sigma' - \sigma_{go}) \Delta t] [1 + \Delta P_{sg}(\frac{1}{P_{so} + \frac{\sigma'}{2}} + \frac{3}{2}T_1 \Delta t)] \tag{A6}$$

where V_{vo} = the void volume at the previous time step and

$$\Delta P_{sg} = P_{sg} - P_{so}$$

The total volume change is now taken as equal to the combination of growth and expansion from Eq. (A6), and the change in solid volume from

Eq. 17 of this report. This volume condition is

$$\Delta V = V_v - V_{vo} + V_s - V_{so} \tag{A7}$$

The resulting estimate for pressure is

$$\Delta P_{sg} = \frac{\Delta V - V_{vo}(X - 1) - \dfrac{V_{so}\Gamma(E - E_o)/C}{\dfrac{1}{\rho_o} + \dfrac{\Gamma E}{C}}}{V_{vo}X\left(\dfrac{1}{P_{so} + \sigma'} + \dfrac{3T_1\Delta t}{2}\right) - \dfrac{V_{so}^2}{C/\rho_o + \Gamma E}} \quad \text{(crack growth)} \tag{A8}$$

where $X = \exp\left[3T_1(P_{so} + \sigma' - \sigma_{go})\Delta t\right]$.

For ductile behavior the third pressure estimate is made based on a combination of strain in the solid material and void growth. The void volume is

$$V_v = V_{vo} \exp\left[T_1\left(\frac{P_{sg} + P_{so}}{2} - P_{go}\right)\Delta t\right]$$

$$\cong V_{vo} \exp\left[T_1\Delta t(P_{so} - P_{go})\right]\left[1 + \frac{T_1\Delta t\Delta P_{sg}}{2}\right] \tag{A9}$$

Combining Eq. 17, Eq. (A9), and the volume condition in Eq. (A7) provides the desired estimate of P_{sg}

$$\Delta P_{sg} = \frac{\Delta V - V_{vo}(X - 1) - \dfrac{V_{so}(E-E_o)}{C/\rho_o + \Gamma E}}{V_{vo} X \dfrac{T_1 \Delta t}{2} - \dfrac{V_{so}^2}{C/\rho_o + \Gamma E}} \quad \text{(void growth)} \qquad \text{(A10)}$$

where $X = \exp\ [T_1 \Delta t(P_{so} - P_{go})]$.

The pressure estimate for the first iteration is selected by taking the least tensile value from Eqs. (A2), (A3), and (A8) for the brittle case or from Eqs. (A2), (A4), and (A10) for the ductile case.

After the first computation of V_s and V_v based on the initial pressure estimate, a reestimate is often required. To minimize the opportunity for getting into loops, two procedures were constructed for the later estimates. The first is based on the result of the previous iteration and on the physical processes: the form is similar to Eq. (A8) or Eq. (A10). The second procedure is the _regula falsi_, an interpolation based on two previous trials.

The first procedure is based on a combination of growth, crack expansion, and change in solid volume. After expanding the exponential in the growth function in the same manner as in Eqs. (A6) or (A9), the crack or void volume for a small change in pressure $\Delta P_s = P_s - P_a$ is found to be related to the previously computed volume V_{va}, as follows:

$$V_v = V_{va}[1 + \Delta P_s (\frac{1}{P_a + \sigma'/2} + \frac{3}{2} T_1 \Delta t)] \qquad \text{(cracks)} \quad \text{(A11)}$$

or

$$V_v = V_{va} \left[1 + \Delta P_s \frac{T_1 \Delta t}{2}\right] \qquad \text{(voids)} \quad \text{(A12)}$$

where P_a is the pressure computed in the previous iteration. The change in solid volume is related approximately to the change in pressure as follows

$$V_s - V_{sa} = -\left(\frac{1}{\rho_o} + \frac{\Gamma E}{C}\right) \frac{\Gamma P_s}{C + P_a} \qquad \text{(A13)}$$

The total volume change computed in the preceding iteration was

$$\Delta V_a = V_{va} - V_{vo} + V_{sa} - V_{so} \qquad \text{(A14)}$$

where the subscript "a" refers to the previous iterations, and "o" refers to conditions from the last time step. Equation (A14) is subtracted from Eq. (A7) to obtain the change in ΔV required to produce a correct result.

$$\Delta V - \Delta V_a = V_v - V_{va} + V_s - V_{sa} \qquad \text{(A15)}$$

When Eqs. (A11) or (A12) and (A13) are inserted in Eq. (A15) and solved for ΔP_s, we obtain

$$\Delta P_s = \frac{\Delta V - \Delta V_a}{V_{va}\left(\dfrac{1}{P_a + \sigma'/2} + \dfrac{3}{2} T_1 \Delta t\right) - \left(\dfrac{1}{\rho_o} + \dfrac{\Gamma E}{C}\right)\dfrac{1}{C + Pa}} \qquad \text{(cracks)}$$

(A16)

or

$$\Delta P_s = \frac{\Delta V - \Delta V_a}{V_{va}\frac{T_1 \Delta t}{2} - \left(\frac{1}{\rho_o} + \frac{\Gamma E}{C}\right)\frac{1}{C + P_a}} \quad \text{(voids)} \tag{A17}$$

The second reestimate procedure requires information from two previous iterations: the estimated changes in solid volume, ΔV_{sa} and ΔV_{sb}, and the computed total volume change, ΔV_a and ΔV_b. The subscript b refers to values saved from some earlier iteration. The next estimate is then simply

$$\Delta V_s = \Delta V_{sa} + \frac{\Delta V_{sb} - \Delta V_{sa}}{\Delta V_b - \Delta V_a}(\Delta V - \Delta V_a) \tag{A18}$$

Appendix B

INSERTION OF BFRACT AND DFRACT INTO HEMP

During brittle fracture calculations, BFRACT and DFRACT replaces the usual routines for computing pressure and deviator stress. This section describes the changes required to incorporate BFRACT and DFRACT into HEMP or other two-dimensional Lagrangian wave propagation codes and gives test cases for verifying the code results.

Changes to HEMP

The insertion of BFRACT and DFRACT requires some added COMMON storage, additional reads for property data, a procedure for switching to the fracture routine, a CALL statement, and a means for printing the computed damage. These changes were all made to FIBROUS, a comparable two-dimensional program at SRI. The additional COMMON quantities are:

TSR (6,30)	An array containing the fractures and fragmentation parameters. It now provides for 6 materials and 30 parameters each, although only 9 parameters are now in use.
ENM (K,J)	Array for the fraction of crack or void volume.
ENT (K,J)	Array for the number of cracks or voids per unit volume in each cell.
LS	Initializing indicator. Set to zero at beginning of program, reset to 1 in BFRACT or DFRACT after initialization.
NFR (M)	An indicator array for the type of fracture considered. NFR = 1 for ductile, and NFR = 2 for brittle fracture.

The additional materials data are inserted in the initializing routine with the rest of the materials data. In FIBROUS, the indicator NFR is read with the material name. If NFR equals 2, then two data cards are read to obtain the first 9 variables of the TSR array. For NFR = 1, only one data card is needed.

BFRACT and DFRACT are not called or initialized until the tensile stress in some cell exceeds the threshold stress for nucleation, TSR (M,5). On the first CALL (described in detail below) the dimensional arrays in BFRACT are zeroed, and several coefficients that depend on material properties are computed. If a second material is involved in fracturing, these coefficients are computed on the first call to BFRACT for a cell of that material. DFRACT requires no initializing. As many as six materials may undergo fracture at once with the present array dimensions.

The CALLs to BFRACT and DFRACT are inserted in the subroutine that controls stress calculations (VQP in HEMP, SWEEPF in FIBROUS) just before the pressure is computed. The following statments may be used:

```
480  IF (NFR(M) - 1) 600, 480, 490
     IF (ENT(K,J).GT.O.) GO TO 500
     IF (P(K,J) .LT.TSR (M.5)) GO TO 500
     GO TO 600

490  IF (ENT(K,J) .GT.O.) GO  TO 520
     IF (AMIN 1 (TXX(K,J), TYY (K,J), TTT (K,J)) .LT. TSR (M,5))
     GO TO 520
     GO TO 600

500  CALL DFRACT (SXXN, SYYN, STTN, SXYN, EXXH, EYYH, ETTH, EXYH,
       P(K,J), ENM(K,J), ENT(K,J), VW, VN, DELTH, E(K,J), EEST,
       CA(M), EQSTG(M), MU(M), RHO(M), TSR, YY(M), YD(M), F, M,
       DROT)
     GO TO 540

520  CALL BFRACT (LS, SXXN, SYYN, STTN, SXYN, EXXH, EYYH, ETTH,
       EXYH, P(K,J), ENM(K,J), ENT(K,J), VW, VN, DELTH, E(K,J),
       EEST, CA(M), EQSTG(M), MU(M), TSR, YY(M), YD(M), F, K, J,
       M, ICYCLE, RHO(M), DROT)

540  SXXW = SXXN
     SYYW = SYYN
     STTW = STTN
     SXYW = SXYN

600  GO TO 650
     (usual relations for pressure and energy)
```

The parameters in the preceding statements are defined in the Nomenclature list given below. It should be noted that BFRACT and DFRACT compute both deviator stress and pressure. Both of these quantities are positive in compression.

The damage information for all cells undergoing brittle fracture is listed in a separate CALL to BFRACT. The form of the CALL is:

CALL BFRACT (2)

This statement may be inserted in the stress controlling subroutine or in a printing or editing subroutine. An example of the listing given is shown later. The damage information computed in DFRACT is all contained in the NM and NT arrays, which are parameters in the CALL statement and are available to the calling program. Therefore, for ductile fracture the damage listing is performed outside DFRACT.

To aid the user in testing the BFRACT and DFRACT subroutines, sample tapered-flyer impact calculations are given. The planar, two-dimensional geometry of the target and flyer is shown in Figure B-1. Sample results from various stages in the two calculations are shown in Figures B-2 through B-10. No motion is permitted in the third dimension, and no vertical motion is permitted along the upper and lower boundaries of either target or flyer. The left and right boundaries are free surfaces. The interface surfaces of target and flyer are in contact during the early part of the calculation but are allowed to separate gradually when the stresses in the adjacent cells become tensile. Specific information about the calculations is contained in the listing of the INPUT data decks, Figures B-2 and B-7. The nomenclature for the data decks is given in the Nomenclature list. The data in Figure B-2 do not correspond entirely with the set of parameters finally chosen as the best representation of XAR 30 steel.

The sample printouts from the flyer computations include the listing of the input data, Figures B-2 and B-7, a portion of edits printed in SWEEPF (Figures B-3 and B-8). At this time the target has passed through a tension and fracturing phase and is now undergoing recompression. Figures B-4 and B-9 list a summary of the damage quantities at each cell (printed in SWEEPF). The detailed listing of the damage quantities given in Figure B-5 is printed by BFRACT. The CL and CN quantities at each cell are given with the average crack radius parameter (CL-AVG) and total number of cracks (CN-TOT). The total crack area is given and the cumulative rotation (ROT) in radius is provided. The quantity ROT gives the rotation of the crack bins from their original orientation; it is not necessarily the total cell rotation. Figure B-6 contains a portion of the historical listing of some stresses. From left to right the quantities are TXX(3,8), P(3,8), TXX(3,9), P(3,9), TXX(3,10), P(3,10), TXX(4,2), P(4,2), P(4,2), TXX(4,3), and P(4,3). Figure B-10 contains a similar historical listing for stresses and pressures at coordinate points (4,4), (4,5), (4,6), (4,7) and (4,8).

The computed fracture and fragmentation damage is shown schematically in Fig. IV-1 of Section IV.

The fragmentation subroutines for DFRACT and BFRACT are listed at the end of this appendix.

NOMENCLATURE OF BFRACT, DFRACT, AND THE CALLING PROGRAM

Formal and External Parameters

DROT	Cell rotation during time increment, positive counter-clockwise, in radians
DTO (or DELTH)	Time increment, sec
E	Internal energy at beginning or end of time step, erg/g
EEST	Estimated internal energy based on constant P through time step, erg/g
EQSTCM (or CA)	Bulk modulus, dyn/cm^2
EQSTGM	Gruneisen ratio
ELMU (or MU)	Shear modulus, dyn/cm^2
EXX, EYY, ETT, EXY	Strain increment in the x, y, and θ directions, shear strain ($\epsilon_{xy} + \epsilon_{yx}$) in the XY plane
F	Thermal strength reduction function
J	Lagrangian coordinate in the Y direction
K	Lagrangian coordinate in the X direction
LS	Initializing indicator 0 initialize on this CALL 1 computations only 2 print only
M	Material number
NFR	Indicator array for type of fracture 0 no fracture model 1 ductile fracture 2 brittle fracture and fragmentation
NM (or ENM)	Relative crack or void volume
NN (or ICYCLE)	Time increment number
NT (or ENT)	Crack or void density, $number/cm^3$
P	Pressure, dyn/cm^2
RHOS (or RHO)	Initial solid density, g/cm^3

SXX, SYY, STT, TXY	Deviator stress in the X,Y, and θ directions, and shear in the XY plane, dyn/cm^2 (With an appended N or EN, the quantity pertains to the previous time step; with an appended W, it refers to the end of the current time step.)
TSR (1)	Growth constant = 3/(4*ETA), $cm^2/dyn/sec$
TSR (2)	Growth threshold, dyn/cm^2
TSR (3)	Nucleation radius parameter, cm
TSR (4) and (6)	Parameters in the nucleation function, $no./cm^3/sec$ and dyn/cm^2 N = TSR(4)*EXP((P-TSR(5))/TSR(6))
TSR (5)	Nucleation threshold, dyn/cm^2
TSR (7), TSR (8)	Not used
TSR (9)	Switch to indicate whether stress or deviator stress governs nucleation 0 stress 1 deviator stress
TXX, TYY, TTT	Total stress in the X,Y, and θ directions
VO (or VW), VOLD (or VN)	Relative volume at end and beginning of time step
Y (or YY)	Yield strength, dyn/cm^2
YD	Work hardening modulus, $dyn/cm^2(g/cm^3)$

<u>Internal Variables</u>

CL	Cube of crack radius parameter, cm^3
CN	Crack density, $number/cm^3$
DELV, DELVA	Imposed and computed total volume change cm^3/g
DOLD, DH	Density at beginning or end of time step, g/cm^3
DPJ	Permitted step in pressure used in iteration control, dyn/cm^2
DV, DVO	Imposed change in specific volume, cm^3/g

DVSA	Change in solid volume, cm^3/g
FNUC	Fraction of cracks nucleated for each crack orientation group; FNUC equals solid angle subtended by the group, divided by 4π
NANG	Number of angular orientation groups
NLOOP	Number of subcycling iterations required
PG	Pressure estimate based on strain, growth and expansion, dyn/cm^2
PJ	Pressure estimate selected to start an iteration, dyn/cm^2
PN	Pressure estimate based on nucleation dyn/cm^2
PS	Pressure estimate based on strain, dyn/cm^2
RED,RED1	Damage-related reduction factors for deviator stress
SDH	Maximum value of deviator stress, dyn/cm^2
VSO	Solid volume at beginning of time step, cm^3/g
VVO,VV,VVA	Total crack or void volume, cm^3/g

Input Variables

(listed in order of occurrence in the input deck)

IMAX	Maximum number of time steps permitted
MIRR	Indicator; 9 means tapered flyer
NMTRLS	Number of materials
IJBUND	Geometry type; 3 means planar geometry with laterally immovable edges
IFCUT,TIMWITH,DELTAT	Unused
COSQ	Coefficient of quadrative artificial viscosity term
XD(2)	Flyer velocity, cm/sec
TS	Stop time, sec
TRIQ	Coefficient of "triangle Q" artificial viscosity for distortion control
IPRINT, KPRINT	Print frequency indicators
NKED, NJED	Numbers of historical edits requested. Following these indicators is a large array with sets of 4 numbers each. In each set the first number indicates target (1) or flyer (2). The second indicates the variable requested: TXX(1) or P(2). The third and fourth are K and J.
RHO	Original density, g/cm^3
CFP	A three-digit indicator. The tens column gives the fracture indicator, NFR.
DPY	A three-digit indicator for deviation stress and pressure parameters. Here it indicates that TENS will be inserted.
TSR	Fracture parameters

CA	Bulk modulus (dyn/cm^2) and first coefficient of the Hugoniot expansion $P = CA \cdot \mu + CB \cdot \mu^2 + CC \cdot \mu^3$ where μ = DH/RHO - 1.
CB,CC	See CA, dyn/cm^2
EQSTE	Sublimation energy, erg/g
EQSTG	Gruneisen ratio
EQSTH	$\gamma - 1$, where γ is the exponent describing expansion of a polytropic gas
PMIN	Maximum tensile stress permitted, dyn/cm^2
YCC, YCT	Yield strengths in compression and tension, dyn/cm^2
TENS	Spall strength at the interface, dyn/cm^2
NZONES	Number of zones with identical K-rows in either target or flyer (target is treated first).
DELX	Cell dimension in the X direction, cm
DELY	Cell dimension in the Y direction, cm (same for target and flyer)
KROWS	Number of K-rows (or cells in the X-direction) within the zone.
NMAT	Number of different materials in the Y-direction in each K-row.
NCELLS	Number of cells in the first material in the Y-direction
MATR	Material number for the first cells in the Y-direction
ITAPERED	Indicator for a tapered flyer
XLTOP	Thickness of flyer at the top, cm
XLBOT	Thickness of flyer at the bottom, cm

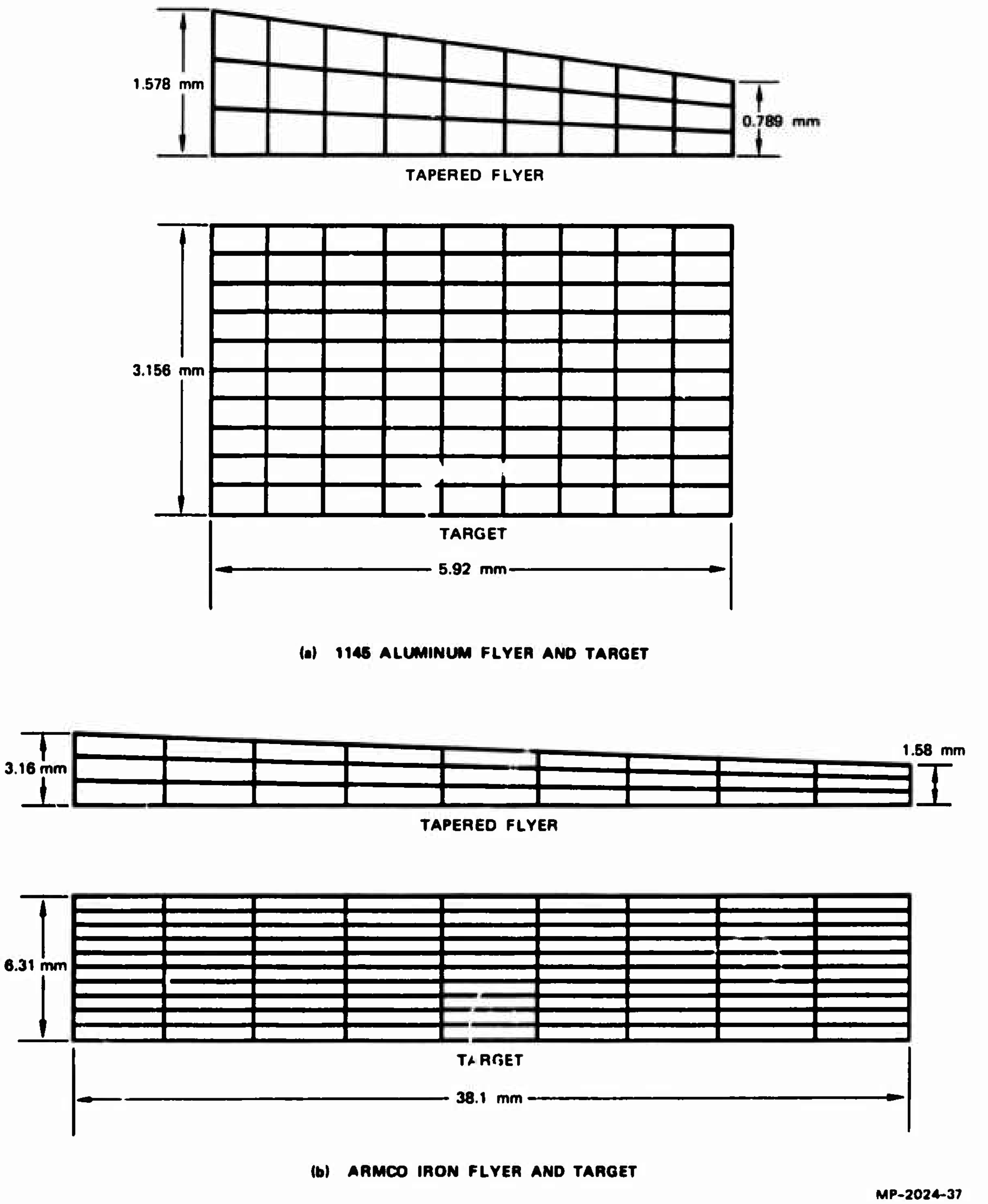

FIGURE B-1 PLANAR TWO-DIMENSIONAL GRIDS FOR CALCULATING TAPERED-FLYER IMPACTS IN 1145 ALUMINUM AND ARMCO IRON

```
DATE =  06/24/73
FIBROUS     AL 1145  TAPERED FLYER SHOT S4
IMAX=            100 MIRR =  9 NMTRLS= 2 IJBUND= 3 IFCUT = 0 TIMWITH = 1.000F+00
DELTAT =  5.000F-08 COS0 =     1.000E+00 XD(2)=    -1.630F+04 TS=         1.500F-06
TRIO =    0.                   -0.
IPRINT =           5 NKED =              0 KPRINT =         10 NJED =          236
            1 1 2 2   1 2 2 2   1 1 2 3   1 2 2 3   1 1 2 4   1 2 2 4   1 1 2 5
            1 2 2 5   1 1 2 6   1 2 2 6   1 1 2 7   1 2 2 7   1 1 2 8   1 2 2 8
            1 1 2 9   1 2 2 9   1 1 210   1 2 210   1 1 3 2   1 2 3 2   1 1 3 3
            1 2 3 3   1 1 3 4   1 2 3 4   1 1 3 5   1 2 3 5   1 1 3 6   1 2 3 6
            1 1 3 7   1 2 3 7   1 1 3 8   1 2 3 8   1 1 3 9   1 2 3 9   1 1 310
            1 2 310   1 1 4 2   1 2 4 2   1 1 4 3   1 2 4 3   1 1 4 4   1 2 4 4
            1 1 4 5   1 2 4 5   1 1 4 6   1 2 4 6   1 1 4 7   1 2 4 7   1 1 4 8
            1 2 4 8   1 1 4 9   1 2 4 9   1 1 410   1 2 410   1 1 5 2   1 2 5 2
            1 1 5 3   1 2 5 3   1 1 5 4   1 2 5 4   1 1 5 5   1 2 5 5   1 1 5 6
            1 2 5 6   1 1 5 7   1 2 5 7   1 1 5 8   1 2 5 8   1 1 5 9   1 2 5 9
            1 1 510   1 2 510   1 1 6 2   1 2 6 2   1 1 6 3   1 2 6 3   1 1 6 4
            1 2 6 4   1 1 6 5   1 2 6 5   1 1 6 6   1 2 6 6   1 1 6 7   1 2 6 7
            1 1 6 8   1 2 6 8   1 1 6 9   1 2 6 9   1 1 610   1 2 610   1 1 7 2
            1 2 7 2   1 1 7 3   1 2 7 3   1 1 7 4   1 2 7 4   1 1 7 5   1 2 7 5
            1 1 7 6   1 2 7 6   1 1 7 7   1 2 7 7   1 1 7 8   1 2 7 8   1 1 7 9
            1 2 7 9   1 1 710   1 2 710   1 1 8 2   1 2 8 2   1 1 8 3   1 2 8 3
            1 1 8 4   1 2 8 4   1 1 8 5   1 2 8 5   1 1 8 6   1 2 8 6   1 1 8 7
            1 2 8 7   1 1 8 8   1 2 8 8   1 1 8 9   1 2 8 9   1 1 810   1 2 810
            1 1 9 2   1 2 9 2   1 1 9 3   1 2 9 3   1 1 9 4   1 2 9 4   1 1 9 5
            1 2 9 5   1 1 9 6   1 2 9 6   1 1 9 7   1 2 9 7   1 1 9 8   1 2 9 8
            1 1 9 9   1 2 9 9   1 1 910   1 2 910   1 110 2   1 210 2   1 110 3
            1 210 3   1 110 4   1 210 4   1 110 5   1 210 5   1 110 6   1 210 6
            1 110 7   1 210 7   1 110 8   1 210 8   1 110 9   1 210 9   1 11010
            1 21010   1 111 2   1 211 2   1 111 3   1 211 3   1 111 4   1 211 4
            1 111 5   1 211 5   1 111 6   1 211 6   1 111 7   1 211 7   1 111 8
            1 211 8   1 111 9   1 211 9   1 11110   1 21110   1 31110   1 41110
            2 1 2 2   2 2 2 2   2 1 2 3   2 2 2 3   2 1 2 4   2 2 2 4   2 1 2 5
            2 2 2 5   2 1 2 6   2 2 2 6   2 1 2 7   2 2 2 7   2 1 2 8   2 2 2 8
            2 1 2 9   2 2 2 9   2 1 210   2 2 210   2 1 3 2   2 2 3 2   2 1 3 3
            2 2 3 3   2 1 3 4   2 2 3 4   2 1 3 5   2 2 3 5   2 1 3 6   2 2 3 6
            2 1 3 7   2 2 3 7   2 1 3 8   2 2 3 8   2 1 3 9   2 2 3 9   2 1 310
            2 2 310   2 1 4 2   2 2 4 2   2 1 4 3   2 2 4 3   2 1 4 4   2 2 4 4
            2 1 4 5   2 2 4 5   2 1 4 6   2 2 4 6   2 1 4 7   2 2 4 7   2 1 4 8
            2 2 4 8   2 1 4 9   2 2 4 9   2 1 410   2 2 410
AL 1145 FR          RHO =      2.700F+00 CFP=  010 DPY=  001             NCON=    1
TSR =     -1.000F-02-4.000E+09 1.000E-04 3.000E+09-3.000F+09-4.000E+08-0.
CA =       7.600F+11 CB =      1.500F+12 EQSTF =    1.220F+11 EQSTG =    2.040F+00
EQSTH =    2.500F-01 CC =      0.        PMIN =    -9.999F+12
YCC=       2.000F+09 YCT=      2.000F+09 MU=        3.000F+11
TENS =     0.        0.       -1.000E+08-0.        -0.         -0.         -0.
AL 1145             RHO =      2.700F+00 CFP=  000 DPY=  001             NCON=    1
CA =       7.600F+11 CH =      1.500F+12 EQSTF =    1.220F+11 EQSTG =    2.040F+00
EQSTH =    2.500F-01 CC =      0.        PMIN =    -9.999F+12
YCC=       2.000F+09 YCT=      2.000F+09 MU=        3.000F+11
TENS =     0.        0.       -1.000F+08-0.        -0.         -0.         -0.
NZONES =             1 DELX(1) = 3.156E-02 DELY =   5.920F-02
KROWS =             10 NMAT =            1 NCELLS =           9 MATR=              1
ITAPERD =            1 XLTOP =   7.890F-02 XLHOT =  1.578F-01
NZONES =             1 DELX(2) = 2.630E-02
KROWS =              3 NMAT =            1 NCELLS =           9 MATR=              2
```

FIGURE B-2 LISTING OF THE INPUT DATA DECK FOR THE SAMPLE TAPERED-FLYER IMPACT IN 1145 ALUMINUM

```
**** ICYCLE=  65 TYME= 1.461E-06 DELTM= 2.883E-08 IRT,KT, AND JT=   2   3  10, CALTIM= 6.169E+01 KMIN,KMAX,KRED,KCUT=   1  11  11000
REGION   1, K-COL.    1              X(J=1)=-7.921E-03, Y(J=1)= 0.                        X,Y IN CM, STRESS IN DYN/CM2
  J        X          Y       TXXW       TYYW       TXYW       TTTW        FW         VW         PW       QQNH       SPSQ       XDNH       YDNH
  2-7.886E-03 5.944E-02 1.916E+08 1.446E+09 2.430E+08 7.164E+08 2.824E+06 9.994E-01 4.679E+08 3.167E+08 5.043E+11-3.354E+03 2.039E+02
  3-7.770E-03 1.188E-01 1.916E+08 1.446E+09 2.430E+08 7.164E+08 2.824E+06 9.994E-01 4.679E+08 3.167E+08 5.043E+11-3.443E+03 2.568E+02
  4-7.577E-03 1.781E-01 1.916E+08 1.446E+09 2.430E+08 7.164E+08 2.824E+06 9.994E-01 4.679E+08 3.167E+08 5.043E+11-3.369E+03 2.902E+02
  5-7.341E-03 2.374E-01 1.916E+08 1.446E+09 2.430E+08 7.164E+08 2.824E+06 9.994E-01 4.679E+08 3.167E+08 5.043E+11-3.250E+03 3.499E+02
  6-7.089E-03 2.966E-01 1.916E+08 1.446E+09 2.430E+08 7.164E+08 2.824E+06 9.994E-01 4.679E+08 3.167E+08 5.043E+11-3.190E+03 3.203E+02
  7-6.868E-03 3.557E-01 1.916E+08 1.446E+09 2.430E+08 7.164E+08 2.824E+06 9.994E-01 4.679E+08 3.167E+08 5.043E+11-3.219E+03 2.451E+02
  8-6.701E-03 4.147E-01 1.916E+08 1.446E+09 2.430E+08 7.164E+08 2.824E+06 9.994E-01 4.679E+08 3.167E+08 5.043E+11-3.240E+03 1.513E+02
  9-6.601E-03 4.738E-01 1.916E+08 1.446E+09 2.430E+08 7.164E+08 2.824E+06 9.994E-01 4.679E+08 3.167E+08 5.043E+11-3.223E+03 6.531E+01
 10-6.570E-03 5.328E-01 1.916E+08 1.446E+09 2.430E+08 7.164E+08 2.824E+06 9.994E-01 4.679E+08 3.167E+08 5.043E+11-3.213E+03 0.
REGION   1, K-COL.    2              X(J=1)= 2.354E-02, Y(J=1)= 0.                        X,Y IN CM, STRESS IN DYN/CM2
  J        X          Y       TXXW       TYYW       TXYW       TTTW        FW         VW         PW       QQNH       SPSQ       XDNH       YDNH
  2 2.359E-02 5.938E-02 7.315E+08-1.577E+09 2.753E+07-3.736E+08-1.201E+06 1.001E+00-5.352E+08 1.290E+08 5.031E+11-3.740E+03 2.368E+02
  3 2.373E-02 1.187E-01 7.682E+08-1.534E+09 2.933E+07-2.646E+08-6.298E+05 1.001E+00-4.583E+08 1.141E+08 5.032E+11-3.696E+03 2.674E+02
  4 2.394E-02 1.780E-01 8.240E+08-1.277E+09-2.079E+07-1.151E+09-1.135E+05 1.000E+00-2.830E+08 9.352E+07 5.034E+11-3.589E+03 2.036E+02
  5 2.420E-02 2.373E-01 7.349E+08-3.938E+08-6.497E+07 1.389E+08 3.469E+05 9.999E-01 8.206E+07 7.794E+07 5.038E+11-3.443E+03 1.513E+02
  6 2.447E-02 2.965E-01 6.455E+08 6.803E+08-1.120E+08 4.660E+08 6.285E+05 9.993E-01 5.282E+08 7.568E+07 5.043E+11-3.353E+03 9.245E+01
  7 2.470E-02 3.556E-01 6.447E+08 1.594E+09-1.170E+08 7.537E+08 6.591E+05 9.988E-01 9.315E+08 6.594E+07 5.048E+11-3.338E+03 5.545E+01
  8 2.488E-02 4.147E-01 6.398E+08 2.193E+09-1.228E+08 9.455E+08 6.626E+05 9.984E-01 1.199E+09 6.012E+07 5.051E+11-3.371E+03 2.830E+01
  9 2.498E-02 4.737E-01 6.489E+08 2.557E+09-1.039E+08 1.069E+09 7.831E+05 9.982E-01 1.360E+09 6.518E+07 5.053E+11-3.377E+03 8.374E+00
 10 2.502E-02 5.328E-01 6.102E+08 2.716E+09-3.984E+07 1.115E+09 8.667E+05 9.982E-01 1.413E+09 6.705E+07 5.054E+11-3.371E+03 0.
REGION   1, K-COL.    3              X(J=1)= 5.500E-02, Y(J=1)= 0.                        X,Y IN CM, STRESS IN DYN/CM2
  J        X          Y       TXXW       TYYW       TXYW       TTTW        FW         VW         PW       QQNH       SPSQ       XDNH       YDNH
  2 5.506E-02 5.934E-02 1.860E+09-4.436E+08-2.227E+07 6.226E+08 4.001E+06 9.995E-01 4.020E+08 2.778E+08 5.034E+11-4.472E+03-2.645E+01
  3 5.521E-02 1.187E-01 2.076E+09-2.713E+08-8.891E+07 7.756E+08 4.460E+06 9.993E-01 5.804E+08 2.631E+08 5.035E+11-4.308E+03-9.891E+01
  4 5.543E-02 1.779E-01 2.121E+09 4.708E+06-2.002E+08 8.613E+08 8.539E+05 9.990E-01 7.530E+08 2.425E+08 5.046E+11-4.158E+03-1.876E+02
  5 5.571E-02 2.372E-01 1.980E+09 5.462E+08-3.214E+08 9.170E+08 9.366E+05 9.999E-01 9.343E+08 2.133E+08 5.048E+11-3.960E+03-1.663E+02
  6 5.600E-02 2.964E-01 1.864E+09 1.174E+09-3.496E+08 1.018E+09 1.082E+06 9.985E-01 1.149E+09 1.831E+08 5.051E+11-3.844E+03 1.214E+01
  7 5.625E-02 3.555E-01 1.825E+09 1.707E+09-2.981E+08 1.119E+09 1.231E+06 9.982E-01 1.391E+09 1.592E+08 5.054E+11-3.769E+03 2.271E+02
  8 5.643E-02 4.146E-01 1.842E+09 2.075E+09-2.060E+08 1.175E+09 1.401E+06 9.980E-01 1.555E+09 1.427E+08 5.055E+11-3.714E+03 3.160E+02
  9 5.655E-02 4.737E-01 1.828E+09 2.300E+09-1.431E+08 1.184E+09 1.923E+06 9.979E-01 1.629E+09 1.414E+08 5.056E+11-3.708E+03 2.226E+02
 10 5.659E-02 5.328E-01 1.789E+09 2.493E+09-6.374E+07 1.204E+09 2.289E+06 9.978E-01 1.678E+09 1.502E+08 5.057E+11-3.699E+03 0.
REGION   1, K-COL.    4              X(J=1)= 8.642E-02, Y(J=1)= 0.                        X,Y IN CM, STRESS IN DYN/CM2
  J        X          Y       TXXW       TYYW       TXYW       TTTW        FW         VW         PW       QQNH       SPSQ       XDNH       YDNH
  2 8.648E-02 5.936E-02 3.128E+09 1.008E+09-8.876E+07 1.305E+09-6.474E+06 9.982E-01 1.356E+09 4.577E+08 5.038E+11-5.686E+03 4.831E+01
  3 8.665E-02 1.187E-01 3.141E+09 1.071E+09-2.496E+08 1.347E+09-4.556E+06 9.982E-01 1.382E+09 4.707E+08 5.038E+11-5.498E+03 1.007E+02
  4 8.690E-02 1.780E-01 3.074E+09 1.094E+09-3.803E+08 1.303E+09-4.120E+06 9.992E-01 1.367E+09 4.575E+08 5.038E+11-5.260E+03 8.049E+01
  5 8.721E-02 2.372E-01 2.899E+09 1.033E+09-4.741E+08 1.133E+09-4.156E+06 9.993E-01 1.275E+09 4.137E+08 5.038E+11-4.995E+03 5.165E+01
  6 8.752E-02 2.964E-01 2.760E+09 1.023E+09-5.192E+08 9.371E+08-4.132E+06 9.984E-01 1.226E+09 3.474E+08 5.037E+11-4.697E+03 2.418E+01
  7 8.779E-02 3.556E-01 2.709E+09 1.094E+09-4.936E+08 7.627E+08-3.640E+06 9.993E-01 1.257E+09 2.661E+08 5.037E+11-4.415E+03 2.384E+01
  8 8.798E-02 4.147E-01 2.857E+09 1.397E+09-4.345E+08 7.751E+08-2.711E+06 9.991E-01 1.459E+09 2.169E+08 5.038E+11-4.233E+03-2.855E+00
  9 8.811E-02 4.737E-01 2.945E+09 1.858E+09-2.975E+08 9.803E+08-1.545E+06 9.978E-01 1.700E+09 1.960E+08 5.039E+11-4.165E+03-1.655E+01
 10 8.815E-02 5.328E-01 2.832E+09 2.152E+09-9.486E+07 1.143E+09-8.080E+05 9.976E-01 1.856E+09 1.861E+08 5.040E+11-4.121E+03 0.
REGION   1, K-COL.    5              X(J=1)= 1.179E-01, Y(J=1)= 0.                        X,Y IN CM, STRESS IN DYN/CM2
  J        X          Y       TXXW       TYYW       TXYW       TTTW        FW         VW         PW       QQNH       SPSQ       XDNH       YDNH
  2 1.190E-01 5.937E-02 3.628E+09 1.534E+09-4.775E+07 1.830E+09 3.001E+06 1.001E+00 2.015E+09 3.162E+08 5.050E+11-6.490E+03 4.508E+01
  3 1.181E-01 1.187E-01 3.579E+09 1.509E+09-1.425E+08 1.767E+09 1.916E+06 1.001E+00 1.999E+09 2.862E+08 5.044E+11-6.234E+03 1.012E+02
  4 1.184E-01 1.780E-01 3.678E+09 1.581E+09-2.771E+08 1.746E+09-3.555E+05 9.995E-01 2.039E+09 2.631E+08 5.046E+11-5.969E+03 2.419E+02
  5 1.187E-01 2.373E-01 3.688E+09 1.697E+09-4.001E+08 1.755E+09-2.412E+06 9.984E-01 2.083E+09 2.638E+08 5.044E+11-5.732E+03 3.876E+02
  6 1.190E-01 2.965E-01 3.632E+09 1.806E+09-4.304E+08 1.768E+09-3.652E+06 9.977E-01 2.096E+09 3.058E+08 5.042E+11-5.520E+03 3.794E+02
  7 1.193E-01 3.557E-01 3.758E+09 1.934E+09-3.837E+08 1.825E+09-4.020E+06 9.973E-01 2.147E+09 3.394E+08 5.042E+11-5.305E+03 3.047E+02
  8 1.195E-01 4.147E-01 3.843E+09 2.035E+09-3.001E+08 1.819E+09-3.909E+06 9.972E-01 2.202E+09 3.633E+08 5.042E+11-5.171E+03 2.400E+02
  9 1.197E-01 4.738E-01 3.786E+09 1.995E+09-2.651E+08 1.689E+09-3.798E+06 9.973E-01 2.125E+09 3.555E+08 5.142E+11-5.053E+03 1.714E+02
 10 1.197E-01 5.328E-01 3.751E+09 1.958E+09-7.329E+07 1.609E+09-3.231E+06 9.975E-01 2.079E+09 3.507E+08 5.042E+11-4.997E+03 0.
REGION   1, K-COL.    6              X(J=1)= 1.497E-01, Y(J=1)= 0.                        X,Y IN CM, STRESS IN DYN/CM2
  J        X          Y       TXXW       TYYW       TXYW       TTTW        FW         VW         PW       QQNH       SPSQ       XDNH       YDNH
  2 1.498E-01 5.939E-02 4.114E+09 2.149E+09-1.472E+07 2.301E+09 2.610E+07 1.010E+00 2.696E+09 1.586E+08 5.073E+11-6.953E+03 3.537E+01
  3 1.499E-01 1.188E-01 4.217E+09 2.254E+09 5.970E+06 2.384E+09 2.561E+07 1.009E+00 2.748E+09 1.840E+08 5.072E+11-6.751E+03-4.413E+00
  4 1.501E-01 1.781E-01 4.241E+09 2.275E+09 8.304E+07 2.401E+09 2.315E+07 1.007E+00 2.777E+09 1.956E+08 5.069E+11-6.570E+03 5.151E+01
  5 1.503E-01 2.374E-01 4.343E+09 2.384E+09 1.129E+08 2.462E+09 1.833E+07 1.005E+00 2.841E+09 2.217E+08 5.063E+11-6.363E+03 6.711E+01
  6 1.506E-01 2.966E-01 4.397E+09 2.430E+09 7.976E+07 2.457E+09 1.231E+07 1.002E+00 2.861E+09 2.366E+08 5.057E+11-6.177E+03 1.658E+02
  7 1.508E-01 3.557E-01 4.566E+09 2.634E+09 2.279E+07 2.549E+09 7.663E+06 9.989E-01 2.970E+09 2.809E+08 5.051E+11-6.090E+03 2.049E+02
  8 1.511E-01 4.148E-01 4.596E+09 2.695E+09-1.613E+07 2.531E+09 4.446E+06 9.971E-01 2.963E+09 3.117E+08 5.048E+11-6.000E+03 2.676E+02
  9 1.512E-01 4.738E-01 4.572E+09 2.704E+09-3.014E+07 2.474E+09 3.283E+06 9.965E-01 2.913E+09 3.372E+08 5.046E+11-5.876E+03 1.614E+02
 10 1.513E-01 5.324E-01 4.485E+09 2.643E+09-1.445E+07 2.366E+09 3.098E+06 9.965E-01 2.809E+09 3.555E+08 5.045E+11-5.835E+03 0.
```

FIGURE B-3 PARTIAL LISTING OF STRESSES AND POSITIONS IN ALL CELLS AT 1.461 μsec AFTER THE TAPERED-FLYER IMPACTED THE ALUMINUM TARGET

DATE = 08/24/73 FIBROUS AL 1145 TAPERED FLYER SHOT S4
**** ICYCLE= 65 TYME= 1.461E-06
DUCTILE FRACTURE DAMAGE PRINT OUT
ENM IS RELATIVE VOID VOLUME, ENT IS VOID DENSITY, NUMBER/CM3
CELL(K,J) IS THE CELL TO THE LOWER LEFT OF POINT(K,J)

J=	2	3	4	5	6	7	8	9	10
K= 2									
ENM=	0.	0.	0.	0.	0.	0.	0.	0.	0.
ENT=	0.	0.	0.	0.	0.	0.	0.	0.	0.
K= 3									
ENM=	7.653E-09	3.547E-09	0.	0.	0.	0.	0.	0.	0.
ENT=	3.045E+02	1.411E+02	0.	0.	0.	0.	0.	0.	0.
K= 4									
ENM=	1.917E-05	1.029E-05	3.916E-06	1.278E-06	4.779E-07	2.110E-07	1.059E-07	5.401E-08	3.704E-08
ENT=	2.169E+05	1.342E+05	6.577E+04	2.965E+04	1.528E+04	8.207E+03	4.214E+03	2.149E+03	1.476E+03
K= 5									
ENM=	4.042E-03	3.342E-03	2.152E-03	1.106E-03	4.490E-04	1.943E-04	1.357E-04	1.625E-04	2.140E-04
ENT=	1.560E+07	1.269E+07	7.805E+06	3.872E+06	1.735E+06	9.291E+05	7.739E+05	1.018E+06	1.384E+06
K= 6									
ENM=	1.306E-02	1.225E-02	1.070E-02	8.273E-03	5.283E-03	2.716E-03	9.707E-04	2.780E-04	1.314E-04
ENT=	3.696E+07	3.645E+07	3.276E+07	2.462E+07	1.430E+07	6.379E+06	2.396E+06	9.745E+05	5.907E+05
K= 7									
ENM=	1.110E-02	1.061E-02	8.995E-03	6.132E-03	3.518E-03	2.025E-03	1.410E-03	1.254E-03	1.319E-03
ENT=	3.262E+07	3.109E+07	2.544E+07	1.616E+07	8.595E+06	5.335E+06	4.081E+06	3.767E+06	3.990E+06
K= 8									
ENM=	1.029E-03	9.418E-04	8.062E-04	1.185E-03	1.847E-03	1.926E-03	1.107E-03	4.753E-04	2.787E-04
ENT=	2.696E+06	2.486E+06	2.424E+06	4.201E+06	7.561E+06	7.858E+06	4.627E+06	2.286E+06	1.548E+06
K= 9									
ENM=	1.882E-05	1.643E-05	3.145E-05	3.807E-05	5.289E-05	3.539E-05	3.570E-05	1.652E-05	1.353E-05
ENT=	2.805E+05	2.515E+05	4.177E+05	4.836E+05	6.120E+05	4.555E+05	4.762E+05	2.561E+05	2.173E+05
K=10									
ENM=	7.381E-08	4.411E-08	2.500E-08	3.675E-08	4.789E-08	6.048E-08	7.457E-08	4.076E-08	1.440E-08
ENT=	2.900E+03	1.755E+03	9.948E+02	1.462E+03	1.905E+03	2.406E+03	2.960E+03	1.622E+03	5.730E+02
K=11									
ENM=	0.	0.	0.	0.	0.	0.	0.	0.	0.
ENT=	0.	0.	0.	0.	0.	0.	0.	0.	0.

FIGURE B-4 LISTING OF THE VOID VOLUME AND NUMBER OF VOIDS IN EACH CELL IN THE SAMPLE TAPERED-FLYER IMPACT IN ALUMINUM

```
DATE =  08/24/73   FIHROUS    AL 1145  TAPERED FLYER SHOT 54
NSCRIBE=  5 STRESS HISTORIES. - TIME IN MICROSECS. STRESS IN KBAR. VELOCITY IN MM/MICROSEC. VOLUME IN CC/GRAM
INTEGER CODE  RONOKOJ  WHERE R=REGION, N=TYPE - 1=TXX, 2=TYY, 3=TXY, 4=TTT, 5=SXX,6=SYY, 7=STT, 8=PW, 9=QQ, 10=TXYC
          OR NOROK WHERE N=TYPE - 0=AVERAGE STRESS, 1=AVERAGE SPECIFIC VOLUME, 2=AVERAGE PARTICLE VELOCITY,  R=REGION,  K=K-ROW
```

N	TIME	1010404	1020404	1010405	1020405	1010406	1020406	1010407	1020407	1010408	1020408
1	.000001	0.00000	0.00000	0.00000	0.00000	0.00000	0.00000	0.00000	0.00000	0.00000	0.00000
2	.001118	0.00000	0.00000	0.00000	0.00000	0.00000	0.00000	0.00000	0.00000	0.00000	0.00000
3	.002458	0.00000	0.00000	0.00000	0.00000	0.00000	0.00000	0.00000	0.00000	0.00000	0.00000
4	.004066	0.00000	0.00000	0.00000	0.00000	0.00000	0.00000	0.00000	0.00000	0.00000	0.00000
5	.005996	0.00000	0.00000	0.00000	0.00000	0.00000	0.00000	0.00000	0.00000	0.00000	0.00000
6	.008312	0.00000	0.00000	0.00000	0.00000	0.00000	0.00000	0.00000	0.00000	0.00000	0.00000
7	.011092	0.00000	0.00000	0.00000	0.00000	0.00000	0.00000	0.00000	0.00000	0.00000	0.00000
8	.014427	0.00000	0.00000	0.00000	0.00000	0.00000	0.00000	0.00000	0.00000	0.00000	0.00000
9	.018429	0.00000	0.00000	0.00000	0.00000	0.00000	0.00000	0.00000	0.00000	0.00000	0.00000
10	.023231	0.00000	0.00000	0.00000	0.00000	0.00000	0.00000	0.00000	0.00000	0.00000	0.00000
11	.028994	0.00000	0.00000	0.00000	0.00000	0.00000	0.00000	0.00000	0.00000	0.00000	0.00000
12	.035909	0.00000	0.00000	0.00000	0.00000	0.00000	0.00000	0.00000	0.00000	0.00000	0.00000
13	.044208	0.00000	0.00000	0.00000	0.00000	0.00000	0.00000	0.00000	0.00000	0.00000	0.00000
14	.054166	0.00000	0.00000	0.00000	0.00000	0.00000	0.00000	0.00000	0.00000	0.00000	0.00000
15	.066116	0.00000	0.00000	0.00000	0.00000	0.00000	0.00000	0.00000	0.00000	0.00000	0.00000
16	.080456	0.00000	0.00000	0.00000	0.00000	0.00000	0.00000	0.00000	0.00000	0.00000	0.00000
17	.097664	.00014	.00007	.00013	.00006	.00013	.00006	.00013	.00006	.00012	.00006
18	.118314	.00119	.00058	.00116	.00056	.00112	.00054	.00109	.00052	.00105	.00051
19	.143093	.00746	.00360	.00727	.00351	.00705	.00340	.00681	.00329	.00658	.00317
20	.171047	.04021	.01940	.03920	.01892	.03804	.01836	.03480	.01777	.03558	.01719
21	.199034	.16356	.07889	.15965	.07705	.15513	.07489	.15029	.07258	.14555	.07035
22	.227101	.50330	.24289	.49198	.23754	.47894	.23131	.46493	.22465	.45112	.21819
23	.255264	1.19031	.57498	1.16600	.56352	1.13911	.55022	1.10816	.53603	1.07853	.52229
24	.283532	2.21376	1.07061	2.17638	1.05311	2.13251	1.03233	2.08483	1.00994	2.03755	.98839
25	.311888	3.32527	1.60959	3.28532	1.59135	3.23808	1.54951	3.18724	1.54633	3.13694	1.52474
26	.340304	4.15637	2.15475	4.12785	2.12703	4.09454	2.09450	4.06062	2.06152	4.03051	2.03287
27	.368768	4.84409	2.84201	4.80197	2.80093	4.75367	2.75368	4.70589	2.70711	4.66569	2.66867
28	.397305	5.72781	3.72530	5.67404	3.67283	5.61318	3.61326	5.55363	3.55519	5.50442	3.50794
29	.425918	6.70419	4.70126	6.65495	4.65359	6.59938	4.59960	6.54465	4.54658	6.49995	4.50392
30	.454557	7.54147	5.53799	7.51246	5.51093	7.48005	5.48047	7.44932	5.45174	7.42702	5.43155
31	.483206	8.10840	6.10414	8.10720	6.10539	8.10489	6.10553	8.10442	6.10751	8.10949	6.11484
32	.511861	8.38767	6.38233	8.40990	6.40758	8.42936	6.43022	8.44728	6.45132	8.46593	6.47256
33	.540533	8.41604	6.40710	8.44227	6.43896	8.45947	6.46050	8.46566	6.47122	8.46160	6.47537
34	.569238	8.14438	6.26695	8.13888	6.28160	8.09437	6.27473	8.00858	6.24386	7.89145	6.19726
35	.597954	7.55708	5.96444	7.44672	5.92628	7.24436	5.84312	6.94621	5.71271	6.58436	5.55507
36	.626671	6.57898	5.46667	6.27930	5.32777	5.92183	5.12113	5.21115	4.84579	4.51366	4.54119
37	.655395	5.09904	4.71010	4.55542	4.44516	3.91082	4.10253	2.89936	3.69531	1.94478	3.29443
38	.684099	3.07591	3.67542	2.30537	3.29629	1.39085	2.88384	.58113	2.40736	-.01478	1.90030
39	.712805	.70711	2.46361	.14874	1.96896	-.40014	1.44219	-.94502	.94570	-1.43988	.51185
40	.741521	-.85023	1.02590	-1.35002	.52110	-1.88825	.00406	-2.38109	-.45096	-2.77041	-.79361
41	.770237	-2.24248	-.34530	-2.75084	-.85213	-3.27177	-1.35198	-3.67346	-1.71699	-3.89645	-1.90104
42	.798962	-3.55676	-1.65103	-4.00423	-2.09463	-4.42438	-2.40295	-4.67236	-2.70607	-4.71237	-2.70167
43	.827701	-4.68615	-2.78300	-4.97767	-3.07214	-5.24118	-3.31856	-5.31660	-3.35210	-5.20546	-3.18664
44	.856448	-5.54054	-3.65862	-5.60403	-3.72693	-5.62027	-3.72156	-5.51353	-3.56642	-5.28953	-3.27153
45	.885191	-6.03068	-4.18072	-5.82907	-4.00504	-5.58789	-3.74107	-5.31616	-3.44294	-5.04284	-3.06909
46	.913952	-6.20252	-4.40830	-5.74677	-4.03634	-5.31911	-3.62395	-4.98156	-3.24549	-4.77534	-2.89604
47	.942707	-6.19756	-4.47746	-5.62711	-4.00974	-5.12787	-3.56191	-4.83186	-3.21019	-4.71663	-2.91885
48	.971362	-6.16703	-4.51462	-5.60490	-4.05888	-5.15729	-3.64252	-4.87393	-3.28577	-4.70047	-2.94172
49	1.000061	-6.13998	-4.53776	-5.67084	-4.14563	-5.27115	-3.74573	-4.90667	-3.30660	-4.52270	-2.82144
50	1.028824	-5.83519	-4.41825	-5.55583	-4.09214	-5.16892	-3.69341	-4.71211	-3.19086	-4.20243	-2.64034

FIGURE B-5   PARTIAL LISTING OF STRESS HISTORIES IN THE SAMPLE TAPERED-FLYER IMPACT IN ALUMINUM

```
DATE =  12/05/73
FIBROUS   ARMCO IRON    TAPERED FLYER SHOT S1
IMAX=          150 MIRR =  9 NMTRLS= 2 IJBUND= 3 IFCUT = 0 TIMWITH = 1.000E+00
DELTAT =  5.000E-08 CUSQ =     4.000E+00 XD(2)=    -1.033E+04 TS=         2.800E-06
TRIQ =    1.500E-01             -0.
IPRINT =            5 NKED =               0 KPRINT =          10 NJED =          236
             1 1 2 2   1 2 2 2   1 1 2 3   1 2 2 3   1 1 2 4   1 2 2 4   1 1 2 5
             1 2 2 5   1 1 2 6   1 2 2 6   1 1 2 7   1 2 2 7   1 1 2 8   1 2 2 8
             1 1 2 9   1 2 2 9   1 1 210   1 2 210   1 1 3 2   1 2 3 2   1 1 3 3
             1 2 3 3   1 1 3 4   1 2 3 4   1 1 3 5   1 2 3 5   1 1 3 6   1 2 3 6
             1 1 3 7   1 2 3 7   1 1 3 8   1 2 3 8   1 1 3 9   1 2 3 9   1 1 310
             1 2 310   1 1 4 2   1 2 4 2   1 1 4 3   1 2 4 3   1 1 4 4   1 2 4 4
             1 1 4 5   1 2 4 5   1 1 4 6   1 2 4 6   1 1 4 7   1 2 4 7   1 1 4 8
             1 2 4 8   1 1 4 9   1 2 4 9   1 1 410   1 2 410   1 1 5 2   1 2 5 2
             1 1 5 3   1 2 5 3   1 1 5 4   1 2 5 4   1 1 5 5   1 2 5 5   1 1 5 6
             1 2 5 6   1 1 5 7   1 2 5 7   1 1 5 8   1 2 5 8   1 1 5 9   1 2 5 9
             1 1 510   1 2 510   1 1 6 2   1 2 6 2   1 1 6 3   1 2 6 3   1 1 6 4
             1 2 6 4   1 1 6 5   1 2 6 5   1 1 6 6   1 2 6 6   1 1 6 7   1 2 6 7
             1 1 6 8   1 2 6 8   1 1 6 9   1 2 6 9   1 1 610   1 2 610   1 1 7 2
             1 2 7 2   1 1 7 3   1 2 7 3   1 1 7 4   1 2 7 4   1 1 7 5   1 2 7 5
             1 1 7 6   1 2 7 6   1 1 7 7   1 2 7 7   1 1 7 8   1 2 7 8   1 1 7 9
             1 2 7 9   1 1 710   1 2 710   1 1 8 2   1 2 8 2   1 1 8 3   1 2 8 3
             1 1 8 4   1 2 8 4   1 1 8 5   1 2 8 5   1 1 8 6   1 2 8 6   1 1 8 7
             1 2 8 7   1 1 8 8   1 2 8 8   1 1 8 9   1 2 8 9   1 1 810   1 2 810
             1 1 9 2   1 2 9 2   1 1 9 3   1 2 9 3   1 1 9 4   1 2 9 4   1 1 9 5
             1 2 9 5   1 1 9 6   1 2 9 6   1 1 9 7   1 2 9 7   1 1 9 8   1 2 9 8
             1 1 9 9   1 2 9 9   1 1 910   1 2 910   1 110 2   1 210 2   1 110 3
             1 210 3   1 110 4   1 210 4   1 110 5   1 210 5   1 110 6   1 210 6
             1 110 7   1 210 7   1 110 8   1 210 8   1 110 9   1 210 9   1 11010
             1 21010   1 111 2   1 211 2   1 111 3   1 211 3   1 111 4   1 211 4
             1 111 5   1 211 5   1 111 6   1 211 6   1 111 7   1 211 7   1 111 8
             1 211 8   1 111 9   1 211 9   1 11110   1 21110   1 31110   1 41110
             2 1 2 2   2 2 2 2   2 1 2 3   2 2 2 3   2 1 2 4   2 2 2 4   2 1 2 5
             2 2 2 5   2 1 2 6   2 2 2 6   2 1 2 7   2 2 2 7   2 1 2 8   2 2 2 8
             2 1 2 9   2 2 2 9   2 1 210   2 2 210   2 1 3 2   2 2 3 2   2 1 3 3
             2 2 3 3   2 1 3 4   2 2 3 4   2 1 3 5   2 2 3 5   2 1 3 6   2 2 3 6
             2 1 3 7   2 2 3 7   2 1 3 8   2 2 3 8   2 1 3 9   2 2 3 9   2 1 310
             2 2 310   2 1 4 2   2 2 4 2   2 1 4 3   2 2 4 3   2 1 4 4   2 2 4 4
             2 1 4 5   2 2 4 5   2 1 4 6   2 2 4 6   2 1 4 7   2 2 4 7   2 1 4 8
             2 2 4 8   2 1 4 9   2 2 4 9   2 1 410   2 2 410
ARMCO FRACTURE      RHO =      7.850E+00 CFP=  020 DPY=  001             NCON=   1
TSR =      -6.000E-04-2.000E+08 5.000E-05 4.600E+12-3.000E+09-4.560E+09-0.
CA =       1.589E+12 CB =       5.170E+12 EQSTE =    7.360E+10 EQSTG =    1.690E+10
EQSTH =    2.500E-01 CC =       5.170E+13 PMIN =    -9.999E+12
YCC =      5.500E+09 YCT=       5.500E+09 MU=        8.190E+11
TENS =     0.        0.        -1.000E+00-0.         -0.         -0.         -0.
ARMCO IRON          RHO =      7.850E+00 CFP=  000 DPY=  001             NCON=   1
CA =       1.589E+12 CB =       5.170E+12 EQSTE =    7.360E+10 EQSTG =    1.690E+10
EQSTH =    2.500E-01 CC =       5.170E+13 PMIN =    -9.999E+12
YCC =      5.500E+09 YCT=       5.500E+09 MU=        8.190E+11
TENS =     0.        0.        -1.000E+00-0.         -0.         -0.         -0.
NZONES =            1 DELX(1) = 6.313E-02 DELY =     4.233E-01                     -0
KROWS =            10 NMAT =              1 NCELLS =           9 MATR=              1
ITAPERD =           1 XLTOP =   1.578E-01 XLBOT =    3.156E-01
NZONES =            1 DELX(2) = 7.000E-02
KROWS =             3 NMAT =              1 NCELLS =           9 MATR=              2
```

FIGURE B-6 LISTING OF THE INPUT DATA DECK FOR THE SAMPLE TAPERED-FLYER IMPACT IN ARMCO IRON

```
**** ICYCLE=  75 TYME= 2.744E-06 DELTM= 4.560E-08 IRT,KT, AND JT=   2   3  10, CALTIM= 8.118E+01 KMIN,KMAX,KRED,KCUT=   1  11  11*000
 REGION  1, K-COL.   1          X(J=1)=-1.057E-02, Y(J=1)= 0.              X,Y IN CM, STRESS IN DYN/CM2
   J        X          Y          TXXW       TYYW       TXYW       TTTW        EW          VW         PW        QQNH        SPSQ       XDNH       YDNH
   2-1.030E-02 4.230E-01 1.149E+08-1.206E+08-2.713E+07 7.890E+06 2.601E+05 1.000E+00 7.324E+05 0.                    4.111E+11-2.423E+03 2.692E+02
   3-9.951E-03 8.473E-01 1.149E+08-1.206E+08-2.713E+07 7.890E+06 2.601E+05 1.000E+00 7.324E+05 0.                    4.111E+11-2.438E+03 4.209E+02
   4-9.430E-03 1.271E+00 1.149E+08-1.206E+08-2.713E+07 7.890E+06 2.601E+05 1.000E+00 7.324E+05 0.                    4.111E+11-2.419E+03 5.374E+02
   5-8.816E-03 1.694E+00 1.149E+08-1.206E+08-2.713E+07 7.890E+06 2.601E+05 1.000E+00 7.324E+05 0.                    4.111E+11-2.399E+03 5.582E+02
   6-8.160E-03 2.118E+00 1.149E+08-1.206E+08-2.713E+07 7.890E+06 2.601E+05 1.000E+00 7.324E+05 0.                    4.111E+11-2.376E+03 4.885E+02
   7-7.507E-03 2.541E+00 1.149E+08-1.206E+08-2.713E+07 7.890E+06 2.601E+05 1.000E+00 7.324E+05 0.                    4.111E+11-2.387E+03 3.187E+02
   8-6.934E-03 2.964E+00 1.149E+08-1.206E+08-2.713E+07 7.890E+06 2.601E+05 1.000E+00 7.324E+05 0.                    4.111E+11-2.446E+03 1.143E+02
   9-6.566E-03 3.307E+00 1.149E+08-1.206E+08-2.713E+07 7.890E+06 2.601E+05 1.000E+00 7.324E+05 0.                    4.111E+11-2.525E+03 1.769E+01
  10-6.531E-03 3.810E+00 1.149E+08-1.206E+08-2.713E+07 7.890E+06 2.601E+05 1.000E+00 7.324E+05 0.                    4.111E+11-2.516E+03 0.
 REGION  1, K-COL.   2          X(J=1)= 5.254E-02, Y(J=1)= 0.              X,Y IN CM, STRESS IN DYN/CM2
   J        X          Y          TXXW       TYYW       TXYW       TTTW        EW          VW         PW        QQNH        SPSQ       XDNH       YDNH
   2 5.280E-02 4.237E-01 1.084E+08-2.217E+09-1.462E+08-5.655E+08 2.630E+03 1.001E+00-9.465E+08 5.525E+07 4.104E+11-2.481E+03 2.383E+02
   3 5.316E-02 8.473E-01 3.199E+08-1.287E+09 1.427E+08-2.410E+08 4.364E+04 1.000E+00-4.699E+08 6.705E+07 4.108E+11-2.477E+03 4.080E+02
   4 5.368E-02 1.271E+00 2.760E+08-8.053E+08 7.358E+07-1.222E+08 6.950E+04 1.000E+00-2.754E+08 5.818E+07 4.109E+11-2.456E+03 5.102E+02
   5 5.430E-02 1.694E+00 4.282E+08-3.125E+08 1.255E+08 6.368E+07 8.495E+04 1.000E+00-1.016E+07 6.996E+07 4.111E+11-2.422E+03 5.354E+02
   6 5.496E-02 2.117E+00 4.894E+08 2.288E+07 1.435E+08 1.766E+08 9.718E+04 9.999E-01 1.557E+08 7.396E+07 4.112E+11-2.389E+03 4.711E+02
   7 5.562E-02 2.541E+00 6.002E+08 5.263E+08 1.504E+08 3.524E+08 1.131E+05 9.997E-01 4.109E+08 8.206E+07 4.114E+11-2.388E+03 3.166E+02
   8 5.620E-02 2.964E+00 6.133E+08 1.342E+09 1.621E+08 5.800E+08 1.257E+05 9.995E-01 7.745E+08 7.069E+07 4.116E+11-2.439E+03 1.221E+02
   9 5.657E-02 3.307E+00 6.169E+08 2.228E+09 8.234E+07 8.096E+08 1.254E+05 9.993E-01 1.193E+09 2.498E+07 4.119E+11-2.522E+03 2.985E+01
  10 5.661E-02 3.810E+00 5.037E+08 2.354E+09 1.355E+08 8.067E+08 1.124E+05 9.992E-01 1.211E+09 1.044E+07 4.119E+11-2.519E+03 0.
 REGION  1, K-COL.   3          X(J=1)= 1.156E-01, Y(J=1)= 0.              X,Y IN CM, STRESS IN DYN/CM2
   J        X          Y          TXXW       TYYW       TXYW       TTTW        EW          VW         PW        QQNH        SPSQ       XDNH       YDNH
   2 1.159E-01 4.236E-01 4.197E+08-1.704E+09-1.590E+08-2.665E+08 3.532E+05 1.000E+00-7.228E+08 2.060E+08 4.106E+11-2.593E+03 1.971E+02
   3 1.163E-01 8.472E-01 6.917E+08-9.592E+08 1.444E+08 1.393E+07 3.936E+05 1.000E+00-2.812E+08 1.967E+08 4.109E+11-2.563E+03 3.667E+02
   4 1.168E-01 1.271E+00 7.206E+08-4.209E+08 1.625E+08 1.659E+08 4.203E+05 1.000E+00-1.773E+07 1.756E+08 4.111E+11-2.531E+03 4.602E+02
   5 1.174E-01 1.694E+00 9.225E+08 6.484E+06 2.285E+08 3.352E+08 4.563E+05 9.998E-01 2.569E+08 1.645E+08 4.113E+11-2.478E+03 4.871E+02
   6 1.181E-01 2.117E+00 1.066E+09 3.323E+08 2.801E+08 4.654E+08 4.814E+05 9.997E-01 4.794E+08 1.484E+08 4.114E+11-2.427E+03 4.344E+02
   7 1.187E-01 2.541E+00 1.229E+09 7.831E+08 2.999E+08 6.238E+08 5.146E+05 9.995E-01 7.499E+08 1.289E+08 4.116E+11-2.404E+03 2.990E+02
   8 1.193E-01 2.964E+00 1.299E+09 1.521E+09 2.647E+08 8.348E+08 5.590E+05 9.993E-01 1.125E+09 9.272E+07 4.119E+11-2.408E+03 1.246E+02
   9 1.197E-01 3.387E+00 1.310E+09 2.203E+09 1.863E+08 1.003E+09 5.934E+05 9.991E-01 1.474E+09 3.118E+07 4.121E+11-2.520E+03 3.846E+01
  10 1.197E-01 3.810E+00 1.163E+09 2.413E+09 1.983E+08 1.012E+09 5.853E+05 9.991E-01 1.518E+09 1.115E+07 4.122E+11-2.519E+03 0.
 REGION  1, K-COL.   4          X(J=1)= 1.788E-01, Y(J=1)= 0.              X,Y IN CM, STRESS IN DYN/CM2
   J        X          Y          TXXW       TYYW       TXYW       TTTW        EW          VW         PW        QQNH        SPSQ       XDNH       YDNH
   2 1.790E-01 4.236E-01 6.531E+08-1.248E+09-1.658E+08-9.381E+06 1.308E+05 1.000E+00-5.487E+08 3.474E+08 4.109E+11-2.752E+03 1.473E+02
   3 1.794E-01 8.471E-01 9.649E+08-6.289E+08 1.131E+08 2.374E+08 2.495E+05 1.000E+00-1.298E+08 3.209E+08 4.109E+11-2.653E+03 3.036E+02
   4 1.799E-01 1.271E+00 1.071E+09-8.966E+07 1.911E+08 4.027E+08 3.021E+05 9.999E-01 1.745E+08 2.867E+08 4.109E+11-2.643E+03 3.889E+02
   5 1.805E-01 1.694E+00 1.325E+09 3.010E+08 2.740E+08 5.708E+08 3.449E+05 9.997E-01 4.743E+08 2.579E+08 4.110E+11-2.566E+03 4.169E+02
   6 1.812E-01 2.117E+00 1.574E+09 6.014E+08 3.452E+08 7.095E+08 3.922E+05 9.995E-01 7.393E+08 2.224E+08 4.110E+11-2.491E+03 3.773E+02
   7 1.818E-01 2.540E+00 1.773E+09 1.013E+09 3.699E+08 8.621E+08 4.588E+05 9.994E-01 1.036E+09 1.796E+08 4.110E+11-2.438E+03 2.644E+02
   8 1.824E-01 2.964E+00 1.890E+09 1.630E+09 3.126E+08 1.044E+09 5.580E+05 9.991E-01 1.402E+09 1.212E+08 4.110E+11-2.447E+03 1.166E+02
   9 1.828E-01 3.387E+00 1.919E+09 2.167E+09 2.422E+08 1.169E+09 6.576E+05 9.989E-01 1.706E+09 4.586E+07 4.111E+11-2.522E+03 4.096E+01
  10 1.829E-01 3.810E+00 1.757E+09 2.396E+09 2.207E+08 1.174E+09 4.570E+05 9.989E-01 1.757E+09 1.866E+07 4.111E+11-2.520E+03 0.
 REGION  1, K-COL.   5          X(J=1)= 2.418E-01, Y(J=1)= 0.              X,Y IN CM, STRESS IN DYN/CM2
   J        X          Y          TXXW       TYYW       TXYW       TTTW        EW          VW         PW        QQNH        SPSQ       XDNH       YDNH
   2 2.421E-01 4.236E-01 7.856E+08 1.323E+08-1.746E+08 1.187E+09 3.878E+05 9.999E-01 2.351E+09 4.665E+08 4.110E+11-2.948E+03 9.366E+01
   3 2.425E-01 8.470E-01 1.125E+09 6.239E+08 6.194E+07 1.366E+09 5.075E+05 9.996E-01 6.108E+08 4.274E+08 4.110E+11-2.859E+03 2.272E+02
   4 2.430E-01 1.270E+00 1.305E+09 1.060E+09 1.750E+08 1.455E+09 5.645E+05 9.994E-01 8.908E+08 3.825E+08 4.110E+11-2.786E+03 3.029E+02
   5 2.436E-01 1.694E+00 1.617E+09 1.326E+09 2.693E+08 1.533E+09 6.081E+05 9.993E-01 1.155E+09 3.308E+08 4.110E+11-2.684E+03 3.310E+02
   6 2.442E-01 2.117E+00 1.927E+09 1.520E+09 3.466E+08 1.596E+09 6.621E+05 9.991E-01 1.397E+09 2.847E+08 4.110E+11-2.577E+03 3.028E+02
   7 2.449E-01 2.540E+00 2.188E+09 1.767E+09 3.733E+08 1.623E+09 7.026E+05 9.990E-01 1.636E+09 2.234E+08 4.111E+11-2.489E+03 2.136E+02
   8 2.455E-01 2.964E+00 2.343E+09 2.131E+09 3.081E+08 1.639E+09 7.474E+05 9.988E-01 1.893E+09 1.451E+08 4.111E+11-2.465E+03 9.626E+01
   9 2.459E-01 3.387E+00 2.389E+09 2.377E+09 2.513E+08 1.571E+09 7.575E+05 9.987E-01 2.056E+09 5.613E+07 4.111E+11-2.525E+03 3.607E+01
  10 2.459E-01 3.810E+00 2.226E+09 2.488E+09 2.138E+08 1.463E+09 7.188E+05 9.987E-01 2.040E+09 1.892E+07 4.111E+11-2.519E+03 0.
 REGION  1, K-COL.   6          X(J=1)= 3.049E-01, Y(J=1)= 0.              X,Y IN CM, STRESS IN DYN/CM2
   J        X          Y          TXXW       TYYW       TXYW       TTTW        EW          VW         PW        QQNH        SPSQ       XDNH       YDNH
   2 3.052E-01 4.235E-01 7.884E+08 4.601E+08-1.710E+08 1.249E+09 5.398E+05 9.998E-01 2.667E+08 5.659E+08 4.110E+11-3.171E+03 4.199E+01
   3 3.055E-01 8.470E-01 1.140E+09 7.126E+08 9.755E+06 1.272E+09 5.332E+05 9.997E-01 5.247E+08 5.165E+08 4.110E+11-3.055E+03 1.472E+02
   4 3.061E-01 1.270E+00 1.305E+09 1.077E+09 1.295E+08 1.348E+09 5.418E+05 9.995E-01 8.055E+08 4.644E+08 4.110E+11-2.957E+03 2.114E+02
   5 3.067E-01 1.694E+00 1.756E+09 1.353E+09 2.178E+08 1.473E+09 5.877E+05 9.993E-01 1.120E+09 4.075E+08 4.110E+11-2.826E+03 2.375E+02
   6 3.073E-01 2.117E+00 2.123E+09 1.596E+09 2.904E+08 1.612E+09 6.565E+05 9.991E-01 1.436E+09 3.427E+08 4.111E+11-2.684E+03 2.176E+02
   7 3.080E-01 2.540E+00 2.443E+09 1.925E+09 3.128E+08 1.767E+09 7.543E+05 9.989E-01 1.779E+09 2.661E+08 4.111E+11-2.558E+03 1.502E+02
   8 3.086E-01 2.963E+00 2.639E+09 2.288E+09 2.493E+08 1.883E+09 8.678E+05 9.987E-01 2.098E+09 1.717E+08 4.111E+11-2.495E+03 6.487E+01
   9 3.089E-01 3.387E+00 2.696E+09 2.434E+09 2.246E+08 1.833E+09 9.182E+05 9.986E-01 2.250E+09 7.070E+07 4.111E+11-2.533E+03 2.630E+01
  10 3.090E-01 3.810E+00 2.548E+09 2.470E+09 1.832E+08 1.702E+09 9.024E+05 9.986E-01 2.218E+09 2.161E+07 4.111E+11-2.518E+03 0.
```

FIGURE B-7 PARTIAL LISTING OF STRESSES AND POSITIONS IN ALL CELLS AT 2.744 μsec AFTER THE TAPERED-FLYER IMPACTED THE ARMCO IRON TARGET

DATE = 12/05/73 FIBROUS ARMCO IRON TAPERED FLYER SHOT S1
**** ICYCLE= 75 TYME= 2.744E-06

J=	2	3	4	5	6	7	8	9	10
K= 2									
ENM=	0.	0.	0.	0.	0.	0.	0.	0.	0.
ENT=	0.	0.	0.	0.	0.	0.	0.	0.	0.
K= 3									
ENM=	0.	0.	0.	0.	0.	0.	0.	0.	0.
ENT=	0.	0.	0.	0.	0.	0.	0.	0.	0.
K= 4									
ENM=	4.353E-07	3.583E-08	0.	0.	0.	0.	0.	0.	0.
ENT=	2.330E+06	2.079E+06	1.884E+06	1.790E+06	1.804E+06	1.798E+06	1.684E+06	1.518E+06	1.533E+06
K= 5									
ENM=	8.785E-08	0.	0.	0.	0.	0.	0.	0.	0.
ENT=	2.653E+06	2.613E+06	2.526E+06	2.504E+06	2.518E+06	2.504E+06	2.338E+06	2.258E+06	2.018E+06
K= 6									
ENM=	9.861E-08	0.	0.	0.	0.	0.	0.	0.	0.
ENT=	3.176E+06	2.890E+06	2.859E+06	2.732E+06	2.705E+06	2.615E+06	2.456E+06	2.273E+06	2.034E+06
K= 7									
ENM=	1.847E-07	0.	0.	0.	0.	0.	0.	0.	0.
ENT=	3.471E+06	3.143E+06	2.899E+06	2.804E+06	2.689E+06	2.479E+06	2.324E+06	1.949E+06	1.887E+06
K= 8									
ENM=	5.156E-06	0.	0.	0.	0.	0.	0.	0.	0.
ENT=	3.325E+06	2.991E+06	2.723E+06	2.557E+06	2.376E+06	2.039E+06	1.808E+06	1.460E+06	8.808E+05
K= 9									
ENM=	3.493E-06	7.297E-07	0.	0.	0.	0.	0.	0.	0.
ENT=	2.686E+06	2.438E+06	2.104E+06	1.795E+06	1.450E+06	0.	0.	0.	0.
K=10									
ENM=	4.764E-07	1.120E-07	0.	0.	0.	0.	0.	0.	0.
ENT=	1.635E+06	1.242E+06	0.	0.	0.	0.	0.	0.	0.
K=11									
ENM=	0.	0.	0.	0.	0.	0.	0.	0.	0.
ENT=	0.	0.	0.	0.	0.	0.	0.	0.	0.

FIGURE B-8 LISTING OF THE CRACK OPENING VOLUME AND NUMBER OF CRACKS IN EACH CELL IN THE SAMPLE TAPERED-FLYER IMPACT IN ARMCO IRON

LISTING OF CRACK LENGTH AND NUMBER FOR EVERY FRACTURING CELL

```
CELL   CL =  2.425E-04 2.082E-04 1.502E-04 1.680E-04   0.      CL-AVG =  2.132E-04  PI*N*R**2 =  3.255E-01
 4  2  CN =  9.040E+05 7.301E+05 1.484E+05 5.479E+05   0.      CN-TOT =  2.330E+06        ROT =  4.347E-04

CELL   CL =  2.418E-04 1.915E-04 0.        1.482E-04   0.      CL-AVG =  2.102E-04  PI*N*R**2 =  2.800E-01
 4  3  CN =  9.077E+05 7.005E+05 0.        4.704E+05   0.      CN-TOT =  2.079E+06        ROT =  8.289E-04

CELL   CL =  2.167E-04 1.676E-04 0.        1.255E-04   0.      CL-AVG =  1.879E-04  PI*N*R**2 =  2.021E-01
 4  4  CN =  8.512E+05 6.559E+05 0.        3.767E+05   0.      CN-TOT =  1.884E+06        ROT =  1.154E-03

CELL   CL =  2.184E-04 1.665E-04 0.        1.213E-04   0.      CL-AVG =  1.890E-04  PI*N*R**2 =  1.939E-01
 4  5  CN =  8.243E+05 6.284E+05 0.        3.371E+05   0.      CN-TOT =  1.790E+06        ROT =  1.407E-03

CELL   CL =  2.133E-04 1.625E-04 0.        1.168E-04   0.      CL-AVG =  1.845E-04  PI*N*R**2 =  1.760E-01
 4  6  CN =  8.308E+05 6.359E+05 0.        3.370E+05   0.      CN-TOT =  1.804E+06        ROT =  1.544E-03

CELL   CL =  2.046E-04 1.562E-04 0.        1.098E-04   0.      CL-AVG =  1.769E-04  PI*N*R**2 =  1.704E-01
 4  7  CN =  8.278E+05 6.375E+05 0.        3.332E+05   0.      CN-TOT =  1.798E+06        ROT =  1.572E-03

CELL   CL =  1.912E-04 1.466E-04 0.        1.006E-04   0.      CL-AVG =  1.667E-04  PI*N*R**2 =  1.416E-01
 4  8  CN =  8.106E+05 5.875E+05 0.        2.860E+05   0.      CN-TOT =  1.684E+06        ROT =  1.405E-03

CELL   CL =  1.832E-04 1.281E-04 0.        9.369E-05   0.      CL-AVG =  1.577E-04  PI*N*R**2 =  1.134E-01
 4  9  CN =  7.615E+05 5.122E+05 0.        2.448E+05   0.      CN-TOT =  1.518E+06        ROT =  8.999E-04

CELL   CL =  1.911E-04 1.078E-04 0.        9.913E-05   0.      CL-AVG =  1.597E-04  PI*N*R**2 =  1.144E-01
 4 10  CN =  7.723E+05 4.164E+05 0.        3.439E+05   0.      CN-TOT =  1.533E+06        ROT =  2.445E-04

CELL   CL =  3.971E-04 2.175E-04 0.        1.689E-04   0.      CL-AVG =  3.214E-04  PI*N*R**2 =  7.825E-01
 5  2  CN =  1.227E+06 7.942E+05 0.        6.315E+05   0.      CN-TOT =  2.653E+06        ROT =  4.067E-04

CELL   CL =  3.939E-04 2.170E-04 0.        1.493E-04   0.      CL-AVG =  3.208E-04  PI*N*R**2 =  7.629E-01
 5  3  CN =  1.265E+06 8.041E+05 0.        5.442E+05   0.      CN-TOT =  2.613E+06        ROT =  8.294E-04

CELL   CL =  3.937E-04 2.077E-04 0.        1.391E-04   0.      CL-AVG =  3.233E-04  PI*N*R**2 =  7.501E-01
 5  4  CN =  1.263E+06 7.770E+05 0.        4.861E+05   0.      CN-TOT =  2.526E+06        ROT =  1.185E-03

CELL   CL =  3.889E-04 2.071E-04 0.        1.346E-04   0.      CL-AVG =  3.180E-04  PI*N*R**2 =  7.183E-01
 5  5  CN =  1.230E+06 7.908E+05 0.        4.836E+05   0.      CN-TOT =  2.504E+06        ROT =  1.442E-03

CELL   CL =  3.739E-04 2.061E-04 0.        1.315E-04   0.      CL-AVG =  3.064E-04  PI*N*R**2 =  6.736E-01
 5  6  CN =  1.230E+06 8.041E+05 0.        4.847E+05   0.      CN-TOT =  2.518E+06        ROT =  1.541E-03

CELL   CL =  3.484E-04 2.021E-04 0.        1.262E-04   0.      CL-AVG =  2.865E-04  PI*N*R**2 =  5.899E-01
 5  7  CN =  1.211E+06 8.112E+05 0.        4.821E+05   0.      CN-TOT =  2.504E+06        ROT =  1.634E-03

CELL   CL =  3.197E-04 1.939E-04 0.        1.181E-04   0.      CL-AVG =  2.650E-04  PI*N*R**2 =  4.751E-01
 5  8  CN =  1.139E+06 7.652E+05 0.        4.340E+05   0.      CN-TOT =  2.338E+06        ROT =  1.468E-03

CELL   CL =  2.967E-04 1.694E-04 0.        1.098E-04   0.      CL-AVG =  2.446E-04  PI*N*R**2 =  3.880E-01
 5  9  CN =  1.109E+06 7.209E+05 0.        4.280E+05   0.      CN-TOT =  2.258E+06        ROT =  9.520E-04

CELL   CL =  2.695E-04 1.298E-04 0.        1.149E-04   0.      CL-AVG =  2.225E-04  PI*N*R**2 =  2.842E-01
 5 10  CN =  1.043E+06 5.134E+05 0.        4.618E+05   0.      CN-TOT =  2.018E+06        ROT =  2.736E-04

CELL   CL =  5.395E-04 2.542E-04 0.        1.977E-04   0.      CL-AVG =  4.322E-04  PI*N*R**2 =  1.650E+00
 6  2  CN =  1.500E+06 9.037E+05 0.        7.719E+05   0.      CN-TOT =  3.176E+06        ROT =  3.350E-04

CELL   CL =  4.561E-04 2.251E-04 0.        1.673E-04   0.      CL-AVG =  3.689E-04  PI*N*R**2 =  1.104E+00
 6  3  CN =  1.395E+06 8.546E+05 0.        6.404E+05   0.      CN-TOT =  2.890E+06        ROT =  6.896E-04

CELL   CL =  4.524E-04 2.217E-04 0.        1.554E-04   0.      CL-AVG =  3.657E-04  PI*N*R**2 =  1.069E+00
 6  4  CN =  1.384E+06 8.581E+05 0.        6.164E+05   0.      CN-TOT =  2.859E+06        ROT =  9.954E-04

CELL   CL =  4.387E-04 2.191E-04 0.        1.510E-04   0.      CL-AVG =  3.563E-04  PI*N*R**2 =  9.738E-01
 6  5  CN =  1.337E+06 8.235E+05 0.        5.710E+05   0.      CN-TOT =  2.732E+06        ROT =  1.228E-03

CELL   CL =  4.116E-04 2.105E-04 0.        1.434E-04   0.      CL-AVG =  3.346E-04  PI*N*R**2 =  8.530E-01
 6  6  CN =  1.319E+06 8.222E+05 0.        5.631E+05   0.      CN-TOT =  2.705E+06        ROT =  1.375E-03

CELL   CL =  3.766E-04 1.982E-04 0.        1.352E-04   0.      CL-AVG =  3.080E-04  PI*N*R**2 =  7.039E-01
 6  7  CN =  1.288E+06 8.134E+05 0.        5.129E+05   0.      CN-TOT =  2.615E+06        ROT =  1.433E-03

CELL   CL =  3.410E-04 1.854E-04 0.        1.208E-04   0.      CL-AVG =  2.793E-04  PI*N*R**2 =  5.451E-01
 6  8  CN =  1.207E+06 7.575E+05 0.        4.920E+05   0.      CN-TOT =  2.456E+06        ROT =  1.295E-03

CELL   CL =  3.101E-04 1.643E-04 0.        1.134E-04   0.      CL-AVG =  2.563E-04  PI*N*R**2 =  4.255E-01
 6  9  CN =  1.161E+06 6.728E+05 0.        4.391E+05   0.      CN-TOT =  2.273E+06        ROT =  8.342E-04

CELL   CL =  2.736E-04 1.262E-04 0.        1.147E-04   0.      CL-AVG =  2.265E-04  PI*N*R**2 =  2.960E-01
 6 10  CN =  1.071E+06 5.030E+05 0.        4.598E+05   0.      CN-TOT =  2.034E+06        ROT =  2.470E-04

CELL   CL =  5.614E-04 2.588E-04 9.874E-05 2.099E-04   0.      CL-AVG =  4.395E-04  PI*N*R**2 =  1.831E+00
 7  2  CN =  1.529E+06 9.375E+05 1.878E+05 8.166E+05   0.      CN-TOT =  3.471E+06        ROT =  2.709E-04

CELL   CL =  5.517E-04 2.484E-04 0.        1.935E-04   0.      CL-AVG =  4.416E-04  PI*N*R**2 =  1.695E+00
 7  3  CN =  1.496E+06 9.218E+05 0.        7.255E+05   0.      CN-TOT =  3.143E+06        ROT =  5.901E-04

CELL   CL =  4.627E-04 2.166E-04 0.        1.647E-04   0.      CL-AVG =  3.719E-04  PI*N*R**2 =  1.115E+00
 7  4  CN =  1.387E+06 8.595E+05 0.        6.522E+05   0.      CN-TOT =  2.899E+06        ROT =  8.229E-04

CELL   CL =  4.351E-04 2.075E-04 0.        1.539E-04   0.      CL-AVG =  3.512E-04  PI*N*R**2 =  9.648E-01
 7  5  CN =  1.359E+06 8.106E+05 0.        6.346E+05   0.      CN-TOT =  2.804E+06        ROT =  1.023E-03
```

FIGURE B-9 DETAILED LISTING OF FRACTURE DAMAGE IN EACH CELL IN THE SAMPLE TAPERED-FLYER IMPACT IN ARMCO IRON

DATE = 12/05/73 FIBROUS ARMCO IRON TAPERED FLYER SHOT S1
NSCRIBE= 4 STRESS HISTORIES, - TIME IN MICROSECS, STRESS IN KBAR, VELOCITY IN MM/MICROSEC, VOLUME IN CC/GRAM
INTEGER CODE RONOKOJ WHERE R=REGION, N=TYPE - 1=TXX, 2=TYY, 3=TXY, 4=TTT, 5=SXX,6=SYY, 7=STT, 8=P=, 9=QQ, 10=TXYC
OR NOROK WHERE N=TYPE - 0=AVERAGE STRESS, 1=AVERAGE SPECIFIC VOLUME, 2=AVERAGE PARTICLE VELOCITY, R=REGION, K=K-ROW

N	TIME	1010308	1020308	1010309	1020309	1010310	1020310	1010402	1020402	1010403	1020403
1	.000001	0.00000	0.00000	0.00000	0.00000	0.00000	0.00006	0.00000	0.00000	0.00000	0.00000
2	.001751	0.00000	0.00000	0.00000	0.00000	0.00000	0.00000	0.00000	0.00000	0.00000	0.00000
3	.003851	0.00000	0.00000	0.00000	0.00000	0.00000	0.00000	0.00000	0.00000	0.00000	0.00000
4	.006371	0.00000	0.00000	0.00000	0.00000	0.00000	0.00000	0.00000	0.00000	0.00000	0.00000
5	.009395	0.00000	0.00000	0.00000	0.00000	0.00000	0.00000	0.00000	0.00000	0.00000	0.00000
6	.013024	0.00000	0.00000	0.00000	0.00000	0.00000	0.00000	0.00000	0.00000	0.00000	0.00000
7	.017378	0.00000	0.00000	0.00000	0.00000	0.00000	0.00000	0.00000	0.00000	0.00000	0.00000
8	.022604	0.00000	0.00000	0.00000	0.00000	0.00000	0.00000	0.00000	0.00000	0.00000	0.00000
9	.028874	0.00000	0.00000	0.00000	0.00000	0.00000	0.00000	0.00000	0.00000	0.00000	0.00000
10	.036399	0.00000	0.00000	0.00000	0.00000	0.00000	0.00000	0.00000	0.00000	0.00000	0.00000
11	.045429	0.00000	0.00000	0.00000	0.00000	0.00000	0.00000	0.00000	0.00000	0.00000	0.00000
12	.056264	0.00000	0.00000	0.00000	0.00000	0.00000	0.00000	0.00000	0.00000	0.00000	0.00000
13	.069267	0.00000	0.00000	0.00000	0.00000	0.00000	0.00000	0.00000	0.00000	0.00000	0.00000
14	.084870	0.00000	0.00000	0.00000	0.00000	0.00000	0.00000	.00022	.00009	.00022	.00009
15	.103594	0.00000	0.00000	0.00000	0.00000	0.00000	0.00000	.00126	.00049	.00125	.00049
16	.126062	.00031	.00012	.00030	.00012	.00029	.00011	.00488	.00190	.00481	.00187
17	.153025	.00191	.00074	.00183	.00071	.00178	.00069	.01696	.00660	.01674	.00651
18	.185379	.00797	.00310	.00765	.00298	.00746	.00290	.05460	.02124	.05391	.02098
19	.224205	.03087	.01201	.02969	.01155	.02898	.01128	.16328	.06354	.16132	.06277
20	.269205	.10532	.04098	.10149	.03951	.09925	.03862	.43746	.17030	.43259	.16840
21	.314205	.28139	.10953	.27198	.10591	.26658	.10381	.94136	.36671	.93181	.36300
22	.359205	.61404	.23915	.59585	.23217	.58561	.22828	1.69429	.66065	1.67925	.65486
23	.404205	1.12892	.44002	1.10097	.42935	1.08550	.42370	2.64963	1.03432	2.62933	1.02662
24	.449205	1.79844	.70165	1.76183	.68780	1.74186	.68096	3.71475	1.45172	3.69166	1.44324
25	.494205	2.56205	1.00057	2.52005	.98494	2.49738	.97809	4.80866	1.88112	4.78331	1.87232
26	.539205	3.33198	1.30247	3.28442	1.28517	3.25830	1.27866	5.83949	2.28618	5.81494	2.27861
27	.584205	4.05419	1.58611	4.00189	1.56766	3.97150	1.56196	6.74271	2.64106	6.71881	2.63511
28	.629205	4.64371	1.81790	4.58039	1.79613	4.54057	1.79008	7.48510	2.93220	7.46252	2.92866
29	.674205	5.08747	1.99250	5.01239	1.96747	4.96235	1.96169	8.02209	3.14154	7.99900	3.14027
30	.719205	5.35897	2.09932	5.26948	2.07043	5.20621	2.06462	8.42018	3.29518	8.39346	3.29553
31	.764205	5.47641	2.14543	5.36308	2.10951	5.28085	2.10228	8.64906	3.38089	8.61702	3.38278
32	.809205	5.45689	2.13753	5.31420	2.09305	5.20831	2.08339	8.74865	3.41440	8.70837	3.41724
33	.854205	5.32448	2.08513	5.14705	2.03073	5.01445	2.01816	8.71425	3.39379	8.66380	3.39732
34	.899205	5.08006	1.98858	4.86346	1.92342	4.70100	1.90743	8.55818	3.32392	8.49169	3.32635
35	.944205	4.72951	1.85024	4.46024	1.77011	4.25626	1.74689	8.28426	3.20633	8.20398	3.20904
36	.989205	4.26724	1.66801	3.92176	1.56499	3.65822	1.52832	7.92066	3.05224	7.82288	3.05416
37	1.034205	3.67935	1.43653	3.232.0	1.30248	2.89230	1.24658	7.46354	2.86014	7.33962	2.85823
38	1.079205	2.95735	1.15266	2.39356	.98332	1.96697	.90574	6.89675	2.62366	6.73632	2.61417
39	1.124205	2.10926	.81982	1.42866	.61766	.91901	.52096	6.20727	2.33772	6.00108	2.31731
40	1.169205	1.16310	.44923	.38448	.22425	-.19180	.11623	5.39295	2.00149	5.13469	1.96806
41	1.214205	.16310	.05846	-.67860	-.17291	-1.29406	-.28017	4.46393	1.61904	4.15117	1.57204
42	1.259205	-.83797	-.33178	-1.69710	-.54882	-2.31735	-.64070	3.44063	1.19843	3.07500	1.13896
43	1.304205	-1.78741	-.70088	-2.61402	-.88125	-3.20259	-.94248	2.35044	.75040	1.93739	.68115
44	1.349205	-2.63951	-1.03110	-3.38562	-1.15330	-3.90831	-1.16967	1.22449	.28709	.77278	.21205
45	1.394205	-3.36003	-1.30919	-3.98449	-1.35445	-4.41289	-1.31419	.09480	-.17915	-.38424	-.25491
46	1.439205	-3.92798	-1.52702	-4.39993	-1.48071	-4.71393	-1.37543	-1.00795	-.63656	-1.50120	-.70725
47	1.484205	-4.33555	-1.68152	-4.63587	-1.53369	-4.82395	-1.35853	-2.05611	-1.07464	-2.54953	-1.13409
48	1.529205	-4.58602	-1.77381	-4.71636	-1.51890	-4.76497	-1.27232	-3.02626	-1.48458	-3.50564	-1.52654
49	1.574205	-4.68794	-1.80692	-4.62933	-1.44285	-4.56801	-1.12967	-3.89992	-1.85952	-4.35162	-1.87790
50	1.619205	-4.65035	-1.78351	-4.42940	-1.31559	-4.26474	-.94340	-4.66376	-2.19456	-5.07458	-2.18342

FIGURE B-10 PARTIAL LISTING OF STRESS HISTORIES IN THE SAMPLE TAPERED-FLYER IMPACT IN ARMCO IRON

```
      SUBROUTINE DFRACT(SXX,SYY,STT,TAY,EXX1,EYY1,ETT1,EXY1,P,NM,NT,VO,
     1   VOLD,DTO,E,EEST,EQSTCM,EQSTGM,ELMU,RHOS,TSR,Y,YD,F,M,ALFA)
C
C        PJ           ESTIMATE OF PRESSURE
C        PA           COMPUTED PRESSURE BASED ON PJ
C        PN,PG        PRESSURES ASSOCIATED WITH NUCLEATION AND GROWTH
C        NM           RELATIVE VOID VOLUME
C        NT           VOID DENSITY, NUMBER/CM3
C        TSR(1)       GROWTH CONSTANT = 3/(4*ETA)
C        TSR(2)       GROWTH THRESHOLD, DYN/CM2
C        TSR(3)       NUCLEATION RADIUS PARAMETER, CM
C        TSR(4),      PARAMETERS IN THE NUCLEATION FUNCTION :
C          TSR(6)          NDOT = T4*EXP((P-TSR(5))/TSR(6))
C        TSR(5)       NUCLEATION THRESHOLD, DYN/CM2
C        VVO, VVA     VOID VOLUME, CM3/G
C        VGA          VOID VOLUME ASSOCIATED WITH GROWTH, CM3/G
C        VNA          VOID VOLUME ASSOCIATED WITH NUCLEATION, CM3/G
C
      DIMENSION TSR(6,30)
      REAL NM,NT,MUN
      DATA SMF/1.86/
      IF (NM .LT. 0.) RETURN
      DOLD=RHOS/VOLD
      VVO=NM*VOLD/RHOS
      VSO=VOLD/RHOS-VVO
      PSO=P/(VSO*DOLD)    $    PCLD=P
      DVO=DV=(VO-VOLD)/RHOS
      IF (TSR(M,7) .EQ. 0.) TSR(M,7)=8.*3.1416*TSR(M,3)**3*TSR(M,4)
C ********
C              BEGIN SUBCYCLING LOOP FOR CASE OF LARGE STRAIN
C ********
      NLOOP=MAX1(1.,-2.*DV*EQSTCM/VSO/TSR(M,5)+0.5,2.5*TSR(M,1)*DTO*
     1   AMIN1(P-TSR(M,2),TSR(M,2)))
100   DELV=DV/NLOOP
      EXX=EXX1*DELV/DVO   $   EYY=EYY1*DELV/DVO
      ETT=ETT1*DELV/DVO   $   EXY=EXY1*DELV/DVO
      VH=VOLD/RHOS
      YT=Y
      EO=F
      DE=(EEST-E)/NLOOP
      DT=DELV/DVO*DTO
      A1=TSR(M,1)*DT
      DPJ=0.2*(ABS(TSR(M,5))+ABS(P))
      DO 380 NL=1,NLOOP
      VH=VH+DELV    $    E1=E0+DE
      DH=1./VH
      TEMP1=1./RHOS+EQSTGM*E1/EQSTCM
C
C             ESTIMATE OF PRESSURE BASED ON STRAIN, GROWTH, NUCLEATION
      PS=PG=PN=EQSTCM*(TEMP1/(VSO+DELV)-1.)
      IF (DELV .GT. 0.) PN=2.*TSR(M,6)*ALOG(DELV*DH/TSR(M,7)/DT)+
     1  2.*TSR(M,5) - PSO
      IF (VVO .LE. 0.) GO TO 150
      XN=0.    $ XP=1.0
      IF (PSO .LT. TSR(M,5)) XN=TSR(M,7)/DH*DT*EXP((PSO-TSR(M,5))/TSR(M,
     16))
      IF (PSO .LT. TSR(M,2)) XP=EXP(A1*(PSO-TSR(M,2)))
      PG = PSO+(DELV-VVO*(XP-1.)-XN-EQSTGM*(E1-E0)/EQSTCM)/(VVO*XP*A1/2.
     1   +XN/2./TSR(M,6)-1./RHOS/EQSTCM)
      IF (PG .GT. TSR(M,2)) PG = PSO + (DELV-VVO*(XP-1.)-EQSTGM*(E1-E0)/
```

```
     1   EQSTCM)*EQSTCM*RHOS
      IF (DELV .GT. 0. .AND. PSO .LT. TSR(M,2)) PG=AMIN1(PG,TSR(M,2))
150   PJ=AMAX1(PS,PG,PN)
      PJ = PSO + SIGN(AMIN1(ABS(PJ-PSO),10.*DPJ),PJ-PSO)
      DVS=TEMP1/(1.+PJ/EQSTCM)-VSO
      VVA=VVO+DELV-DVS
      NC=0.
C ********
C              BEGIN ITERATION LOOP
C ********
200   NC=NC+1
      VV=VVO+DELV-DVS
      PA = EQSTCM*(TEMP1/(VSO+DVS)-1.)
      PN=AMIN1(0.5*(PA+PSO)-TSR(M,5),0.)
      IF (PN .LT. 0.) PN=EXP(PN/TSR(M,6))
      VNA=TSR(M,7)*PN*DT/DH
      VGA=VVO
      PG=AMIN1(0.5*(PA+PSO)-TSR(M,2),0.)
      IF (PG .LT. 0.) VGA=VVO*EXP(A1*PG)
      VVA=VGA+VNA
      DVSA=TEMP1/(1.+PA/EQSTCM)-VSO
      DELVA=DVSA+VVA-VVO
      PJ=PA
C        TEST FOR COMPLETION OF ITERATIONS
      IF (ABS(DELVA-DELV)/VSO .LT. 2.E-5 .AND. ABS(DVS-DVSA)/VSO .LT.
     1  1.E-5) GO TO 300
      IF (NC .GE. 10) GO TO 450
      IF (NC .EQ. 1 .OR. MOD(NC,3) .EQ. 0) GO TO 270
C        INTERPOLATION TO FIND DVS
      DVS=DVSA+(DVSB-DVSA)/(DELVB-DELVA)*(DELV-DELVA)
      GO TO 280
270   PJ=PA+(DELV-DELVA)/(VGA*A1/2.-TEMP1/(EQSTCM+PA)+VNA/2./TSR(M,6))
      PN=PJ
      IF (VNA+DELV-DELVA .GT. 0. .AND. VNA .GT. 0.) PN=2.*TSR(M,6)*
     1  ALOG((VNA+DELV-DELVA)/VNA) + PA
      PJ=AMAX1(PJ,0.5*(PN+PJ))
      PJ=PA+SIGN(AMIN1(ABS(PJ-PA),DPJ),DELVA-DELV)
      DVS=TEMP1/(1.+PJ/EQSTCM)-VSO
      IF (NC .EQ. 1) GO TO 290
280   IF (ABS(DELVA-DELV) .GT. ABS(DELVB-DELV)) GO TO 200
290   DELVB=DELVA
      DVSB=DVSA
      GO TO 200
C        ENDING ROUTINE
C
300   NM=VVA*DH
      NT=NT*DH/DOLD+TSR(M,4)*PN*DT
      IF (NM .GT. 0.6) GO TO 400
      BETA=2.*TXY*ALFA/NLOOP
      ELMUF=2.*ELMU*AMAX1(1.-SMF*VVA*DH,0.)
      WS1=0.6667*(DOLD-DH)/(DOLD+DH)
      TXY=TXY-ELMUF/2.*EXY+(SYY-SXX)*ALFA/NLOOP
      SXX=SXX-ELMUF*(EXX-WS1)+BETA
      SYY=SYY-ELMUF*(EYY-WS1)-BETA
      STT=STT-ELMUF*(ETT-WS1)
      WS4=SXX**2+SYY**2+STT**2+2.*TXY**2
      YE=Y*F*AMAX1(1.-4.*VVA*DH,0.)
      IF (WS4 .LT. YE**2/1.5) GO TO 340
      WS3=YE/SQRT(1.5*WS4)
      PTERM=(DOLD-DH)/(DOLD+DH)/DT/TSR(M,1)
```

```
      WS5=1.5/TSR(M,1)/DT                                                DFR2 122
      SXX=SXX*WS3 - EXX*WS5 + PTERM                                      DFR2 123
      SYY=SYY*WS3 - EYY*WS5 + PTERM                                      DFR2 124
      STT=STT*WS3 - ETT*WS5 + PTERM                                      DFR2 125
      TXY=TXY*WS3 - EXY*WS5/2.                                           DFR2 126
  340 CONTINUE                                                           DFR2 127
      PSO = PJ                                                           DFR2 128
      PJ = PJ*(VSO+DVS)*DH                                               DFR2 129
      P=PJ                                                               DFR2 131
      Y=YT                                                               DFR2 132
      VVO=VVA                                                            DFR2 133
      VSO=1./DH-VVA                                                      DFR2 134
  380 DOLD=DH                                                            DFR2 135
      E=EEST+(POLD-PJ)*DVO/2.                                            DFR2 136
      RETURN                                                             DFR2 137
C                                                                        DFR2 138
C        END WITH SEPARATION                                             DFR2 139
  400 P=Y=SXX=SYY=STT=TXY=0.                                             DFR2 140
      NM=-ABS(NM)                                                        DFR2 141
      RETURN                                                             DFR2 142
C                                                                        DFR2 143
C                PROVISION FOR ABORT IN CASE OF ITERATION FAILURE        DFR2 144
  450 NTRY=NTRY+1                                                        DFR2 145
      IF (NTRY .GE. 5) GO TO 460                                         DFR2 146
      DV=VO/RHOS-1./DOLD                                                 DFR2 147
      NLOOP=MAX1(3.,-4.*2.**NTRY*DV*EQSTCM/VSO/TSR(M,5)+0.5)             DFR2 148
      GO TO 100                                                          DFR2 149
  460 PRINT 1600,M,S,P,DV,DELVA,DELVH                                    DFR2 150
      GO TO 300                                                          DFR2 151
 1600 FORMAT (*    ITERATION FAILURE IN DFRACT,   M=*I2,* S=*E10.3,      DFR2 152
     1 * P=*E10.3,* DV=*E10.3,* DELV=*2E10.3)                            DFR2 153
      END DFRACT                                                         DFR2 154
```

```
      SUBROUTINE BFRACT(LS,SXXEN,SYYEN,STTEN,TXYEN,EXX1,EYY1,ETT1,EXY1,
     1   P,NM,NT,VO,VOLO,UTO,E,EEST,EQSTCM,EQSTGM,ELMU,TSR,Y,YD,F,KS,JS,
     2   M,NN,RHOS,UHOT,IPRBFR)
C
C     NEM -- RELATIVE VOLUME OF CRACKS
C     NET -- NUMBER OF CRACKS/UNIT VOLUME
C     T1 -- CRACK GROWTH COEFFICIENT, CM2/DYN/SEC
C     T2 -- THRESHOLD STRESS FOR GROWTH, DYN/CM2
C     T3 -- PARAMETER OF NUCLEATION DISTRIBUTION, CM
C     T4 -- NUCLEATION RATE COEFFICIENT
C     T5 -- THRESHOLD STRESS FOR NUCLEATION
C     T6 -- DENOMINATOR OF EXPONENTIAL STRESS FUNCTION
C     T7 -- NOT USED
C     T8 -- THRESHOLD STRESS FOR ENTERING BFRACT
C     T9 -- SWITCH TO INDICATE WHETHER S OR SDH GOVERNS NUCLEATION
C              0 STRESS GOVERNS
C              1 DEVIATOR STRESS GOVERNS
C     CN -- CRACK DENSITY, NUMBER/CM3
C     CL -- CUBE OF CRACK RADIUS,CM3
C     IPRBFR(6) -- IPRBFR(1) =1 FOR EXTRA BFRACT ITERATION PRINTOUT
C
      DIMENSION TSR(6,30)
      DIMENSION CL(11,11,5),CN(11,11,5),COS2TH(4),SIN2TH(4),CL3(5),
     1   FNUC(5),ROT(11,11),STH(5),INIT(6)
      DIMENSION VCR(6),VCN(6)
      DIMENSION NTRI(11,11)
      DIMENSION IPRBFR(6)
      REAL NM,NT
      DATA SMF,NANG/1.88,5/
      IF (LS .GT. 0) GO TO 20
C         **********                                      ***********
C                I N I T I A L I Z A T I O N
C         **********                                      ***********
C ***     INITIALIZE GENERAL ARRAYS - COS2TH, SIN2TH, ROT, CN, CL, FNUC
      LS=1
      INIT(1)=INIT(2)=INIT(3)=INIT(4)=INIT(5)=INIT(6)=0
      NANG1=NANG-1
      FNUC(1)=0.707107/NANG1
      FNUC(NANG)=0.292893
      COS2TH(1)=1.0   $   SIN2TH(1)=0.
      DO 10 NG=2,NANG1
      FNUC(NG)=FNUC(1)
      TWOTH=6.2831853*FLOAT(NG-1)/FLOAT(NANG1)
      COS2TH(NG)=COS(TWOTH)
10    SIN2TH(NG)=SIN(TWOTH)
      DO 15 J=1,11
      DO 15 K=1,11
      ROT(K,J)=0.
      DO 15 NG=1,NANG
15    CN(K,J,NG)=CL(K,J,NG)=0.
C ***     INITIALIZE -TSR- COEFFICIENTS FOR EACH MATERIAL
20    IF (INIT(M) .EQ. M) GO TO 25
      TSR(M,3)=TSR(M,3)**3
      VCR(M)=8.*(1./ELMU+1./(EQSTCM+ELMU/3.))
      VCN(M)=-TSR(M,3)*TSR(M,4)
      INIT(M)=M
25    CONTINUE
      IF (LS .EQ. 2) GO TO 500
C         **********                                      ***********
C                C O M P U T A T I O N S
```

```
C         **********                                           ***********
      IF (NM .LT. 0.) RETURN
      VVO=NM*VOLD/RHOS
      VSO=VOLD/RHOS-VVO
      DV=DVO=(VO-VOLD)/RHOS
      DOLD=RHOS/VOLD
      PSO=P/(VSO*DOLD)
      R=ROT(KS,JS)   $   PO=P
C ***    SET VALUES FOR MULTIPLE LOOPS IN CASE OF LARGE STRAIN
C        MULTIPLE LOOPS IF STRAIN CORRESPONDS TO A STRESS GREATER THAN
C          0.33*TSR(M,5)
      NLOOP=MAX1(1.,-4.*DV*EQSTCM/VSO/TSR(M,5)+0.5)
      DPJ=0.2*(ABS(TSR(M,5))+ABS(PSO))
      NTRY=0
100   DELV=DV/NLOOP
      NTRI(KS,JS)=100*NLOOP+NTRY
      EXX=EXX1/NLOOP*DV/DVO   $   EYY=EYY1/NLOOP*DV/DVO
      ETT=ETT1/NLOOP*DV/DVO   $   EXY=EXY1/NLOOP*DV/DVO
      VH=1./DOLD    $    YT=Y   $   DE=(EEST-E)/NLOOP    $    E1=E
      DR=DELV/DVO*DROT    $    DT=DELV/DVO*DTO
      A1=3.*TSR(M,1)*DT         $   TEMP1=1./RHOS+EQSTGM*E/EQSTCM
C
C ***    BEGIN -DO- LOOP FOR EACH STEP IN STRAIN
      DO 380 NL=1,NLOOP
      VH=VH+DELV                $   DH=1./VH
      E1=E1+DE
      TEMPO=TEMP1
      TEMP1=1./RHOS+EQSTGM*E1/EQSTCM
      SDH=AMIN1(SXXEN,SYYEN,STTEN)
      VOPO=0.
      DO 120 NA=1,NANG
120   VOPO=VOPO+CN(KS,JS,NA)*CL(KS,JS,NA)
      VOPO=-VCR(M)*VOPO
C     *****      ESTIMATE SOLID PRESSURE TO BEGIN ITERATIONS       *****
C        STRAIN BASIS FOR PRESSURE ESTIMATE
      PS=PG=PN=EQSTCM*(TEMP1/(VSO+DELV)-1.)
      IF (P .LT. 0.) GO TO 130
C        CRACK OPENING BASIS FOR PRESSURE ESTIMATE
      PG=PSO+(DELV-TEMP1+VSO)/(VOPO-TEMP1/EQSTCM)
      IF (PG .GT. 0.) PG=PS
      GO TO 150
C        NUCLEATION BASIS FOR PRESSURE ESTIMATE
130   IF (DELV .GT. 0.) PN=-PSO+2.*TSR(M,5)+2.*TSR(M,6)*ALOG(ABS(DELV/
     1   VCR(M)/VCN(M)/DT/PSO))
C        GROWTH, EXPANSION, AND STRAIN BASIS FOR PRESSURE ESTIMATE
      XP=EXP(A1*AMIN1(0.,PSO+SDH-TSR(M,2)))
      PG=PSO+(DELV-VVO*XP+VVO-VSO+TEMPO/TEMP1*VSO)/(VVO*XP*(1./(PSO+SDH)
     1   +A1/2.)-VSO*VSO/EQSTCM/TEMP1)
150   PJ=AMAX1(PS,PG,PN)
      DVS=TEMP1/(1.+PJ/EQSTCM)-VSO
      COSR=COS(2.*R)
      SINR=SIN(2.*R)
C ***    COMPUTE STRESSES AT TIME(N-1) FOR EACH ANGULAR GROUP
      STH(NANG)=STTEN+PSO
      DO 170 NA=1,NANG1
170   STH(NA)=(SXXEN+SYYEN)/2.+PSO+(SXXEN-SYYEN)/2.*(COS2TH(NA)*COSR-
     1   SIN2TH(NA)*SINR)+TXYEN*(SIN2TH(NA)*COSR+COS2TH(NA)*SINR)
      SINR=SIN(2.*(R+DR))   $   COSR=COS(2.*(R+DR))
      NC=0
      IF (IPRBFR(1) .NE. 1) GO TO 1220
```

```
      PRINT 2010,NN,KS,JS
      PRINT 3001,VVO
      PRINT 1201,PJ,PS,PG,PN,P,DVS,DELV
2001  CONTINUE
3001  FORMAT(5X,* VVO=*E12.3)
1201  FORMAT(*  PJ=*E10.3,*, PS=*E10.3,*, PG=*E10.3,*, PN=*E10.3,*, P=*
     1   E10.3,*, DVS=*E10.3,*, DELV=*E10.3)
2010  FORMAT(5X,* NN=*I4,* KS,JS=*2I4)
1220  CONTINUE
C*********                                                    ********
C                     BEGIN ITERATION LOOP
C*********                                                    ********
200   CONTINUE
      NC=NC+1
      VV=VVO+DELV-DVS
C ***    COMPUTE PRESSURE
      PA=FQSTCM*(TEMP1/(VSO+DVS)-1.)
      VV=VH-VSO-DVS
C ***    COMPUTE DEVIATOR STRESS
      RED=AMAX1(0.,1.-4.*VV*DH)
      RED1=AMAX1(1.-SMF*VV*DH,0.)
      WS1=.66667*(DOLD-DH)/(DOLD+DH)
      BETA=2.*TXYEN*DROT*DELV/DV
      ELMUF=RED1*2.*ELMU
      TXYE=TXYEN-ELMUF/2.*EXY+(SYYEN-SXXEN)*DROT*DELV/DV
      SXXE=SXXEN-ELMUF*(EXX-WS1)+BETA
      SYYE=SYYEN-ELMUF*(EYY-WS1)-BETA
      STTE=STTEN-ELMUF*(ETT-WS1)
      WS4=SXXE**2+SYYE**2+STTE**2+2.*TXYE**2
      YE=YT*F*RED
      IF (WS4 .LE. YE**2/1.5 ) GO TO 230
      WS3=YE/SQRT(1.5*WS4)
      SXXE=SXXE*WS3
      SYYE=SYYE*WS3
      TXYE=TXYE*WS3
      STTE=STTE*WS3
230   CONTINUE
C ***    COMPUTATION OF CRACK VOLUME FROM ELASTIC OPENING, GROWTH,
C               NUCLEATION AND FRAGMENTATION
      VVA=0.
      DO 250 NA=1,NANG
      IF (NA .LT. NANG) GO TO 237
      STHW=STTE+PA   $  GO TO 240
237   STHW=PA+(SXXE+SYYE)/2.+(SXXE-SYYE)/2.*(COS2TH(NA)*COSR-SIN2TH(NA)*
     1   SINR)+TXYE*(SIN2TH(NA)*COSR+COS2TH(NA)*SINR)
240   SAVG=(STH(NA)+STHW)/2.
      DTC=CN(KS,JS,NA)*DH/DOLD*CL(KS,JS,NA)
      IF (SAVG .LT. TSR(M,2)) DTC=DTC*EXP(A1*(SAVG-TSR(M,2)))
      SCN=SAVG-TSR(M,9)*(PSO+PA)/2.-TSR(M,5)
      DTN=0.
      IF (SCN .LT. 0.) DTN=TSR(M,4)*EXP(SCN/TSR(M,6))*DT*FNUC(NA)
     1   *TSR(M,3)
      IF (STHW .LT. 0.) VVA=VVA-VCR(M)*STHW*(DTC+DTN)
250   CONTINUE
      VVA=VVA/DH
C ***    COMPUTE CHANGES IN V AND IN V SUB S
      SUH=AMIN1(SXXE,SYYE,STTE)
      DVSA=DVS
      DELVA=DVS+VVA-VVO
      PJ=PA
```

```
      IF (IPRBFR(1) .NE. 1) GO TO 1320
      PRINT 1301,NC,DVS,DVSA,DELV,DELVA,DV,VVA,PA,SDH
      PRINT 3002,SXXE,SYYE,STTE,TXYE
3002  FORMAT(5X,* SXXE,SYYE,STTE,TXYE=*4E12.3)
1301  FORMAT(1X,* NC=*I2,* DVS=*2E11.3,* DELV=*2E11.3,* DV=*E11.3,
     1 * VVA=*E11.3,* PA=*E11.3,* SDH=*E11.3)
1320  CONTINUE
C
C ***      TEST FOR COMPLETION OF ITERATIONS
      IF (ABS(DELVA-DELV)/VSO .LT. 2.E-5) GO TO 300
      IF (NC .GE. 10) GO TO 450
      IF (NC .EQ. 1 .OR.  MOD(NC+1,3)  .EQ. 0)  GO TO 270
C        INTERPOLATION TO FIND DVS
      DVS=DVSA+(DVSB-DVSA)/(DELVB-DELVA)*(DELV-DELVA)
      GO TO 280
270   PJ=PA+(DELV-DELVA)/(VVA*(1./(PA+SDH/2.)+A1/2.)-TEMP1/(EQSTCM*PA))
      IF (PJ .LT. 0. .OR. PA .GE. 0.) GO TO 279
      PJ=PA+EQSTCM*(VVA-DELV)/VSO
      IF (PJ .LT. 0.) PJ=AMAX1(PJ,PA)/2.
279   PJ=PA+SIGN(AMIN1(ABS(PJ-PA),DPJ),DELVA-DELV)
      DVS=TEMP1/(1.+PJ/EQSTCM)-VSO
      IF (NC .EQ. 1) GO TO 290
280   IF (ABS(DELVA-DELV) .GT. ABS(DELVB-DELV)) GO TO 200
290   DELVB=DELVA   $   DVSB=DVSA   $    GO TO 200
C
C        ENDING ROUTINE
300   CONTINUE
      NT=0.
      R=R+DR
      DO 320 NA=1,NANG
      IF (NA .LT. NANG) GO TO 307
      STHW=STTE+PJ  $   GO TO 310
307   STHW=PJ+(SXXE+SYYE)/2.+(SXXE-SYYE)/2.*(COS2TH(NA)*COSR-SIN2TH(NA)*
     1   SINR)+TXYE*(SIN2TH(NA)*COSR+COS2TH(NA)*SINR)
310   SAVG=(STH(NA)+STHW)/2.
      SCN=SAVG-TSR(M,9)*(PSO+PJ)/2.-TSR(M,5)
      DN=0.
      IF (SCN .LT. 0.) DN=TSR(M,4)*EXP(SCN/TSR(M,6))*DT*FNUC(NA)
      CNO=CN(KS,JS,NA)
      CN(KS,JS,NA)=CN(KS,JS,NA)*DH/DOLD+DN
      IF (CN(KS,JS,NA) .EQ. 0.) GO TO 320
      CL(KS,JS,NA)=(CNO*CL(KS,JS,NA)*EXP(A1*AMIN1(SAVG-TSR(M,2),0.))+
     1  DN*TSR(M,3))/CN(KS,JS,NA)
      NT=NT+CN(KS,JS,NA)
320   CONTINUE
      NM=VVA*DH
      PSO=PJ
      IF (NM .GT. 0.6) GO TO 400
C     *****      EVALUATE AVERAGE GROSS PRESSURE FROM SOLID PRESSURE  ***
      PJ=PJ*(VSO+DVS)*DH
      SXXEN=SXXE
      SYYEN=SYYE
      STTEN=STTE
      TXYEN=TXYE
      P=PJ
      Y=YT
      TXXE=PJ+SXXE
      IF (IPRBFR(1) .EQ. 1) PRINT 1255,NN,NL,PSO,PJ,TXXE,NM
1255  FORMAT(10H CONVERGED,5X,*NN=*I4,*,NL=*I4,*, PSO=*E10.3,*, PJ=*E10.
```

```
     13,*, TXX=*E10.3,*, NM=*E10.3)
C        **********
C        END OF SUBCYCLING LOOP
C        **********
      VVO=VVA    $    VSO=VSO+DVS
380   DOLD=DH
      E=EEST+(PO-PJ)*DVO/2.
      ROT(KS,JS)=R
      RETURN
C
C        END WITH SEPARATION
400   SXXE=SYYE=SXYE=TXYE=P=0.
      Y=YT   $   NM=-ABS(NM)
      RETURN
C
C ***    PROVISION FOR ABORT IN CASE OF ITERATION FAILURE
450   NTRY=NTRY+1
      IF (NTRY .GE. 5) GO TO 460
      DV=VO/RHOS-1./DOLD
      NLOOP=MAX1(3.,-4.*2.**NTRY*DV*EQSTCM/VSO/TSR(M,5)+0.5,2.*NLOOP)
      NTRI(KS,JS)=NTRY+100*NLOOP
      GO TO 100
460   PRINT 1600,NN,KS,JS,SDH,P,DV,DELVA,DELVB,DELV,DVO,VO
      IF (NTRY .EQ. 5) STOP 22
      NT=0.
      R=R+DR
      DO 620 NA=1,NANG
      IF (NA .LT. NANG) GO TO 607
      STHW=STTE+PJ $ GO TO 610
607   STHW=PJ+(SXXE+SYYE)/2.+(SXXE-SYYE)/2.*(COS2TH(NA)*COSR-SIN2TH(NA)*
     1     SINR)+TXYE*(SIN2TH(NA)*COSR+COS2TH(NA)*SINR)
610   SAVG=(STH(NA)+STHW)/2.
      SCN=SAVG-TSR(M,9)*(PSO+PJ)/2.-TSR(M,5)
      DN=0.
      IF (SCN .LT. 0.) DN=TSR(M,4)*EXP(SCN/TSR(M,6))*DT*FNUC(NA)
      CNO=CN(KS,JS,NA)
      CN(KS,JS,NA)=CN(KS,JS,NA)*DH/DOLD+DN
      IF (CN(KS,JS,NA) .EQ. 0.) GO TO 620
      CL(KS,JS,NA)=(CNO*CL(KS,JS,NA)*EXP(A)*AMIN1(SAVG-TSR(M,2),0.))+
     1     DN*TSR(M,3))/CN(KS,JS,NA)
      NT=NT+CN(KS,JS,NA)
620   CONTINUE
      NM=VVA*DH
      IF (NM .GT. 0.6) GO TO 400
      PJ=PJ*(VSO+DVS)*DH
      SXXFN=SXXE
      SYYEN=SYYE
      STTEN=STTE
      TXYEN=TXYE
      P=PJ
      Y=YT
      VVO=VVA    $    VSO=VSO+DVS
      DOLD=DH
      E=EEST+(PO-PJ)*DVO/2.
      ROT(KS,JS)=R
      RETURN
C
C        FINAL PRINTOUT
C
```

```
500    IZERO=1
       PRINT 1511,((NTRI(K,J),J=1,11),K=1,11)
       DO 530 K=1,11
       DO 530 J=1,11
530    NTRI(K,J)=0
       DO 521 K=1,11
       DO 520 J=1,11
       IF (CN(K,J,1) .EQ. 0.) GO TO 520
       IF (IZERO .EQ. 1) PRINT 1500
       IZERO=2
       CNSUM=CRIT2=CRIT3=CRIT4=0.
       DO 510 NA=1,NANG
       CL3(NA)=CL(K,J,NA)**(1./3.)
       CRIT2=CRIT2+CN(K,J,NA)*CL3(NA)**2
       CNSUM=CNSUM+CN(K,J,NA)
510    CRIT3=CRIT3+CN(K,J,NA)*CL(K,J,NA)
       CRIT2=3.1416*CRIT2
       RAD=(CRIT3/CNSUM)**(1./3.)
       PRINT 1510,(CL3(I),I=1,5),RAD,CRIT2,K,J,(CN(K,J,I),I=1,5),CNSUM,
      1   ROT(K,J)
520    CONTINUE
521    CONTINUE
       RETURN
1500   FORMAT(1H0,*  LISTING OF CRACK LENGTH AND NUMBER FOR EVERY *,
      1   *FRACTURING CELL*/)
1510   FORMAT (* CELL   CL = *4E10.3,2X,E10.3,*  CL-AVG = *E10.3,
      1  14H  PI*N*R**2 = ,E10.3/2I3*  CN = *4E10.3,2X,E10.3,*  CN-TOT =
      2*E10.3,14H        ROT = ,E10.3/)
1511   FORMAT(* *,10X,*   BFRACT ITERATIONS--NTRY+100,NLC[illegible]*,/,10X,*   K-
      1ROWS AND J-COLS*,//,11(11I10/),/,*1*)
1600   FORMAT (* ITERATION FAILURE IN BFRACT, N=*I5,*, K=*I3,*, J=*I3,
      1   5E12.3,/,5X,3E12.3)
       END BFRACT
```

Appendix C

CALCULATION OF VOID GROWTH UNDER HIGH SHEAR

The calculations of this appendix were made to guide in constructing stress-strain relations for material containing voids for cases where the material is subjected to high shear strains. The material was idealized as an elastic-viscous-plastic material, initially containing a uniform spacing of spherical voids. The "typical" element used in the computations was a cylinder with height equal to the diameter and containing one spherical void at its center as shown in Figure C-1. The calculations simulated a high speed extrusion that could occur in 10 to 100 nsec. The planar boundaries were moved outward to simulate tensile straining on the material. The cylindrical boundaries were moved inward at half the velocity of the planar boundaries to produce a constant volume, high-shear-strain loading on the material.

The computations were conducted with a computer program termed VOID, a special purpose, finite-difference, two-dimensional wave propagation code described in Reference 3. In the calculations, the motion of the boundaries caused waves to propagate through the body of the material. By use of a high coefficient of artificial viscosity, the wave amplitudes were minimized so they did not interfere with the interpretation of the steady-state results.

The quantities of interest for determining stress-strain relations for fracturing material are the pressure, deviator stresses, gross specific volume, void volume, and gross shear strain. The stress quantities were computed as averages based on the total forces on the planar and cylindrical surfaces. The growth rate of the void was derived from the computed history of void volume. Because only a shear strain was imposed, the pressure remained small, making interpretation of pressure volume-relations uncertain. However, the void growth rate does

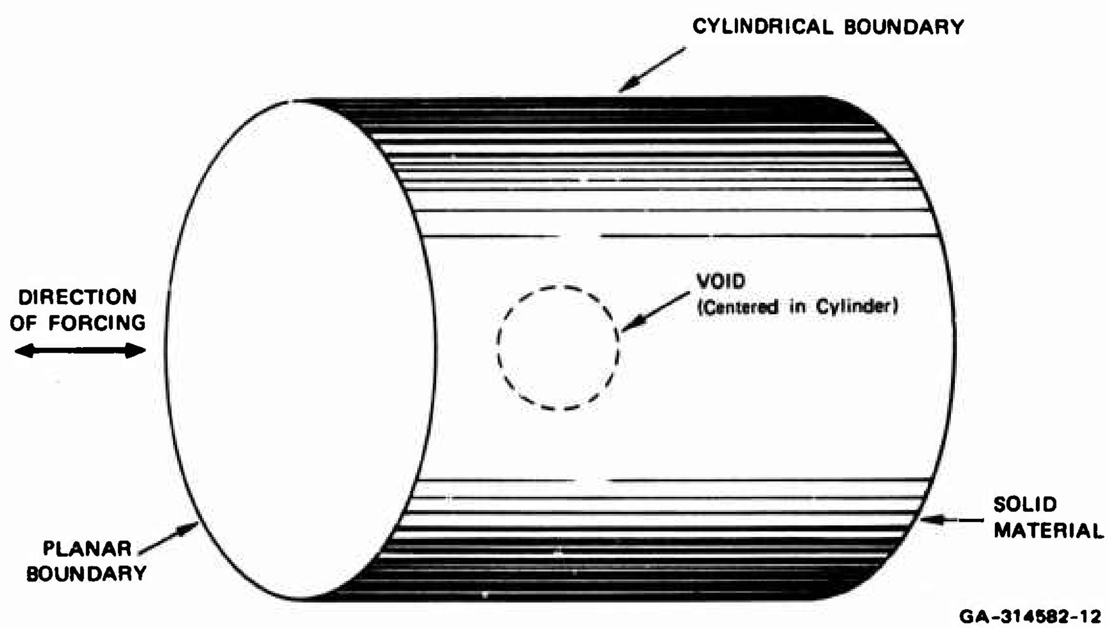

FIGURE C-1 GEOMETRY OF CYLINDER OF SOLID MATERIAL CONTAINING A SPHERICAL VOID TO SIMULATE FRACTURE BY VOID GROWTH appear to follow the rule

$$\dot{R} = \frac{P - P_o}{4\eta} R \tag{C-1}$$

where R = average void radius

P = pressure

P_o = a threshold pressure

η = the material viscosity used in the stress relaxation model for the material.

Hence the growth rate is the same under high-shear-strain loading as for spherical or one-dimensional loading.

The deviator stress-strain relation was also studied. As in the one-dimensional calculations,[3] some of the results fit the form we expected, which is, in one dimension

$$\dot{\sigma}' = \frac{4}{3} G(1 - 4V_v \rho) \frac{\dot{V}}{V} - \frac{\sigma' - 2/3Y}{T} \tag{C-2}$$

where σ' = deviator stress

G = shear modulus for the solid material

V_v = specific volume of the void

ρ = density

V = gross specific volume

Y = yield strength

T = a time constant.

Some of the results showed a long rise time corresponding to a much smaller modulus than G. These latter results may have been caused by the effect of waves on the results. Because we could not interpret these results, we chose to use Eq. (C-2) for deviator stress until a more complete study could be conducted of deviator stress.

Appendix D

BALLISTIC EXPERIMENTS ON 1145 ALUMINUM AND ARMCO IRON

As an aid to the code development effort, long rod ballistic impact experiments were performed on two materials whose dynamic fracture behavior under one-dimensional strain is well-known. We performed 4 experiments on 10 x 10 cm plates of 1.27-cm-thick 1145 aluminum and 14 experiments on similar specimens of Armco iron, using the testing facility shown in Figure 14 of Section III.C. The dynamic fracture parameters for both materials under uniaxial strain had been determined in previous work. Our goal was to count and measure the fracture damage in these specimens and then eventually compare the results with the predictions of the evolving two-dimensional fracture model.

Table D-I summarizes the results. For the experiments on armor steel described in Section III.C, the projectiles were right cylinders 1.03 cm in diamter by 2.03 cm long, made of drill rod and fitted into Lexan polycarbonate sabots. For the 1145 aluminum experiments, the projectiles were in the as-received spherodized condition at a hardness of Rockwell B95. For the Armco iron experiments, the projectiles were heat treated to Rockwell C35. The projectiles were accelerated to different velocities to produce a range in the extent of fracture damage in the targets.

Work on 1145 aluminum was discontinued after four experiments, since it became apparent that no voids or cracks could be produced under these conditions. The penetration mechanism for this soft aluminum alloy was one of pure plastic plugging, although spherical ductile voids were previously found to develop under uniaxial strain conditions. The photomicrograph in Figure D-1 of a polished cross section taken through the partially penetrated Specimen No. 3 shows the intense plastic shear deformation.

Preceding page blank

Table D-I

SUMMARY OF BALLISTIC TESTS

Experiment No.	Material	Projectile Velocity (ft/sec)	Remarks
1	1145 Al	1900*	Full penetration; no voids or cracks observed on polished cross sections.
2	1145 Al	555	Partial penetration; no voids or cracks observed on polished cross sections.
3	1145 Al	500	Partial penetration; (see Figure D-1) no voids or cracks observed on polished cross sections.
4	1145 Al	200	Partial penetration; no voids or cracks observed on polished cross sections.
5	Armco Fe	730	Partial penetration; no voids or cracks observed on polished cross sections.
6	Armco Fe	850*	Partial penetration; no voids or cracks observed on polished cross sections.
7	Armco Fe	950*	Partial penetration; no voids or cracks observed on polished cross sections.
8	Armco Fe	1115	Partial penetration; incipient fracture damage.
9	Armco Fe	1300*	Partial penetration; incipient fracture damage.
10	Armco Fe	1300	See Figures D-2 and D-3.
11	Armco Fe	1640	See Figures D-2 and D-3.
12	Armco Fe	1630	Partial penetration; incipient back surface fragmentation.
13	Armco Fe	1890	See Figures D-2 and D-3.
14	Armco Fe	2000*	Partial penetration; incipient back surface fragmentation.
15	Armco Fe	2130	Still only partial penetration. See Figures D-2 and D-4.
36	Armco Fe	3300	Penetration; gross back surface fragmentation, see Figure D-2.
37	Armco Fe	2900	Penetration; back surface petalling, see Figure D-2.
38	Armco Fe	2650	No penetration; back surface heavily damaged, see Figure D-2.

* No velocity record was obtained. Velocities are estimated values.

Note: All shots performed on rolled plate 4 inches square by 1/2-inch thick using 0.8-inch long x 0.4-inch diameter cylindrical projectiles from drill rod, heat treated to a hardness of RC35--except for shots on 1145 Al in which projectile hardness was Rockwell B95.

MP-2024-2

FIGURE D-1 POLISHED CROSS SECTION OF 1145 ALUMINUM PARTIALLY PENETRATED BY A ROD-LIKE PROJECTILE

Fracture damage did accompany projectile penetration in Armco iron at velocities of about 1100 ft/sec and above, as could be readily observed on the rear surfaces, Figure D-2. Full penetration did not occur at velocities up to 2130 ft/sec.

Examination of polished sections with an optical microscope showed that, as in the uniaxial strain situation, the damage was in the form of planar microcracks, as shown in Figure D-3. The cracks lay nominally in a band about 2 mm from the rear surface and roughly parallel to it. They coalesced most strongly in the material directly in the path of the projectile, and at sufficiently high velocities resulted in rear surface spallation.

To obtain the necessary experimental information for eventual comparison with the predictions of the two-dimensional dynamic fracture model, we assessed quantitatively the fracture damage in the specimens. The procedure entailed counting and measuring the microcrack traces on enlarged photomicrographs of polished sections, as shown in Figure D-4. A statistical transformation may be applied to these data to obtain the actual crack size distributions per unit volume. The crack trace counting and measuring operation is facilitated by a large area record reader, and the statistical transformation is performed by a computer code. The counting and measuring was carried out for the above Armco iron specimens, but the statistical transformation to volume distribution was not accomplished. In any future work it is recommended that this be done to provide data for comparison with HEMP code predictions based on the fracture model developed in this program.

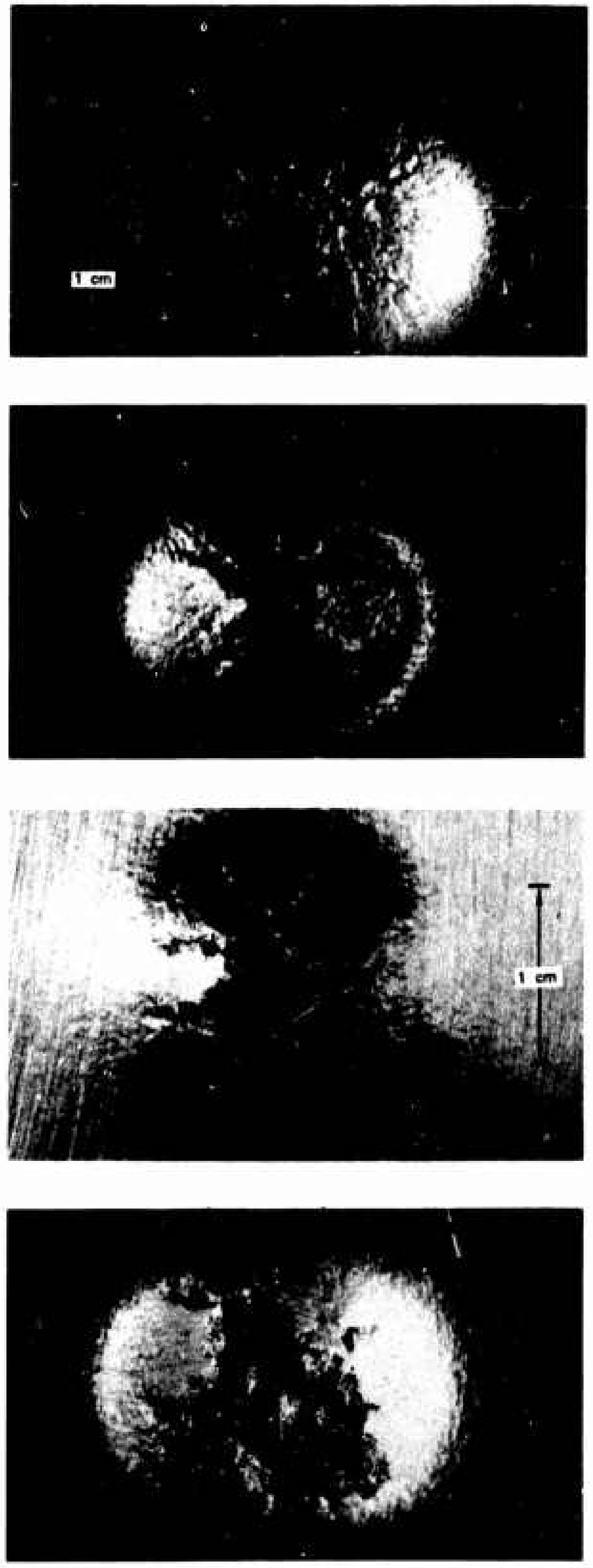

1300 ft/sec

1640 ft/sec

1890 ft/sec

2130 ft/sec

MP-2024-3

FIGURE D-2 BACK SURFACE FRACTURE IN ARMCO IRON SPECIMENS AT VARIOUS PROJECTILE VELOCITIES

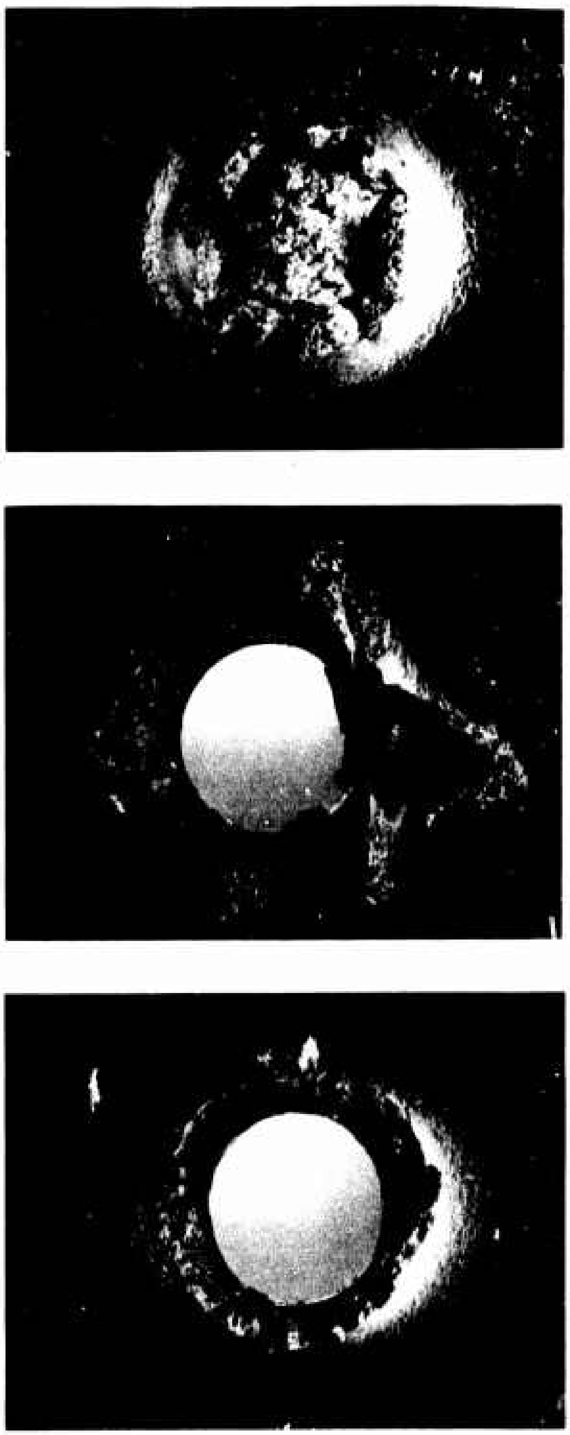

2650 ft/sec

2900 ft/sec

3300 ft/sec

MP-2024-3A

FIGURE D-2 BACK SURFACE FRACTURE IN ARMCO IRON SPECIMENS AT VARIOUS PROJECTILE VELOCITIES (Concluded)

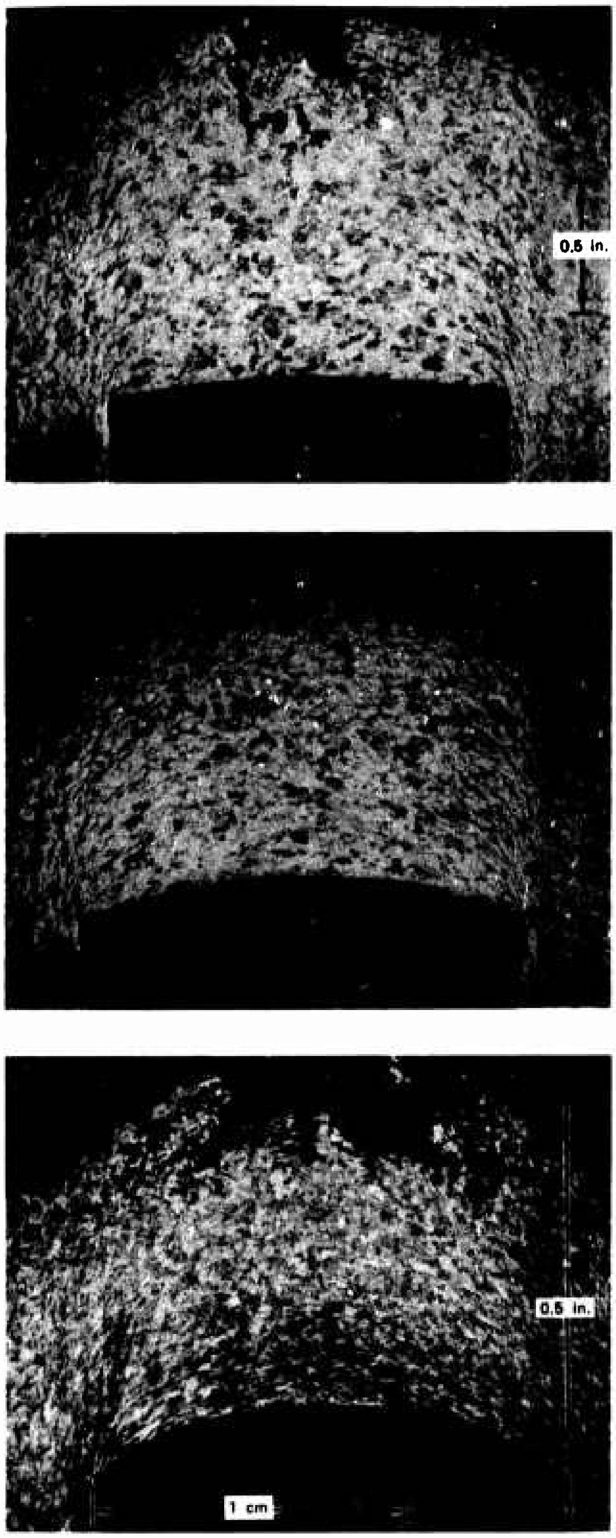

1300 ft/sec

1640 ft/sec

1890 ft/sec

MP-2024-4

FIGURE D-3 POLISHED AND ETCHED CROSS SECTIONS OF ARMCO IRON SPECIMENS SHOWING FRACTURE DAMAGE INDUCED BY PROJECTILE IMPACT

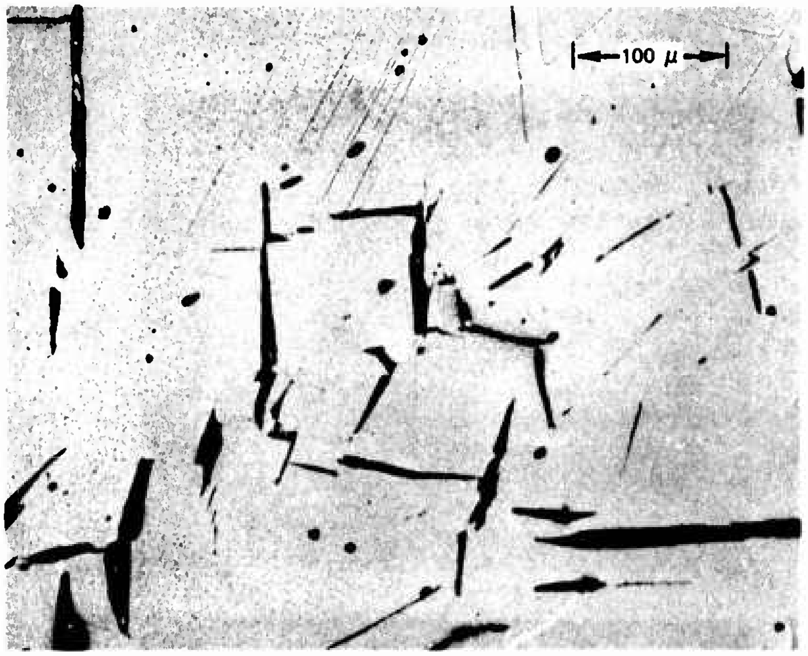

MP-2024-5

FIGURE D-4 HIGH MAGNIFICATION VIEW OF MICROCRACK TRACES ON AN UNETCHED POLISHED SECTION THROUGH ARMCO IRON SPECIMEN NUMBER 15

Appendix E

IMPROVED HOMOGENEOUS STEEL ARMOR

An improved homogeneous steel (IHS) armor can be made by unidirectionally solidifying and homogenizing steel castings.[16] This procedure results in a cleaner steel, free from large inclusions and having a lower content of detrimental impurity elements such as sulfur, oxygen, and phosphorus. In addition, the procedure provides a preferred texture and a fine homogeneous dispersion of included particles. These microstructural features are thought responsible for the excellent high strength ductility and superior ballistic impact properties of the material.

The laboratory method for making IHS consists of pouring the steel under vacuum into a mold cavity on a thick copper chill block. The feasibility of large-scale production by the commercial electroslag remelt (ESR) technique is being actively investigated by AMMRC, and the results are encouraging.

Because of the attractive properties of the improved armor steel and the promise of the ESR process as a cost-effective manufacturing method, some preliminary investigations were carried out on IHS in this program. The microstructure was examined, quasistatic tensile properties in the short transverse (through-the-plate-thickness) direction were determined, the fracture surfaces were examined, and the region near the hole produced by a ballistic round was examined.

Material

The steel was manufactured by U.S. Steel Corporation[17] by the unidirectional solidification technique in 18 x 13½ x 18 inch molds on a thick copper chill block. The steel had the following approximate chemical composition (wt%): 0.52 C, 0.70 Mn, 0.25 Si, 1.20 Ni, 0.75 Cr, 0.50 Mo, 0.025 Al, < 0.003 P, 0.005 S, and < 0.009 N.

Melting, alloying, and pouring were done under vacuum. The vacuum melting was done in a 500-pound induction furnace; the pouring temperature was maintained at about 2900°F. Homogenization took place in a commercial high-temperature heat treating furnace at a pressure of 1 micron and a temperature of 2400°F for 64 hours. After furnace cooling to 1000°F and then air cooling, the casting was cut into four slabs and hot cross-rolled to half-inch plates. The plates were then heat treated to about RC 60 by heating to 1500°F for 1/2 hours, oil quenching, and immediately tempering at 250°F for 1 hour.

Microstructural Observations

Polished and etched surfaces in three mutually perpendicular planes of a plate of undirectionally solidified and homogenized steel were examined with the optical microscope. Most notable were the fineness and homogeneity of the microstructure, the absence of large inclusions, and the lack of banding. Figure E-1 shows micrographs of the IHS armor and, for comparison, the XAR30 armor. Note the coarser structure and the large inclusions in the XAR30 material.

Tensile Property Measurements

Tensile properties in the short transverse direction (through the plate thickness) were determined by spark machining small cylindrical blanks about 6.35 mm in diameter and 12.7 mm long from the armor plate, grinding the central sections of the blanks to about 3.18 mm to obtain a typical dumbbell shaped specimen with a gage length of about 5.08 mm, and then pulling the specimens in a tensile testing machine at a constant crosshead speed of 0.5 mm/minute. Triplicate specimens yielded extremely reproducible load displacment records, shown in Figure E-2 which were analyzed to obtain the short transverse tensile properties given in Table E-I.* The curves from similar tests for conventional rolled

* The results for similar specimens tested at a 100-fold faster testing speed (50 mm/minute) were essentially identical and show the low strain rate sensitivity of the steels in this range.

(a) IMPROVED HOMOGENEOUS STEEL

(b) XAR30 ARMOR STEEL

MP-2024-29

FIGURE E-1 COMPARISON OF CROSS SECTIONS OF IMPROVED HOMOGENEOUS STEEL ARMOR AND OF XAR30 ARMOR

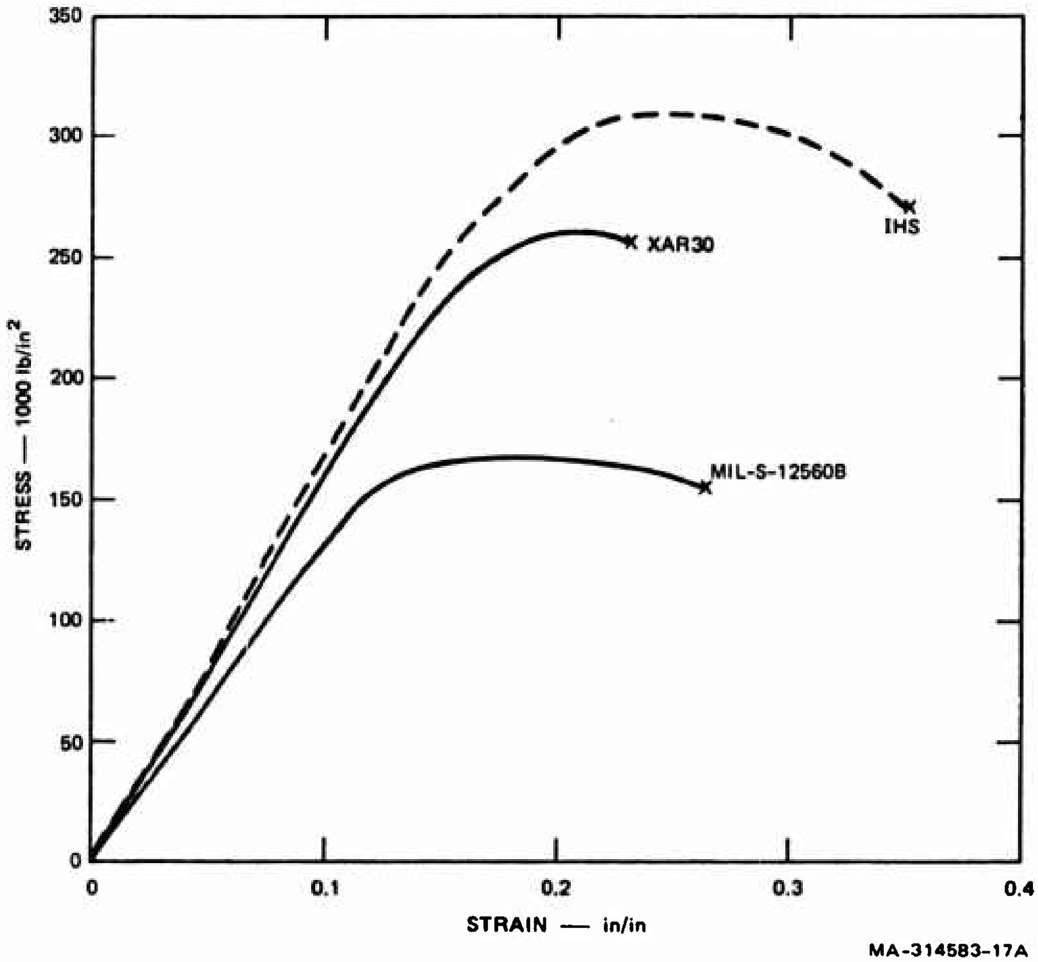

FIGURE E-2 STRESS-STRAIN CURVES FROM SHORT TRANSVERSE TENSILE TESTS OF THREE ARMOR STEELS

Table E-1

RESULTS OF QUASISTATIC TENSILE TESTS
OF THREE ARMOR STEELS TESTED NORMAL TO THE ROLLING PLANE

Specimen Number	0.2% Yield Strength (ksi)	Ultimate Tensile Strength (ksi)	Total Strain at Fracture (%)	Elongation (%)	Reduction in Area at Fracture (%)	Toughness (in.-kips/in.^{3})
XAR30	210	261	22.5	8.5	12.2	37.3
XAR30	206	262	24.3	12.5	13.8	39.0
XAR30	217	260	22.3	9.5	11.4	34.6
Average	211 ± 6	261 ± 1	23.0 ± 1.3	10.0 ± 2.5	12.5 ± 1.2	36.9 ± 2.3
XAR30	224	259	22.0	9.5	13.8	37.6
12560B-1	150	163	27.7	22.0	36	32.9
12560B-2	150	163	25.5	23.0	31	31.3
12560B-3	152	163	21.4	16.0	20	24.3
Average	151 ± 1	163 ± 0	24.9 ± 3.5	20.4 ± 4.4	29 ± 9	29.5 ± 5.2
12560B-4*	150	164	20.0	14.5	23	24.3
IHS-1	226	309	36.2	21.0	31	77.3
IHS-2	250	309	34.8	20.0	33	74.5
IHS-3	248	309	32.6	17.5	29	69.3
Average	241 ± 15	309 ± 0	34.5 ± 1.9	19.5 ± 2.0	31 ± 2	73.6 ± 4.3
IHS-4*	260	306	34.0	21.5	33	71.0

For All Specimens: Gage length = 0.200 in. Total length = 0.485 in.
Initial diameter = 0.125 in. Cross-head speed = 0.02 in./min (2.0 in/min for *)
Initial area = 0.0123 in.^{2} Strain rate = 0.00167 in./in.-sec (0.167 in./in.-sec for *)

homogeneous armor steels are included for comparison. These properties are of particular interest since the dynamic loads in this work are applied normal to the plane of the plate. The short transverse properties for MIL-S-12560B armor steel have been shown to differ significantly from the properties in perpendicular directions.[8]

Fractography

The IHS armor tensile specimens fractured in a classical cup-cone manner after considerable necking; the fracture appearance of the XAR30 and MIL-S-12560B specimens was of the 45^{o} shear type, as shown in Figure E-3. In the MIL-S-12560B steel large cracks, such as shown in Figure E-3(c), were often observed on the specimen sides. Figure E-4 is a high magnification scanning electron micrograph of the central region of the cup-cone of a specimen of improved homogeneous steel, showing the fineness of the dimple structure. The small spherical particles at the centers of the dimples were analyzed by nondispersive X-rays as aluminum, and are thus thought to be aluminum oxide. This fine uniform dispersion of these particles probably contributes to the excellent strength and ductility characteristics.

A plate of IHS armor that had been tested ballistically at AMMRC was sent to SRI for examination. We sectioned the plate through the center of the hole made by the ballistic round and polished this surface for observation with an optical microscope. Figure E-5(a) shows the fracture damage that occurred during projectile penetration. It is important to note that the cracks are rather randomly oriented and thus can join up to isolate fragments, a process that had indeed occurred at a location included in the figure. Etching revealed dense networks

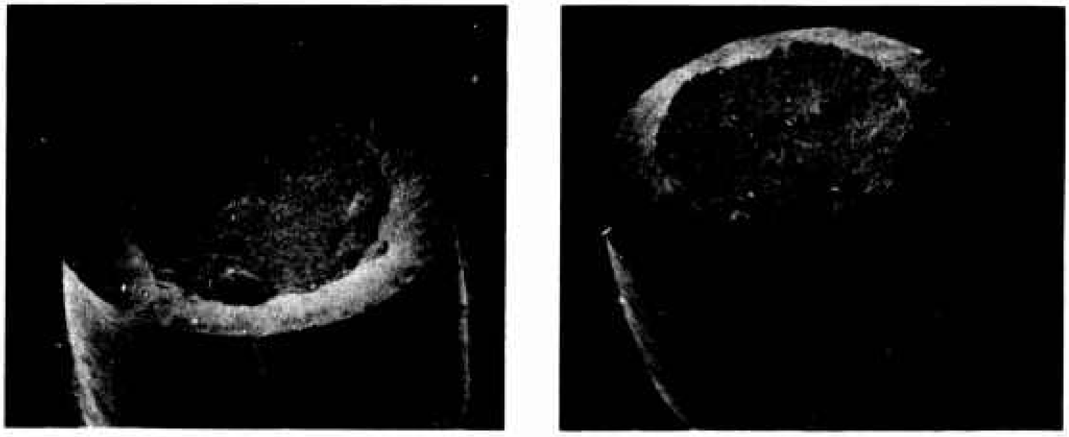

(a) IMPROVED HOMOGENEOUS STEEL ARMOR

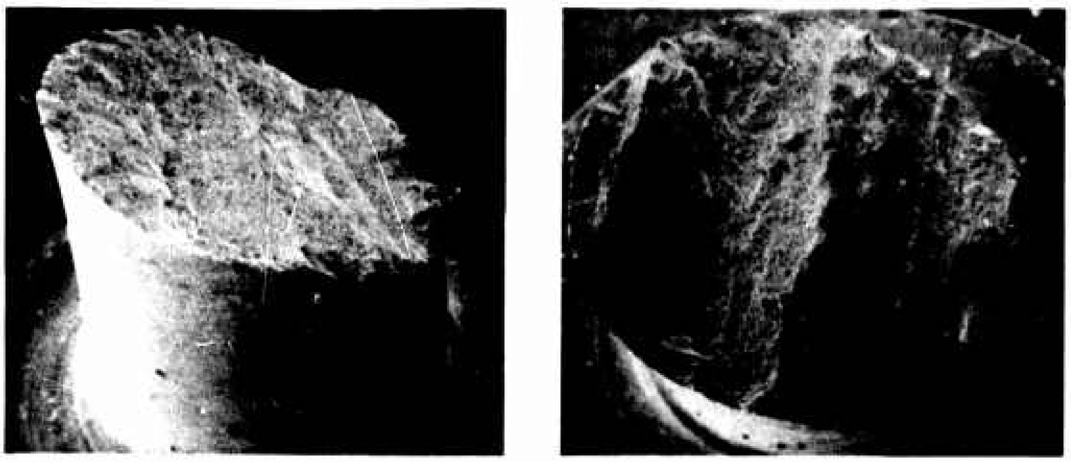

(b) XAR30 STEEL ARMOR

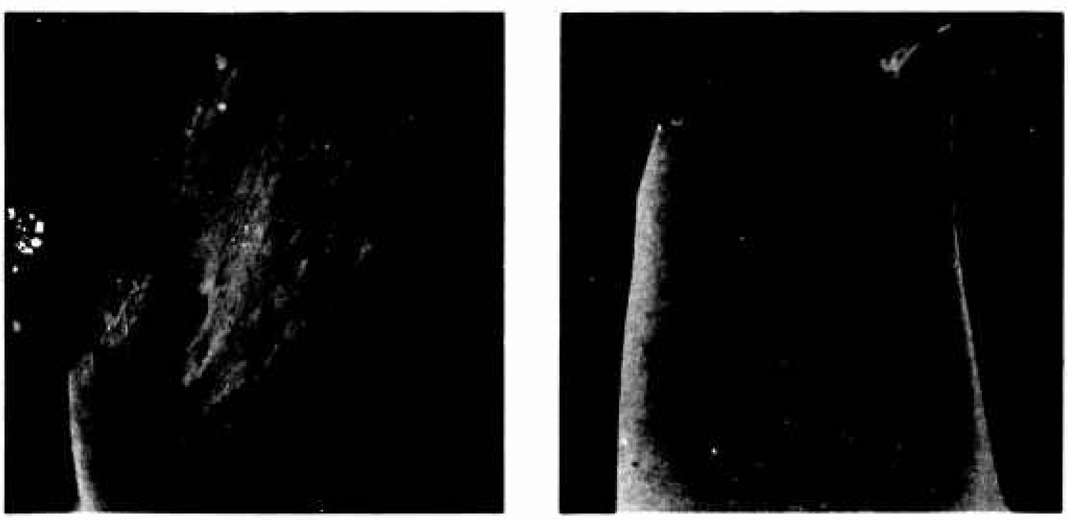

(c) MIL-S-12560B STEEL ARMOR

MP-2024-30

FIGURE E-3 APPEARANCE OF FRACTURED ENDS OF SHORT TRANSVERSE TENSILE SPECIMENS OF THREE ARMOR STEELS

FIGURE E-4 SCANNING ELECTRON MICROGRAPH OF CENTRAL REGION OF CUP-CONE FRACTURE SURFACE OF IMPROVED HOMOGENEOUS STEEL TENSILE SPECIMEN

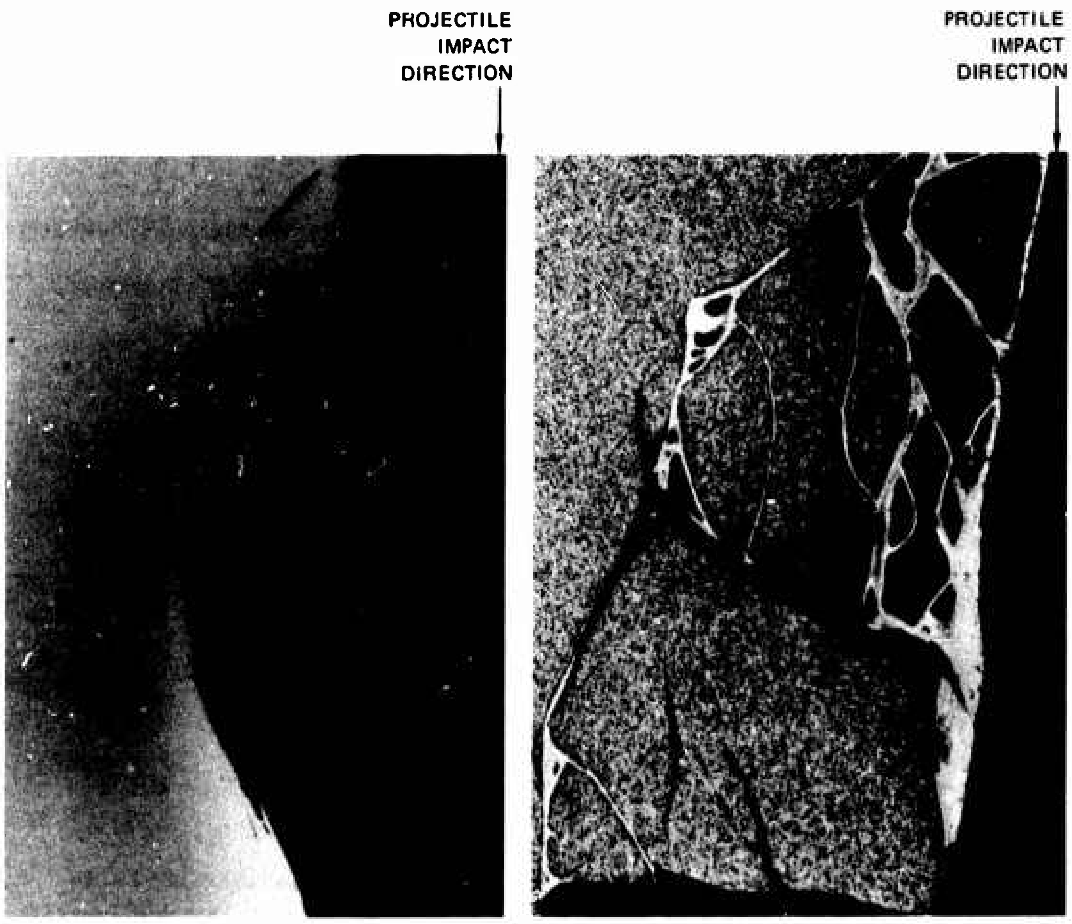

(a) POLISHED SECTION THROUGH PROJECTILE HOLE

(b) ETCHED CLOSE-UP VIEW OF (a)

MP-2024-6A

FIGURE E-5 PLANAR MICROCRACKS AND ADIABATIC SHEAR ZONES NEAR THE PLUGGED REGION IN IMPROVED HOMOGENEOUS STEEL ARMOR of adiabatic shear bands.* Figure E-5(b) is a closeup view of Figure E-5(a), and shows that many of the cracks lie within the shear bands. Figure E-5 demonstrates the important role of adiabatic shear in the penetration process for IHS. The probable time sequence of events during penetration is as follows:

(1) Under ballistic impact, a network of adiabatic shear bands forms in the armor plate.

(2) The narrow shear bands are preferred fracture sites, and planar microcracks nucleate and grow within them.

(3) The cracks join up with one another and with the surfaces of the armor plate, freeing the plug and a number of fragments.

---

*Adiabatic shear bands are narrow regions of highly localized large plastic shear strains. The heating accompanying the shear deformation may increase the temperature to where solid phase transformations or even melting occurs. Very rapid quenching of this material follows because the large volume of adjacent material in intimate contact with the narrow band conducts the heat away at high rates. In the present instance a transformation to austenite followed by another rapid transformation to martensite probably occurred. The white etching response in 5% nital is consistent with the existence of martensite.

Appendix F

THE MICROMECHANISM OF DYNAMIC FRACTURE IN ROLLED ARMOR STEEL

Observations of polished cross sections of shock damaged specimens of ferrous materials indicate two distinctive fracture morphologies. Rolled homogeneous XAR30 armor steel for example, exhibits a relatively small number of large parallel crack-like artifacts (as shown earlier in Figure 6), whereas Armco iron[3] acquires many more microcracks, which are generally much shorter, more randomly oriented, and more slit-like, as shown in Figure F-1.

The observerations in Armco iron are attributable to cleavage-type fracture of individual grains. The grains and hence the cleavage planes are nearly randomly oriented, which explains the observed random micro-crack orientation and also the limited size of the microcracks--the latter because large deviations from crystallographic match-up between grains makes it difficult for a cleavage crack to form in an adjacent grain. Thus most microcracks in Armco iron arrest at grain boundaries.

But whereas the fracture morphology in Armco iron is controlled by the presence of weak cleavage planes, the morphology of rolled steels reflects the weak planes of the rolling direction. Examination of the large planar fractures in XAR30 armor steel at high magnification reveals that each large fracture comprises a large number of microfractures having a spherical appearance. It appears that the microfractures nucleate in a plane, grow spherically, and coalesce with one another to result in the observed planar macrofractures.

Full spall or the formation of a continuous macrofracture within a specimen occurs when adjacent planar fractures coalesce. The micrograph in Figure F-2 shows two parallel but nonplanar fractures in the process of coalescing. A profusion of tiny microfractures has formed in the path of incipient coalescence under the action of high shear stresses,

FIGURE F-1 POLISHED CROSS SECTION IN SHOCK LOADED ARMCO IRON REVEALING INTERNAL CLEAVAGE CRACKS

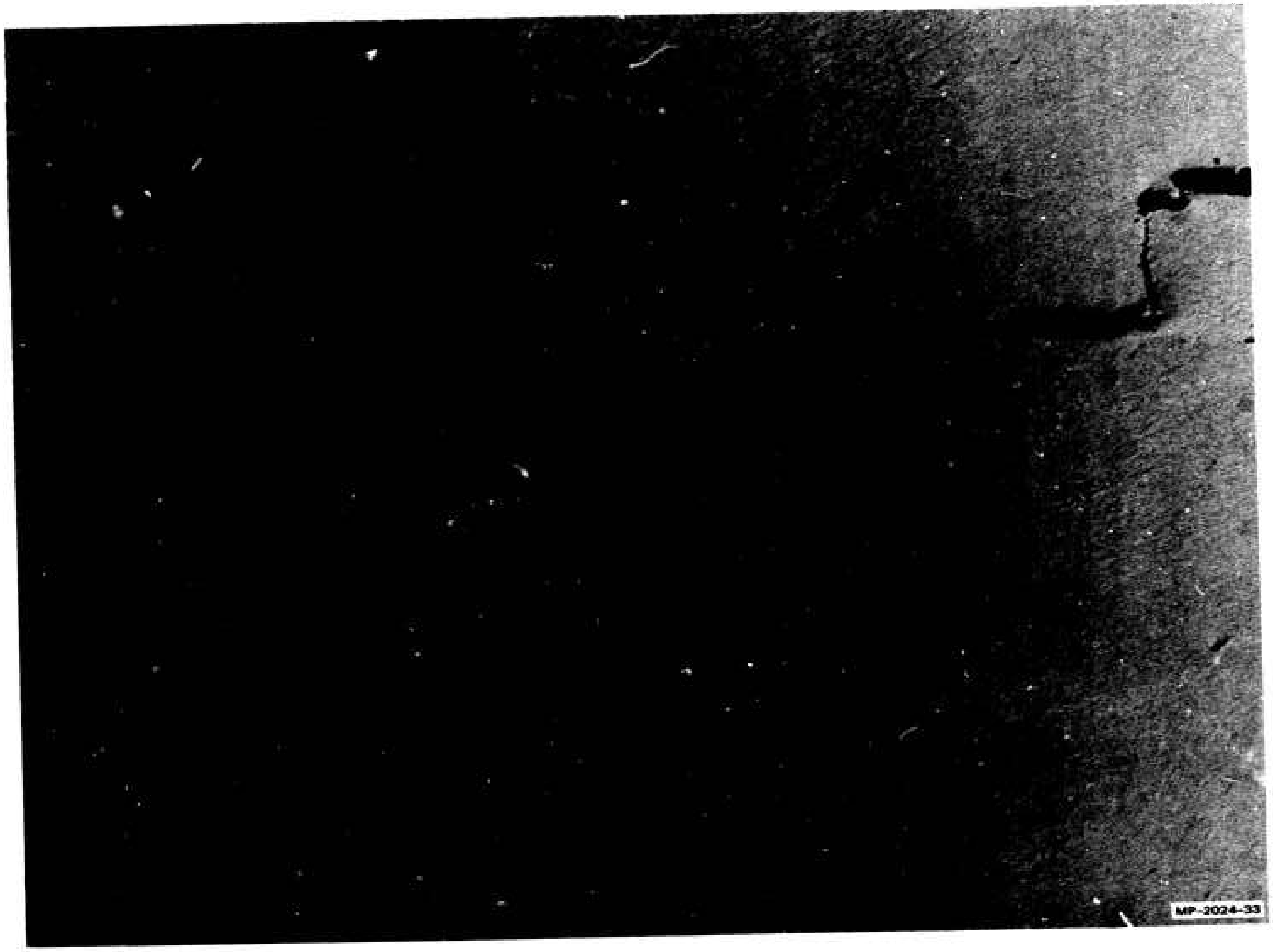

FIGURE F-2 POLISHED CROSS SECTION IN XAR30 ARMOR STEEL SHOWING INCIPIENT COALESENCE OF TWO PLANAR FRACTURES as in the formation of the planar fractures, these microfractures nucleate, grow, and join up until a continuous fracture connects the two planes.

This process is depicted schematically in Figure F-3.

The micrographs of shock loaded XAR30 armor steel in Figure F-4 clearly show that inclusions are involved in the nucleation of fracture. This leads us to speculate that the improved ballistic performance of unidirectionally solidified or electroslag remelted steel is connected with its lower inclusion content.

The view in Figure F-4 is slightly etched to reveal the grey sulfide inclusions but not the grain structure. The inclusions, whose elongated form and biased orientation result from the rolling process, have fractured in a brittle manner. As these cracks attempt to extend into the more ductile steel, their morphology becomes more equiaxed. Figure F-4(b) is a more heavily etched area of the specimen, showing a large planar fracture that apparently originated at the broken inclusion, extended by coalescence of more ductile microfractures, and finally coalesced with a parallel but nonplanar fracture by a similar process.

The apparent nests of voids observable at high magnifications may not be caused by the same dislocation mechanisms responsible for void formation in aluminum, copper, and tantalum, such as described by Stevens et al.[18,19] Rather, as implied from dynamic fracture work in Armco iron, the "voids" may nucleate as planar microcracks on cleavage planes, which upon reaching the grain boundaires, arrest and begin to widen (Figure F-5). The result is a void-like microfracture, which attained its morphology by extensive plastic flow at a planar crack front instead of by maintaining a pseudo-spherical morphology during its growth phase.

(1) NUCLEATION OF ROWS OF VOIDS.

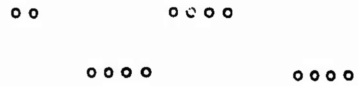

(2) SPHERICAL EXPANSION OF THE VOIDS AND COALESCENCE OF THE ROW. OTHER ROWS OF VOIDS ARE NUCLEATED ON EITHER SIDE OF MAIN DAMAGED ZONE.

(3) JOINING UP OF THE ROWS BY SHEAR CRACKS, WHICH ALSO FORM BY NUCLEATION, GROWTH, AND COALESCENCE OF MICROVOIDS.

(4) FURTHER WIDENING AND COALESCENCE.

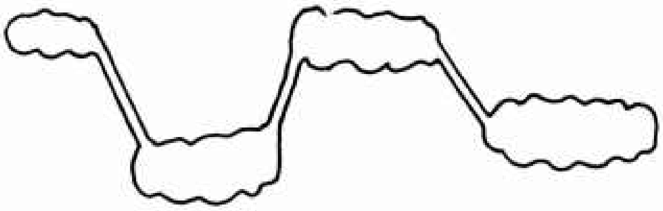

THE FRACTURE DAMAGE OF STAGE 2 APPEARS MACROSCOPICALLY TO BE PLANAR MICROCRACKS. FRACTURE MODE IN ACTUALITY IS A DUCTILE, ENERGY-ABSORBING MODE. SEM WORK SHOWS NESTS OF VOIDS CONNECTED BY SHEAR CRACKS LYING AT STEEP ANGLES.

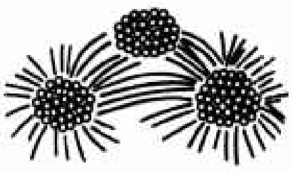

MANY INCLUSIONS; MANY HAVE CRACKS PRODUCED EITHER DURING ROLLING OR DURING IMPACT. TWO MAIN TYPES:

(a) GREY LENSES (STRINGERS), PROBABLY SULFIDE

(b) ORANGE SQUARES □

MA-2024-34

FIGURE F-3 PROPOSED DYNAMIC FRACTURE PROCESS IN ROLLED ARMOR STEEL

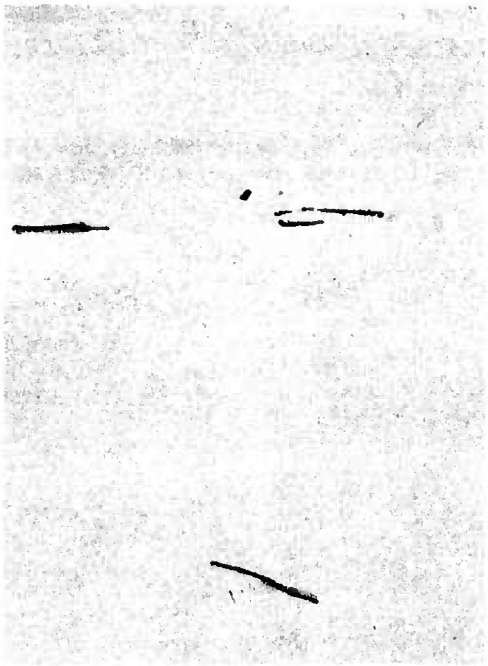

(a) POLISHED SPECIMEN, 1000X

(b) ETCHED SPECIMEN, 500X

MP-2024-35

FIGURE F-4 POLISHED AND ETCHED CROSS SECTION OF SHOCK LOADED XAR30 ARMOR STEEL SHOWING CRACKING AT INCLUSIONS

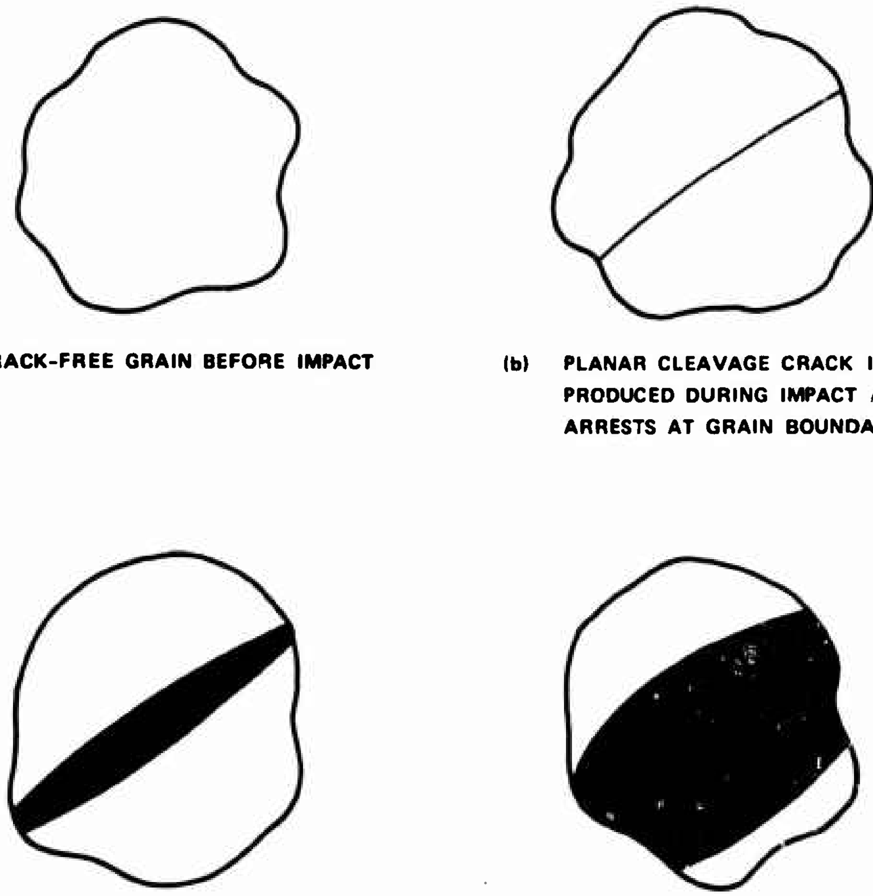

(a) CRACK-FREE GRAIN BEFORE IMPACT

(b) PLANAR CLEAVAGE CRACK IS PRODUCED DURING IMPACT AND ARRESTS AT GRAIN BOUNDARY

(c) ARRESTED CRACK BEGINS TO WIDEN AS THE MATERIAL AT THE CRACK TIP UNDERGOES INTENSE PLASTIC DEFORMATION

(d) WIDENING HAS OCCURRED TO SUCH AN EXTENT THAT THE ORIGINAL PLANAR FRACTURE APPEARS VOID-LIKE

MP-2024-36

FIGURE F-5 PROPOSED MECHANISM FOR VOID FORMATION IN ARMOR STEEL UNDER DYNAMIC LOADING

The suggested mechanism for void formation in armor steel is nucleation in the form of planar microcracks, arrest at grain boundaries, and displacement of crack faces. In coarse grained material such as Armco iron, the planar crack morphology is still apparent even after significant widening, as shown in Figure F-5. However, for steels in which the average grain diameter is about the same as the crack tip stretch the planar fractures of the original microcrack are lost and the microfracture appears void-like.

The dynamic fracture process in rolled armor steel is based on the proposed void formation mechanism and is thought to occur in the manner indicated in Figure F-3. Large numbers of inclusions fracture and/or voids nucleate on planes parallel to the rolling plane. These fractures become more equiaxed as they grow, and coalesce to form large planar fractures. Shear cracks form between parallel nonplanar macrocracks.

REFERENCES

1. M. L. Wilkins, "Calculation of Elastic-Plastic Flow," Methods in Computational Physics, ed. B. Alder, Academic Press, New York, 1964, p. 211.
2. T. W. Barbee, L. Seaman, and R. C. Crewdson, "Dynamic Fracture Criteria of Homogeneous Materials," Technical Report No. AFWL-TR-70-99, Air Force Weapons Laboratory, Kirtland Air Force Base, New Mexico, November 1970.
3. L. Seaman, T. W. Barbee, Jr., and D. R. Curran, "Dynamic Fracture Criteria of Homogeneous Materials," Technical Report No. AFWL-TR-71-156, Air Force Weapons Laboratory, Kirtland Air Force Base, New Mexico, December 1971.
4. D. A. Shockey, L. Seaman, and D. R. Curran, "Dynamic Fracture of Beryllium Under Plate Impact and Correlation with Electron Beam and Underground Test Results," Final Report No. AFWL-TR-73-12, Kirtland Air Force Base, New Mexico, January 1973.
5. D. R. Curran, D. A. Shockey, and L. Seaman, "Dynamic Fracture Criteria for a Polycarbonate," J. Appl. Phys., Vol. 44, No. 9, 1973, pp. 4025-4038.
6. D. A. Shockey, C. F. Petersen, D. R. Curran, J. T. Rosenberg, and L. Seaman, "Dynamic Tensile Failure in Rocks," Final Report, Contract H0220053, Bureau of Mines, Twin Cities, Minnesota, June 1973.
7. T. W. Barbee, Jr., L. Seaman, R. Crewdson, and D. Curran, "Dynamic Fracture Criteria for Ductile and Brittle Metals," J. of Matls., Vol. 7, No. 3, 1972, pp. 393-401.

8. D. A. Shockey, L. Seaman, D. R. Curran, P. S. DeCarli, M. Austin, and J. P. Wilhelm," "A Computational Model for Fragmentation of Armor Under Ballistic Impact," Final Report No. DAAD05-73-0025, Phase 1, U.S. Army Ballistic Research Laboratories, Aberdeen Proving Ground, December 1973.

9. M. M. Carroll and A. C. Holt, "Static and Dynamic Pore-Collapse Relations for Ductile Porous Materials," J. Appl. Phys., Vol. 43, No. 4, 1972, pp. 1626-1636.

10. J. K. MacKenzie, "The Elastic Constants of a Solid Containing Spherical Holes," Proc. of the Phys. Society, Sect. B, Vol. 63, 1950, p. 2.

11. I. N. Sneddon, and M. Lowengrub, "Crack Problems in the Classical Theory of Elasticity," John Wiley and Sons, Inc., New York, 1969.

12. S. N. Zhurkov, "Kinetic Concept of the Strength of Solids," Int. J. Fract. Mech., Vol. 1, No. 4, 1965, p. 311.

13. D. R. Curran, D. A. Shockey, J. P. Wilhelm, B. S. Holmes, and L. Seaman, "Shock Damage and Residual Mechanical Properties in Three-Dimensional Quartz Phenolic Composite Material," Final Report No. DNA-001-72-C-0201, Defense Nuclear Agency, Washington, D.C., December 1973 (SECRET).

14. C. F. Hickey, Jr., "Toughness Data for Monolithic High-Hardness Armor Steel," AMMRC PTR 72-3, Army Materials and Mechanics Research Center, Watertown, Massachusetts, July 1972.

15. D. A. Shockey, D. R. Curran, P. S. DeCarli, J. P. Wilhelm, and D. Petro, "Physical Changes Occurring in Armor Steel Under Hypervelocity Impact," Final Report No. DAAD05-73-0025, Phase II, U.S. Army Ballistic Research Laboratories, Aberdeen Proving Ground.

REFERENCES (Concluded)

16. D. J. Papetti, "Development of Improved Homogeneous Steel Armor," AMMRC SP 72-11, AMXMR-PL, Watertown, Massachusetts, July 1972 (Confidential).

17. C. E. Bieniosek, "Production of Homogeneous Armor Plates from Unidirectionally Solidified Steel Castings," U.S. Steel Corporation, report to AMMRC on Contract No. DAAAG46-71-C-0048, July 1972.

18. A. L. Stevens, L. Davison, and W. E. Warren, "Void Growth During Spall Fracture of Aluminum Monocrystals," Proceedings of Conference on Dynamic Crack Propagation, Lehigh University, Bethlehem, PA. (1972) to be published.

19. A. L. Stevens, L. Davison, and W. E. Warren, "Spall Fracture in Aluminum Monocrystals: Dislocation Dynamics Approach," J. Appl. Phys. 43, p. 4922 (1972).